



Hydrodynamics of open-channel confluences with low discharge ratio

José Martins Gouveia de Oliveira

Thesis to obtain the Master of Science Degree in

Civil Engineering

Supervisor: Prof. Doutor António Heleno Cardoso

Examination Committee

Chairperson: Prof. Dr. Rodrigo de Almada Cardoso Proença de Oliveira

Supervisor: Prof. Dr. António Heleno Cardoso

Member of the Committee: Dr. Elsa Cristina Tavares Lourenço Alves

May 2018

Declaração

Declaro que o presente documento é um trabalho original da minha autoria e que cumpre todos os requisitos do Código de Conduta e Boas Práticas da Universidade de Lisboa.

Abstract

Over the last century, river works were usually done with no regards for the impacts on the ecosystem, considerably impoverishing them. However, from the end of the last century, efforts were made to implement sustainable river rehabilitation. Good understanding of the river morphology and hydrodynamics is key for successful river rehabilitation projects. The present study was developed on this context, where a high angled confluence with high tributary sediment supply and low discharge and width ratios was studied.

The present experiments showed that some confluence features are different when these parameters are adopted. When confluences feature high tributary sediment supply, bed discordance occurs and a relatively large bank-attached bar is formed. On the other hand, in the presence of the combination of high tributary discharges and low tributary widths, the bed erosion is greatly enhanced at the scour zone, resulting in a greater scour hole. This combination also enhances the water jet flowing from the tributary channel, consequently enhancing the flow deflection, causing a great part of the width of the main channel flow direction being affected and deflected by the action of the tributary.

Using this knowledge, confluences which present similar control variables and parameters can be better interpreted, rendering possible rehabilitation and future interventions easier.

Resumo

Ao longo do último século, as obras fluviais foram feitas com pouco cuidado para com os impactos causados aos ecossistemas, o que os danificou consideravelmente. No entanto, desde o final do século, foram feitos alguns esforços de modo que a reabilitação fluvial fosse sustentável. Uma boa compreensão da morfologia e hidrodinâmica fluviais é a chave para projectos de reabilitação bem sucedidos. O presente estudo foi desenvolvido nesse contexto, tendo sido estudada uma confluência de elevado ângulo com alto caudal sólido afluente e baixos rácios de caudal e largura.

As presentes experiências mostraram que algumas características da confluência são diferentes quando estes parâmetros são adoptados. Quando uma confluência possui alto caudal sólido afluente, ocorre discordância entre leitos e forma-se uma grande barra de deposição no canal principal, imediatamente a jusante da confluência. Por outro lado, na presença da combinação entre altos caudais afluentes e baixas larguras do canal afluente, a erosão do leito é bastante potenciada na zona da cavidade de erosão, o que produz uma cavidade de erosão mais acentuada. Esta combinação potencia também o jacto de água que flui do canal afluente, o que acentua a deflexão do escoamento.

Utilizando o conhecimento adquirido, espera-se que se possa atingir uma melhor interpretação das confluências que apresentem variáveis de controlo semelhantes, facilitando futuros projectos de reabilitação nestas condições.

List of symbols and acronyms

B_m	Width of the main channel	[m]
B_t	Width of the tributary channel	[m]
B_r	Width ratio	[-]
Fr	Froude Number	[-]
P	Pressure force on a channel wall	[N m ⁻²]
Q_m	Flow discharge of the main channel upstream of the confluence	[m ³ s ⁻¹]
Q_t	Flow discharge of the tributary upstream of the confluence	[m ³ s ⁻¹]
Q_r	Flow discharge ratio	[-]
Q_d	Flow discharge downstream of the confluence	[m ³ s ⁻¹]
Q_{sm}	Solid discharge of the main channel upstream of the confluence	[kg h ⁻¹]
Q_{st}	Solid discharge of the tributary upstream of the confluence	[kg h ⁻¹]
Q_{rs}	Solid discharge ratio	[-]
U	Flow mean velocity	[m s ⁻¹]
Y	Flow depth	[m]
g	Gravitational acceleration	[m s ⁻²]
h_r	Adimensional relative height	[-]
t	Time	[s]
y	Local flow depth	[m]
y_d	Flow depth downstream	[m]
y_u	Flow depth upstream	[m]
α	Junction angle	[°]
ρ	Density	[kg ⁻¹ m ³]
ν	Kinematic viscosity	[m ³ s ⁻²]

Table of Contents

1	Introduction	1
2	State-of-the-art	3
2.1	General.....	3
2.2	Hydrodynamics of fixed bed open-channel confluences.....	4
2.3	Hydrodynamics and morphodynamics of mobile bed river confluences.....	10
2.4	Concluding remarks.....	14
3	Experimental set-ups and procedure	15
3.1	Experimental facility and equipment.....	15
3.1.1	Overall description of the facility.....	15
3.1.2	Bed topography and water surface level measurements.....	20
3.1.3	Flow velocity measurements.....	22
3.1.4	Water surface streamlines	25
3.2	Control variables and parameters	27
3.3	Experimental procedure.....	28
3.3.1	Achieving equilibrium bed morphology.....	28
3.3.2	Measuring flow velocities	31
3.3.3	Measuring the water surface streamlines.....	32
4	Experimental Results	35
4.1	Introduction.....	35
4.2	Morphology and water surface configuration.....	35
4.3	Hydrodynamics	38
5	Result discussion.....	53
5.1	Introduction.....	53
5.2	Morphology.....	53
5.3	Hydrodynamics	54
6	Conclusion.....	59
6.1	Conclusions	59
6.2	Limitations and Improvements	60
	References	63
	Appendices	67
	Appendix A – u/U isolines.....	67

Appendix B – v/U isolines	74
Appendix C – w/U isolines	81
Appendix D – vw pseudo-streamlines	88
Appendix E – u/U planviews	95
Appendix F – Flow surface streamlines planview	97
Appendix G – u/U planviews with bed topography overlay.....	98

*Aos meus pais que, apesar de tudo,
sempre acreditaram em mim.*

1 Introduction

River confluences are complex singularities of natural river systems, where two or more river channels join together to continue downstream as a single river. A few types of river confluences are usually identified, the most common of which consisting of a loose-bed main channel joined by a sediment laden tributary at a certain angle. Irrespective of the confluence type, the convergence of separated water and sediment flow bodies creates non-trivial three-dimensional (3-D) patterns, hard to understand and characterize due to the multitude of variables and variable combinations normally at stake.

Those complex 3-D patterns, including complex deposition and erosion mechanisms, induce a wide panoply of different *habitats*, thus contributing to the variety of river ecosystems. Also, by supplying water, sand and other sediments and food resources, tributary streams influence the habitat complexity and biodiversity of the main stream (Rice et al., 2008). As such, confluences are relevant generators of river heterogeneity, making their understanding an important subject. Furthermore, it is important to investigate the effects of river confluences on flow structures and patterns, in order to better design and manage hydraulic structures in river engineering. Despite the complexity, river confluences have received comparatively little research attention, probably due to the difficulty on their systematic replication in laboratorial environment. The natural consequence is that the existing knowledge on the topic is rather scarce.

To change this lack of knowledge, progress is required in two key areas. Firstly, the need for additional empirical data to evaluate the tributary effects on confluences, hence the use of an experimental approach for the present research. Secondly, the studies on confluences should be supported by intensive work that focuses on developing the understanding of each individual mechanism which takes part in confluence processes. Most studies demonstrate associations between these mechanisms and their effects on confluences. However, few attempts have been made to isolate the key processes and study them in detail.

This research work focused on analyzing the flow field within a laboratory confluence reach where the main channel dominated in terms of water discharge and the tributary was dominant regarding the sediment transport rate. The experimental results will enable the representations of the confluence flow fields. Only one experiment was carried out in view of

the complexity and the time required to perform it as well as of the large amount of data generated to be analyzed. Yet, it is expected that a greater understanding on the effect of the imposed conditions is achieved, thus contributing to a deeper and wider knowledge on the hydro-morphodynamics of river confluences.

The laboratory confluence was built in an experimental facility located at Instituto Superior Técnico of the University of Lisbon (IST-UL). The experiment was initially performed under movable bed conditions, with the objective of achieving the confluence equilibrium. After achieving the equilibrium, 3-D point flow velocities were measured by using one Vectrino probe with a pre-defined grid of points. Finally, the surface streamlines were obtained by processing the results of a large scale PIV technique.

This report is divided into six chapters and seven Appendices. After this introductory chapter, a state-of-the-art review is established, envisioning the grasp of concepts and contributions so far towards describing open-channel confluences and the associated hydro-morphodynamic processes. It covers differences between fixed and mobile bed channels as well as fixed-bed channels with and without tributary-mouth bed discordance. Afterwards, the experimental facility, the equipment and the experimental procedures are described in detail in chapter 3. The results of the measuring campaign, including mostly 3-D velocities, are presented and analyzed next (chapter 4), after which they are discussed and compared with previous studies (chapter 5). The main conclusions are finally summarized (chapter 6), along with the identification of limitations and possible future improvements. The Appendices contain representations of the experimental results.

2 State-of-the-art

2.1 General

According to Mosley (1976), two types of river channel confluences can be defined (Mosley, 1976): symmetric confluences, where both channels intersect with each other and form a Y-shaped plan pattern [see Figure 2.1 a)], and asymmetric confluences, where a tributary joins the main channel at a given confluence angle [Figure 2.1 b)], somewhat contributing to change the main channel shape downstream.



Figure 2.1 – a) Symmetric confluence of the Drava and Danube rivers. b) Asymmetric confluence of the Teesta and Rangit rivers (Source: Google).

Confluences are physically determined by many variables, the most important being the dominant water and sediment discharge rates, the geology of the surrounding valley, the size and size distribution of the loose bed material, the confluence angle and, depending on the flow regime, the bed slopes or the downstream flow depth. At a comparatively short time interval (decades), the composition of the valley and bed slopes can be assumed as invariant.

It should be noted here that the confluence angle is the angle defined by the axes of the converging channels, while the dominant water and sediment discharge rates can be considered through two different ratios: the water discharge ratio, $Q_r = Q_t/Q_m$ (where Q_m is the main channel dominant water discharge and Q_t is the equivalent discharge for the tributary, both upstream of the confluence); the sediment discharge ratio, $Q_{sr} = Q_{st}/Q_{sm}$, s standing for sediment while the other symbols keep their meaning.

After Taylor (1944) performed the first research work on the hydrodynamics of fixed bed confluences – mostly through the characterization of flow depths and average cross-section velocities –, contributing heavily to the knowledge on these complex singularities, the path was cleared for the studies that were developed on this subject until to the present.

In this context, it is indeed important to distinguish between two types of open-channel confluences: those with fixed bed and those with mobile or loose boundaries. These two types are characterized by different hydrodynamics but, above all, by the nature of the bed, since fixed bed channels are not prone to deformation through erosion and deposition, whereas mobile bed channels are. The latter are the focus of this study.

After this brief introduction on the general aspects of open-channel confluences, the literature review of the most important previous works is performed, including the differences between fixed and mobile bed cases.

2.2 Hydrodynamics of fixed bed open-channel confluences

In his pioneering work, Taylor (1944) considered a one-dimensional (1-D) approach and covered the junction angle of 45° of an asymmetrical confluence. By applying momentum and mass conservation equations, he calculated the ratio between upstream and downstream water depths. Webber and Greated (1966) followed the same research approach and studied the confluence angles of 30° , 60° and 90° .

Figure 2.2 represents a right-angled junction. In this figure, ρ is the water mass-density, whereas U and B correspond to average cross-sectional flow velocity and channel width, respectively. Subscripts 1, 2, and 3 refer to cross-sections EF, CI, and HG, respectively. Q_1 and Q_2 are fed upstream, while Q_3 is the downstream sum of Q_1 and Q_2 . U'_2 is the resultant average velocity of the deflected tributary flow entering the main channel, δ is the angle between the resultant velocity U' and the direction of the main channel axis and Π_u and Π_d are the stream-wise pressure forces on the walls CD and IA.

Both Taylor (1944) and Webber and Greated (1966) assumed the following simplifying hypotheses: i) the channels slopes are mild, the joining branches have the same cross-sectional area and the same bed level; ii) both upstream flows are subcritical; iii) both flows are uniform at cross-sections CI and EF and their depths are equal (Taylor, 1944); iv) boundary friction is negligible in the control volume (AICDEFGH); v) the flow depth in both cross-sections CI and DA is approximately the same, meaning that the mean velocity is also approximately the same.

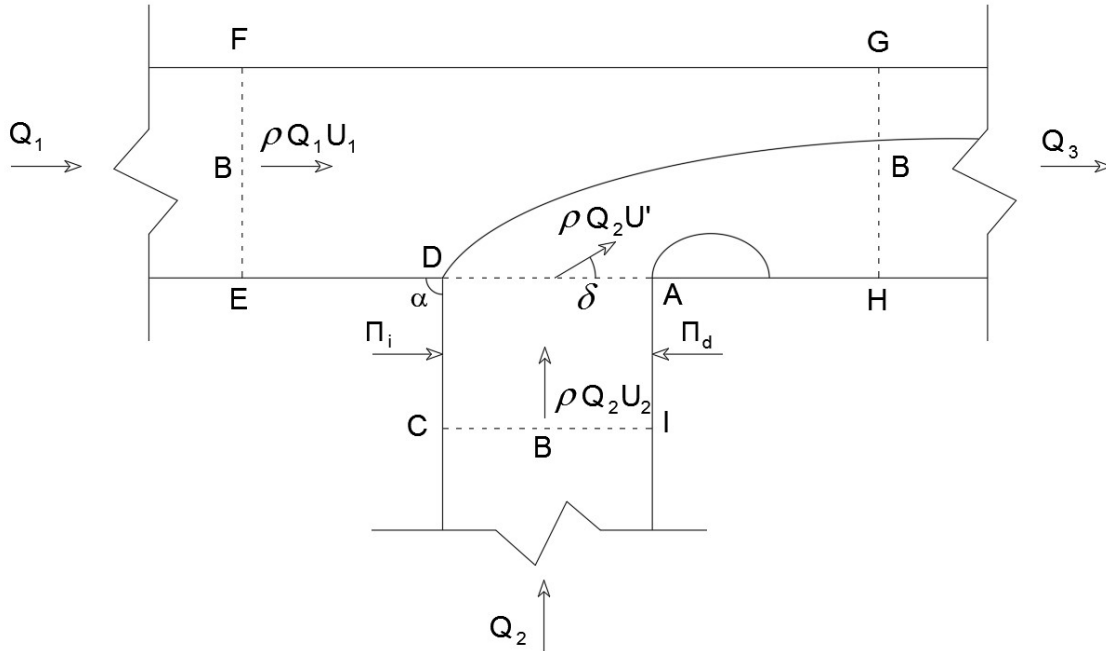


Figure 2.2 – Flow interaction and variables at right-angled open channel confluences with rectangular cross-section (Ramamurthy et al., 1988).

After Webber and Greated (1966), some authors (for instance Hager, 1989; Hsu et al., 1998; Shabayek et al., 2002) also proposed 1-D models to relate the water levels in the vicinity of the junctions, the observed head losses and the momentum transfer between channels for different junction angles, discharge ratios, channel widths, slopes and flow regimes. Through the usage of this one-dimensional model, Ramamurthy et al. (1988) studied the rise in upstream flow depth due to the effect of lateral inflow from the tributary channel. Using the relation between the flow depth at the junction and the discharge ratio, which is derived from the momentum principle, one can predict the rise in flow depth. However, this prediction can only be applied to a range of discharge ratios of $0,3 \leq Q_r = Q_2/Q_1 \leq 1,5$ (Ramamurthy et al., 1988).

Defining the upstream to downstream flow depth ratio as $h_r = h_u/h_d$, where u and d stand for upstream and downstream, respectively, and h is the flow depth, 1-D studies have shown that the increase in the junction angle, α , or in the downstream Froude number, Fr , induce the increase of h_r (Hsu et al., 1998). However, the strong three-dimensionality of the flow in open-channel confluences limits the usage of the one-dimensional approaches, thus impelling the use of empirical correction coefficients.

Later on, Best (1987) presented a somewhat sophisticated description of the flow dynamics at fixed bed open-channel confluences. According to Best (1987), “flow dynamics at confluences can be characterized by six major regions of flow stagnation, flow deflection, flow separation, maximum velocity, flow recovery and distinct shear layers”. These regions, illustrated on Figure 2.3, are mainly controlled by the junction angle and the water discharge ratio, Q_r , for a given width ratio, $B_r = B_t/B_m$.

The flow stagnation zone is caused by the clash of both streams near the upstream junction corner, which aggravates with the increase of the junction angle. At this zone, the flow velocities and shear stresses are reduced, reaching the limit of zero, and the water depth increases. Right after the stagnation zone comes the flow-deflection zone, where a shear layer is created between the convergent flows, generating powerful vertical vortices. On a mobile bed channel, these vortices highly influence bed scouring, since they are responsible for the increased bed shear stresses at this flow zone.

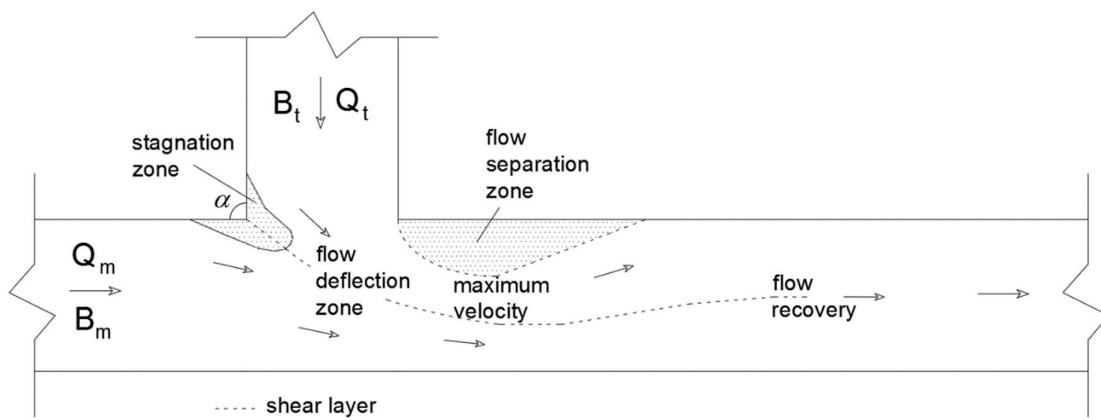


Figure 2.3 – Hydrodynamics at Open-Channel Confluences (Best, 1987).

Near the downstream junction corner, a zone of flow separation is formed. This happens because the tributary flow detaches from the main-channel wall due to the abrupt change in the boundary geometry. The dimensions of this zone increase as the junction angle and discharge ratio increase. Due to the low velocities at the separation zone and its recirculating nature, this zone is prone to sediment accumulation on a mobile bed situation, and thus a bar forms there, reducing the flow cross-section area.

The effectively reduced flow cross-section area alongside the separation zone induces the maximum velocity zone, as it delimits an area of the channel where the combined flows must pass. As such, the area between the separation zone and the opposed channel wall is

the maximum velocity zone of the confluence and it can be assumed that, on mobile bed channels, this zone is of great importance regarding bed erosion and sediment transport.

Strong velocity gradients originate shear layers. They are located between the separation zone and its surrounding flows, and at the “boundary” of flows coming from both channels. These shear layers are characterized by high turbulence intensity and shear stress, while having well-organized flow structures composed by distinct vortices that rotate around vertical axes (Rhoads and Sukhodolov, 2001; Sukhodolov and Rhoads, 2001). Confluence shear layers mostly occur when the distance between the water surface and the channel bed is small compared to the size of the vortical structures (Rhoads and Sukhodolov, 2004).

Downstream the separation zone, the flow recovers from the effects generated by the confluence dynamics. The channel will then return to a more symmetrical state, as both flows mix gradually and the turbulence declines.

Like Taylor (1944), most early models of junction hydrodynamics assume that the confluence bed level, including the approach reaches, is constant, which is a rare situation natural rivers, where the beds are discordant (Best and Roy, 1991) since the tributary tends to flow on a higher bed.

The impact of the bed discordance on the flow field was addressed by Biron et al. (1996) by comparing fixed bed confluences with and without bed discordance. Figure 2.4 reproduces and compares streamlines measured by Biron et al. (1996) for three different bed conditions of a confluence angled 30°, namely for: a) concordant bed; b) discordant bed with a vertical bed step at the tributary mouth; c) discordant bed for a sloppy incline of 45° penetrating the main channel.

Figure 2.4 a), referring to the concordant bed level, shows that the flow structure is essentially the same as described by Best (1987), despite the shorter and thinner separation zone with recirculation and a necessarily less marked maximum velocity zone. These differences are clearly due to the smaller confluence angle. However, some neat changes occur for the discordant bed cases, Figure 2.4 (b and c). The main channel flow deflection is almost absent for the vertical bed step and rather weak for the 45° bed step. In the latter case, separation seems to be induced by the avalanche face entering the main channel and forcing the flow to skirt the step. These bed features highly distort the shear layer created by the clash of both channel flows, enhancing rapid mixing of the flow preceding from the shallow tributary, while reducing the mixing of the deeper main channel flow (Best and Roy, 1991).

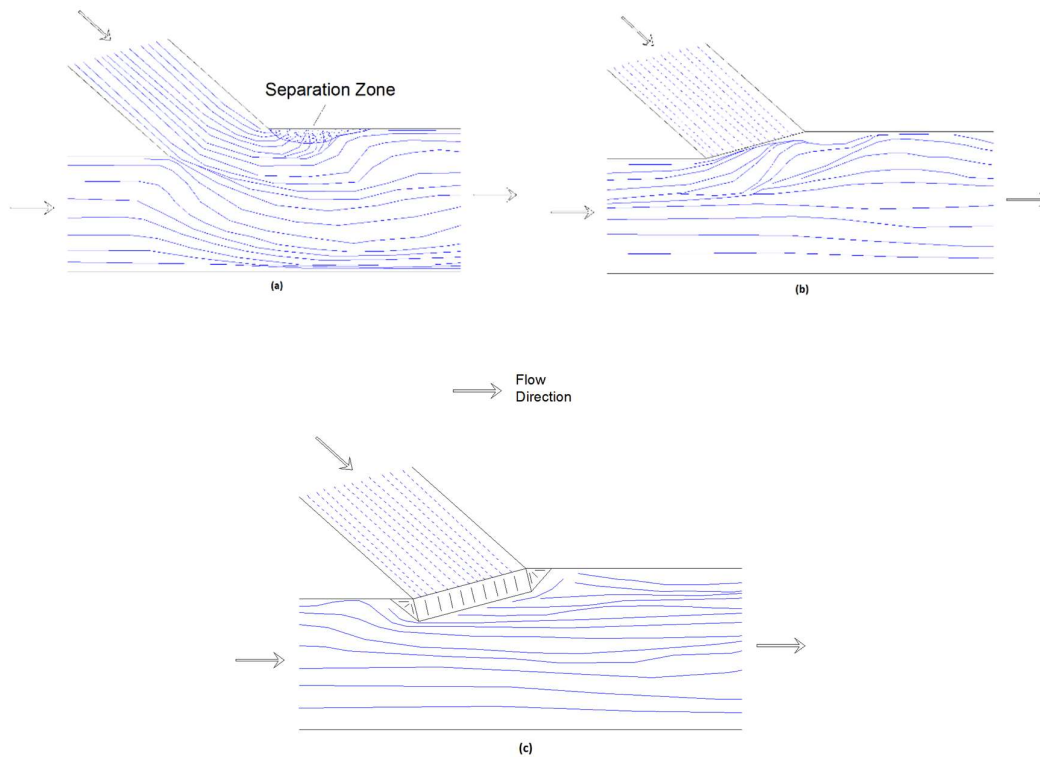


Figure 2.4 – Planview of bed streamlines in confluences with (a) concordant bed; (b) discordant bed with a 90° step; (c) discordant beds with a 45° step (Biron et al., 1996).

Figure 2.5 represents the downstream velocity components near the downstream junction corner zone, a) close to the bed, for a relative height $h^* = z/h_d = 0,06$ and b) near the water surface, for a relative height of $h^* = 0,81$. Herein, the relative height h^* is defined as z/h_d , where z is a given height above the bed.

It can be observed that there is a relevant velocity decrease where the separation zone is located for the concordant bed, for both the bed and surface of the channel, *i.e.*, for $h^* = 0,06$ and $h^* = 0,81$, respectively. No relevant reduction is seen, however, near the bed for both discordant confluences (b and c). On the contrary, near the water surface, there is a neat reduction of the flow velocity including flow recirculation, revealing a drastic vertical change of velocities in the same plan location. This indicates that, for discordant beds, even though the separation zone is destroyed near the bed, it does exist near the water surface.

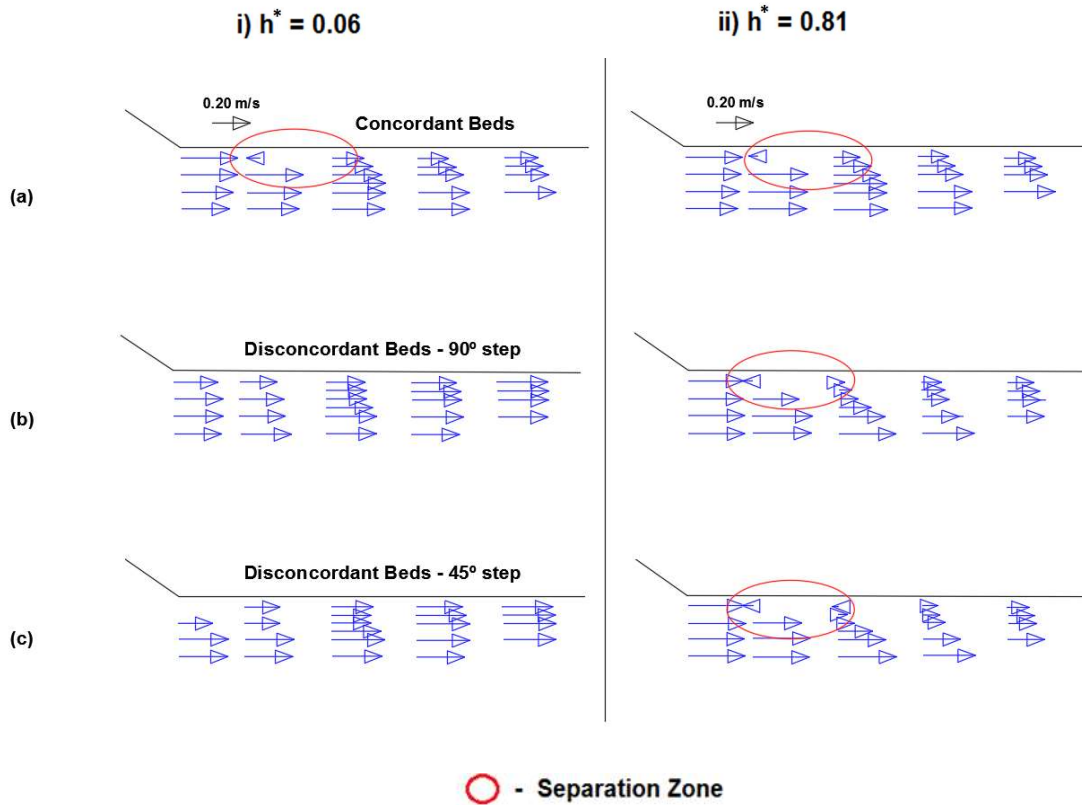


Figure 2.5 – Velocity vectors near downstream junction in confluences with (a) concordant beds; (b) discordant beds with 90° step; (c) discordant beds with 45° step (Biron et al., 1996).

For discordant beds, a very strong vertical motion is formed right after the step, near the downstream junction corner [Figure 2.6 b) and c)], which differs highly from the concordant bed, where the vectors are basically horizontal [Figure 2.6 a)]. This vertical motion is the cause of the destruction of the separation zone near the bed for discordant confluences. Still, the separation zone exists near the water surface, where this vertical motion is much less significant, corroborating the observations made on Figure 2.5.

Since it is now understood that the separation zone is destroyed near the bed for discordant confluences, it is safe to assume that no relevant flow acceleration zone will be present near the downstream junction corner for this situation. However, a small acceleration zone still remains near the water surface, resulting on higher velocities [Figure 2.5 (ii)]. Additionally, the mixing layer, which is created when the flows meet and grows in width downstream (Best and Roy, 1991), is distorted towards the shallower tributary. This causes an upwelling at the downstream junction corner, caused by the turbulence generated near the step (Biron et al., 1996).

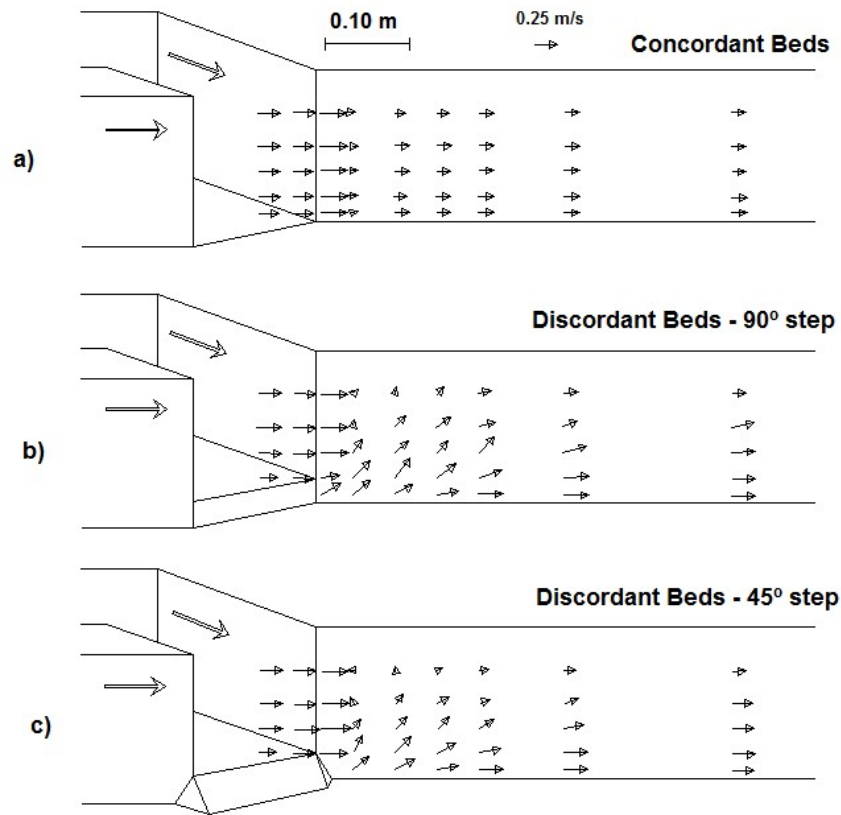


Figure 2.6 – Plot of uv vectors along the longitudinal section near the tributary sidewall for (a) concordant beds; (b) discordant beds with 90° step; (c) discordant beds with 45° step (Biron et al., 1996).

The influence of bed discordance on the deflection of flow, its mixing layer and separation zone indicates that the discordance must be taken into account when dealing with river confluences, since it alters its hydrodynamics and, consequently, its morphodynamics.

2.3 Hydrodynamics and morphodynamics of mobile bed river confluences

Mosley (1976) was the author who first studied mobile bed river confluences, namely of the symmetric type (Y shaped). Later on, Best and Reid (1984), Best (1987, 1988) and Bristow et al. (1993) have proposed comprehensive morphodynamic models of asymmetric river confluences.

According to Best (1988) and Bristow et al. (1993), the typical bed morphology of asymmetrical river confluences includes a scour hole, two river-mouth bars and a bank attached bar (Figure 2.7):

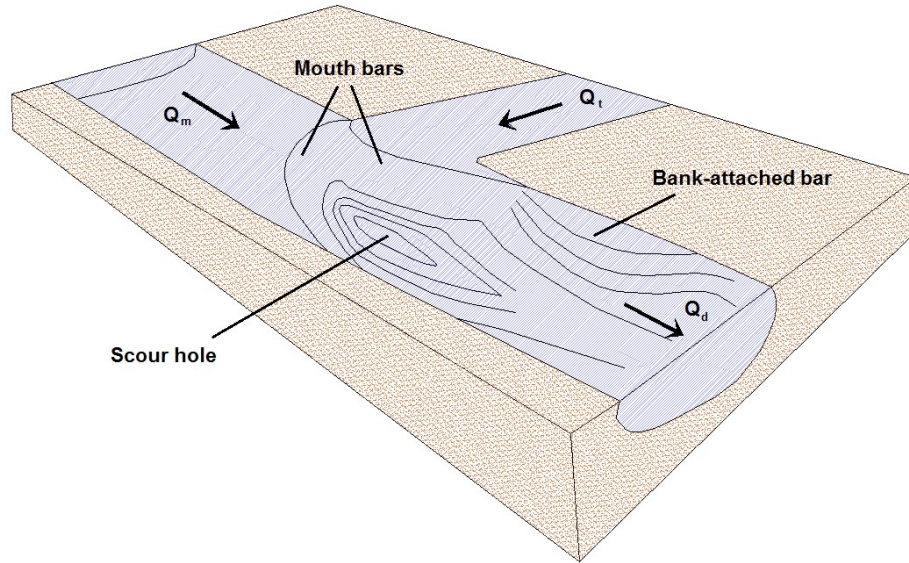


Figure 2.7 – Morphology of Open-Channel Confluences (Bristow et al., 1993).

River-mouth bars are a sort of avalanches formed at the downstream end of both tributary and main channels, typically right upstream of the confluence. Their slope and height increase with the confluence angle and the discharge ratio, due to the increasing influence of the tributary channel. Those avalanches connect the bed of the joining channels to the scour hole, above which the higher flow shear stresses and turbulence intensities are observed. The scour hole is in turn delimited by the avalanche faces as well as by the bank-attached bar; it can be assumed to start at the upstream junction corner and extend downstream by approximately bisecting the junction angle. The decrease of the discharge ratio leads to a scour hole oriented closer to the downstream junction corner. The scour hole is practically inexistent for very low discharge ratios and junction angles under 15° (Best, 1988). The bank-attached bar, associated with the flow deceleration, is usually formed downstream of the scour hole. The shape of this bar also depends on the junction angle and discharge ratio. Best (1988) proposed a model for sediment transportation which illustrates the influence of the discharge ratio on confluences according to Figure 2.8.

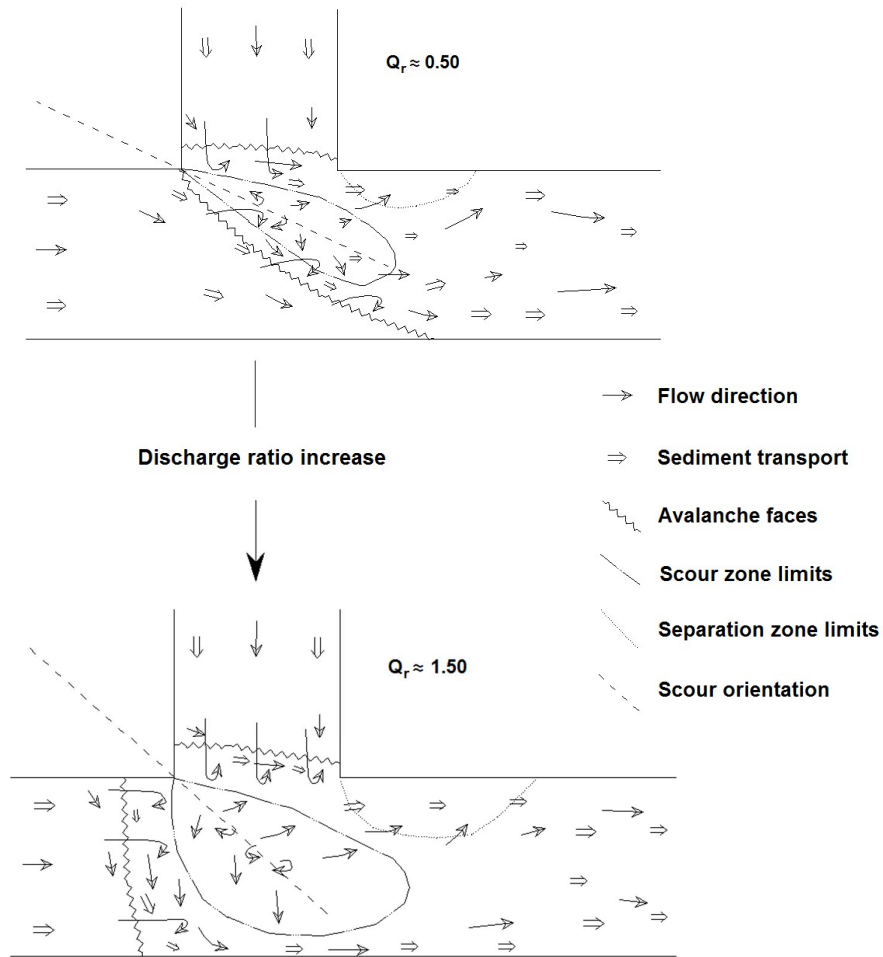


Figure 2.8 – Sediment Transport on Open-Channel Confluences (Best, 1988).

Figure 2.8 shows that an increase in the discharge ratio increases the width and length of the bank-attached bar. The main channel avalanche face recedes, resulting in a wider and deeper scour hole, which is then oriented more towards the outer bank of the main channel, showing the increasing effect of the penetration of the tributary flow and deflection of the main channel flow. An increase in the junction angle also produces the aforementioned changes on the morphology. The sediment grains mostly move along the borders of the scour hole, joining further downstream.

Apart from the junction angle and the water discharge ratio, other variables significantly influence the erosion and deposition processes in the confluence. According to Best and Rhoads, 2008, these include the plan form, the channels widths upstream, the ratio of momentum of the converging flows and the sediment discharge ratio. The same applies to the hydrodynamics.

For symmetrical confluences, Mosley (1976) observed the generation of two helical cells on top of the scour hole. These cells are generated by the converging flows and are separated by a shear layer (Figure 2.9). Flow from both channels plunges into the scour hole, resurfacing along its walls. The water surface is super-elevated over the hole because of the overlapping of flows and the consequently generated vertical vortices. These helical flows explain the steep external walls of the scour hole, while permitting these walls to maintain angles higher than the angle of repose of the material and preventing sediment movement into the center.

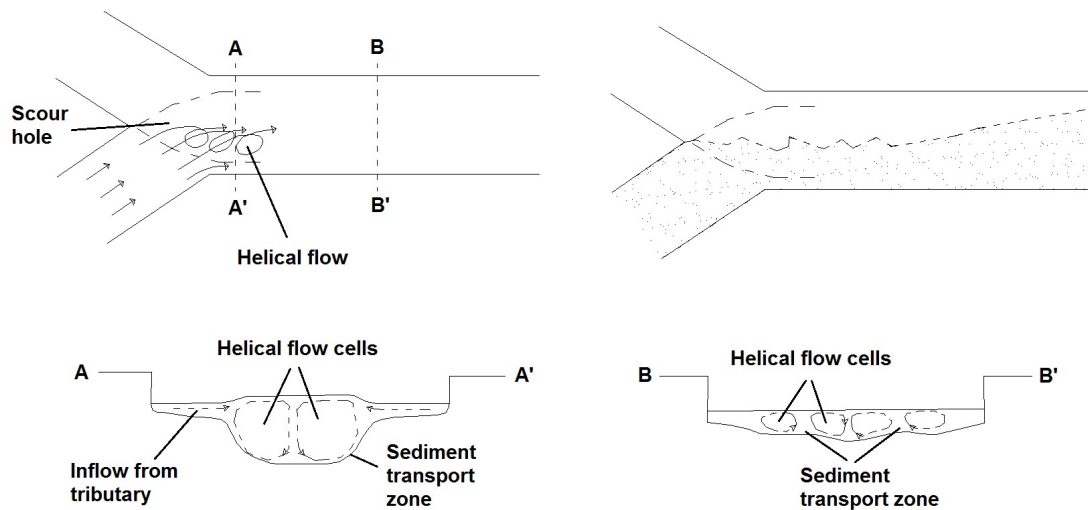


Figure 2.9 – Flow patterns in a model confluence (Mosley, 1976).

The streams from both channels remain mostly separated through the scour hole, mixing gradually downstream. This separation occurs due to vertical vortices on the shear layer. Complete mixing often does not occur for tens or even hundreds of channel widths downstream of large river confluences but local conditions such as irregular bed topography can lead to rapid mixing. The existence of helical cells was confirmed, both in the laboratory and in the field, by Fujita and Komura (1989) and Rhoads and Kenworthy (1998), respectively.

The hydrodynamics of asymmetrical mobile bed confluences is deeply influenced by the bed discordance created by the tributary mouth bar. Leite Ribeiro (2011) concluded that the most important features of the hydrodynamic model suggested by Best (1987) for fixed concordant bed confluences also occur at mobile bed asymmetrical confluences. These include the flow stagnation zone, the flow deflection zone, the flow acceleration zone, the shear layers and the recovery zone. On the contrary, the separation zone that occurs on fixed bed channels is normally replaced by a low velocity zone, located on top of the bank-attached bar. A two-layer flow structure is observed near the tributary mouth. This two-layer flow

structure, consequence of the bed discordance, is composed by an upper layer and a lower layer. The upper layer consists of flow from the tributary channel, which enters the main channel with an angle that is smaller than the junction angle, obstructing the flow coming from the main channel. The lower layer flow consists of obstructed flow from the main channel, which flows under the upper layer flow (Biron et al., 1993). This lower layer collides with the bank-attached bar and leads to an upwelling zone near the downstream confluence junction corner. This near-bed flow prevents the formation of a zone of flow recirculation.

2.4 Concluding remarks

After reviewing the existing literature on open-channel confluences, some conclusions were drawn, including the variables which control the hydraulic and sedimentary processes, such as the confluence junction angle, the water and solid discharges, the channel widths and the planform of the confluence.

Hydraulic and sedimentary processes present on confluences are extremely complex. However, both hydrodynamics and morphodynamics have features that are fairly well described. The confluence hydrodynamics can be divided into six major regions: flow stagnation, flow deflection, maximum velocity, flow recovery, shear layers and flow separation. The last region is replaced by a low velocity zone on top of a bank-attached bar. On the other hand, the morphology can be divided into three main regions: scour zone, bank-attached bar and main/tributary channel mouth bars. The mouth bars are related to the bed discordance and this discordance affects greatly the separation zone, resulting in the previously mentioned low velocity zone.

Despite the well described features, few field studies were made regarding natural river confluences, which exposes the lack *in situ* knowledge on this subject. Also, most studies regarding open-channel confluences relied on fixed bed channels. As such, the present study might bring light to some questions that are inherent to the subject, mainly the hydrodynamic processes of mobile bed flumes.

3 Experimental set-ups and procedure

3.1 Experimental facility and equipment

3.1.1 Overall description of the facility

The experimental facility used in the study was composed by a main and a tributary channel. A schema can be seen on Figure 3.1.

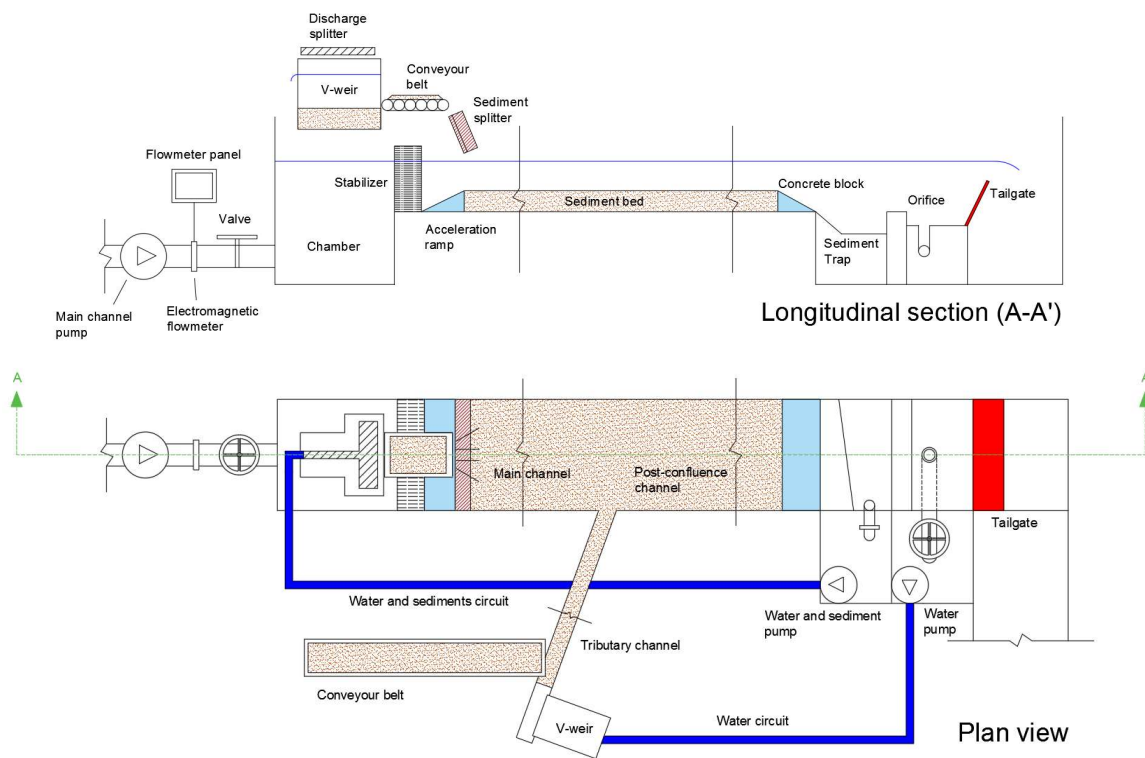


Figure 3.1 – Experimental facilities.

The main channel was a 12,0 m long and 1,0 m wide concrete rectangular flume with a glass wall reach. Since the width was constant along its full length, the main channel upstream width was equal to the post-confluence channel width ($B_d = B_m$). Starting upstream, a large underground reservoir was connected to the main channel by a pipe. This pipe circuit included a pump and conveyed the design discharge, which was measured by an electromagnetic flowmeter, with an accuracy of $\sim 0,1$ l/s (Figure 3.2).

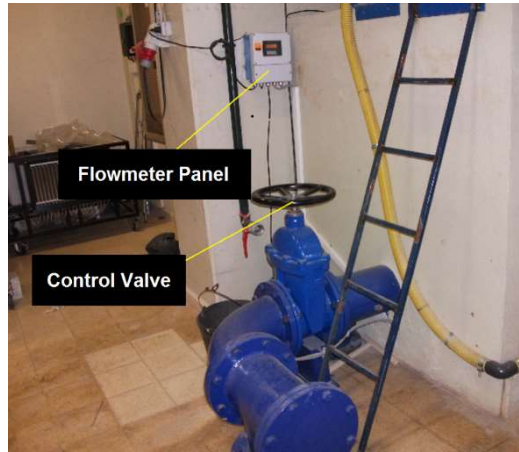


Figure 3.2 – Main channel electromagnetic flowmeter.

The discharge could be adjusted by a valve that was located between the pump and the main channel, as also seen on Figure 3.2. The discharge was poured into a chamber that was followed by a flow stabilizer, which reduces flow instability. After the flow was stabilized, it was accelerated by a bed ramp, followed by the sand bed. This sand bed was confined by the concrete bed, by the ramp upstream and a concrete bed sill downstream, used to define the origin of the Z axis of the referential. The geometry and referential schematic of the experimental facility can be observed on Figure 3.3. Both channels had their own referential, which each robotic car used to make measurements. These cars and their referential will be explained in more detail on the next subchapter.

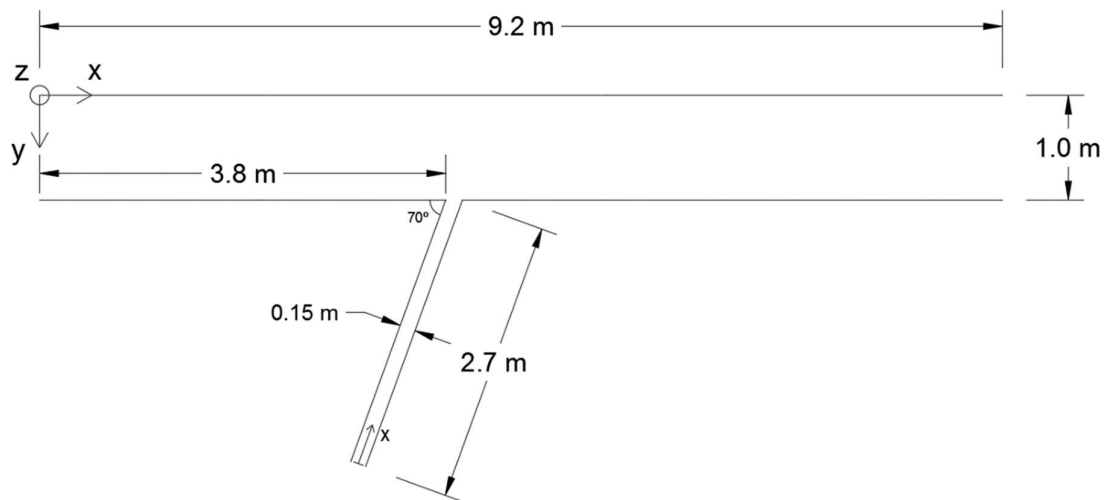


Figure 3.3 – Geometry and referential of the channel.

Downstream of the concrete bed sill a sediment trap was located, followed by an orifice and an adjustable tailgate [Figure 3.4 a)]. The downstream water depth was imposed via tailgate adjustment, by using a limnimeter installed next to it. The sediment trap configuration leaned towards the right bank of the main channel where a pipe, which was controlled by a valve, conducted the mix of water and sediments into a tank. The orifice was connected to a pipe, also controlled by a valve, which led water into another tank that was connected to the previous tank through a spillway. These tanks were also connected through another spillway to the channel downstream of the tailgate, which leads to the underground reservoir Figure 3.4 b).

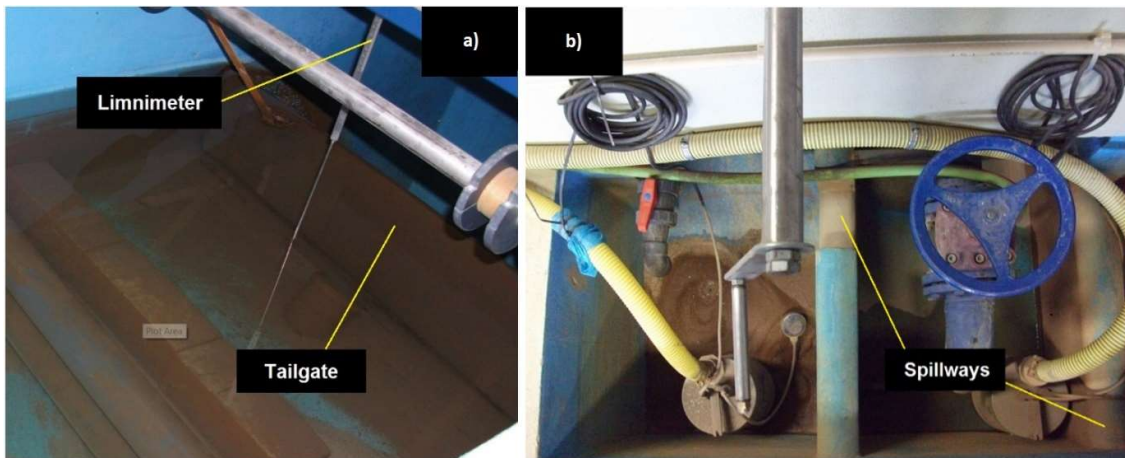


Figure 3.4 – a) Adjustable tailgate alongside the limnimeter. b) Tanks connected by spillway.

The tributary channel was a 4,5 m long and 0,15 m wide PVC rectangular channel that joined the main channel with a 70-degree angle (see Figure 3.3).

As mentioned before, water was pumped from a large underground reservoir into the initial chamber, flowing downstream through the stabilizer, into the main channel (see Figure 3.5). The sediments were initially deposited on conveyor belts, both on main [Figure 3.6 a)] and tributary channels [Figure 3.6 b)]. At the main channel, there was a sediment splitter, which evened the sediments along the full width of the channel. At the tributary channel a splitter was not necessary, since its width was relatively small. The sediments fell into both channels and flowed downstream, in the direction of the confluence.

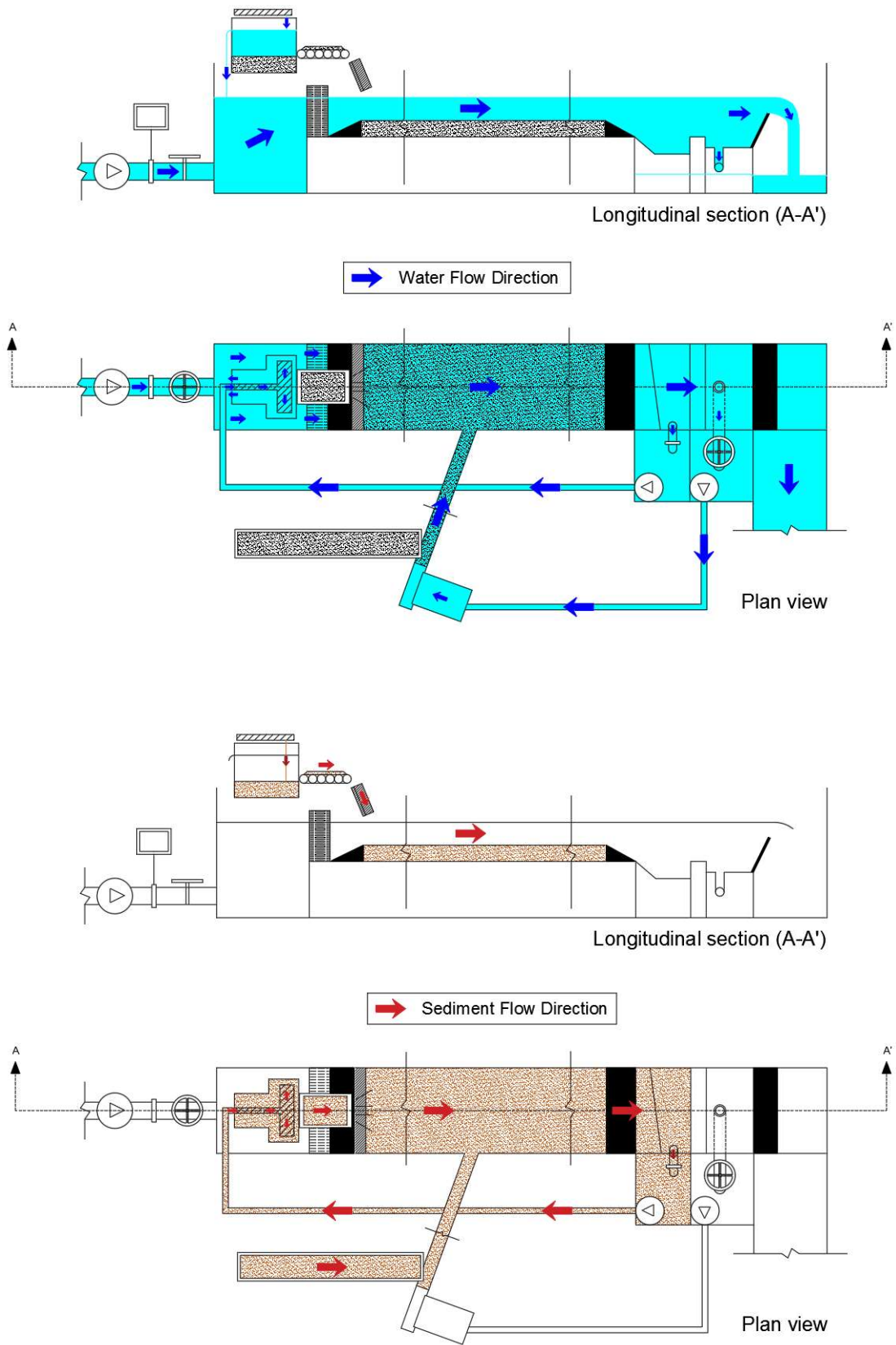


Figure 3.5 – Water and sediment circuits.



Figure 3.6 – a) Main channel conveyor belt and sediment splitter. b) Tributary channel conveyor belt.

The mixture of water and sediments moved along the channel and reached the sediment trap downstream. After the sediments were captured, they fell into the tank which contained a pump that sent both sediments and water through a pipe, into a V-weir sediment recovery tank, placed on top of the main-channel upstream cross-section [Figure 3.7 a)]. This tank was the final container for the sediments, which required a low turbulence. If high turbulence existed, the sediments would flow back into the channel. To minimize this undesired effect, the flow passed through a discharge splitter located above the tank [Figure 3.7 a)]. The sediments were trapped and the water flowed back to the main channel. After 1,5 hours passed, the sediments were extracted from the tank and weighted on a digital dynamometer, with a $\sim 0,5$ kg accuracy [Figure 3.7 b)].



Figure 3.7 – a) Sediment recovery tank with V-weir at the main inlet. b) Digital dynamometer.

In the main channel, the water, now cleared of sediments, reached the tailgate. Right before the tailgate, part of the water flow was drained down through a pipe, controlled by a valve, which was connected to the tank that possessed the water-only pump. This water was pumped into the V-weir that feeds the tributary channel, flowing downstream into a new cycle.

The flow that was not caught into the pipe passed above the tailgate and plunged into a channel that leads to the underground reservoir.

3.1.2 Bed topography and water surface level measurements

Two robotic cars moved on rails on both main [Figure 3.8 a)] and tributary [Figure 3.9 b)] channels. The main channel robotic car had a metallic graduated adapter, which allowed the installation of measuring probes, as shown on Figure 3.8 b). This adapter was connected to a robotic arm that could move three dimensionally.

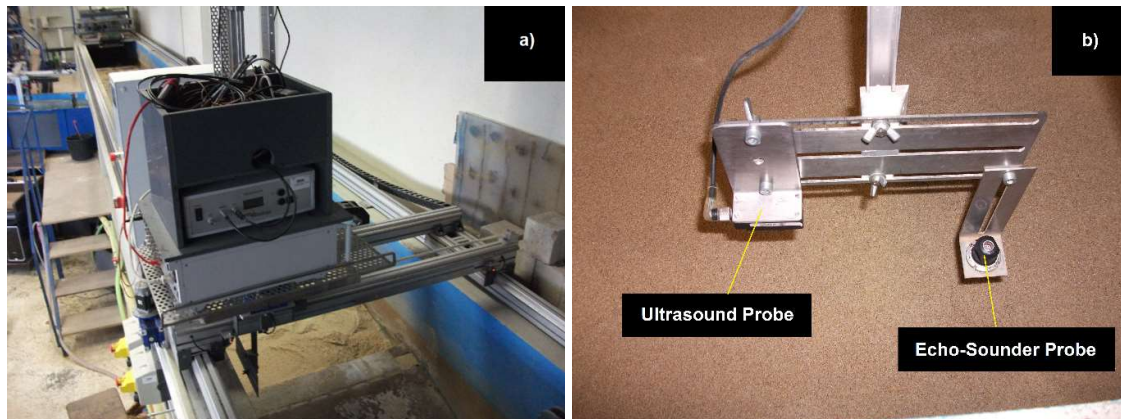


Figure 3.8 – a) Main channel robotic car. b) Main channel probes (ultrasound on the left, echo-sounder on the right).

On the tributary channel, the probes were installed on a metallic adapter [Figure 3.9 a)], which was connected to the robotic car.

Relatively to the referential presented on Figure 3.3, both main and tributary car rails were aligned with each channel X axis. The measurements from the tributary referential were later transformed to fit the main channel referential. The referential used on the tributary channel is two-dimensional, since only one profile was measured along the X axis. One profile is enough to fully describe the tributary, due to its relatively small width. The Z and Y

coordinates were established by positioning the adapter along the tributary channel axis, before the measurements were made.

It is important to refer that all the measurements performed with the robotic cars were controlled by the Conflume software, which was developed by IST for this particular installation.



Figure 3.9 – a) Tributary channel probe support (echo-sounder installed, ultrasound on standby). b) Tributary channel robotic car.

Topography and water level were measured using Echo-Sounder and Ultrasound probes, respectively, with ~ 1 mm accuracy. Both robotic cars had a probe of each type attached.

The Echo-sounder probe must be slightly submerged when measuring, so it is able to measure the topography. This probe has a membrane that vibrates at a given frequency, sending sound pulses underwater. Once the sound pulses reach the sand bottom, they are reflected back to the probe and the time interval between emission and return of the pulse is measured. The distance between the probe and the target can now be calculated, since both travel time and pulse propagation velocity are known. For the main channel, the zero for the Z axis for the echo-sounder probe was found using the top of the downstream concrete block, right upstream of the sediment trap, as reference. For the tributary channel, it was made using the PVC bottom as reference.

Like the Echo-sounder probe, the Ultrasound probe has a membrane that vibrates at a given frequency, sending sound pulses in the direction of the water surface. Once the sound pulses reach the water surface, they are reflected back to the probe and the time interval between emission and return of the pulse is measured. The distance between the probe and

the target can now be calculated, since both travel time and pulse propagation velocity are known.

Since the main channel probes are not located at the exact same X position [Figure 3.8 b)], there are some differences between topography and water level profiles. This can be solved by simply adapting the final X value for each measurement according to the probe position relatively to the referential used.

The values obtained through the measurements do not correspond to the real value. As seen in Figure 3.10, the measured values correspond to dm_{top} and dm_{wl} (topography and water level, respectively), which do not coincide with the adopted referential origin. As such, calculating dr is imperative in order to have the correct values for both topography and water levels. Since the total distance between the probes and the origin of the referential is known, dt_{top} and dt_{wl} , the real values can be approximately calculated by the following equation:

$$dr = dt - dm$$

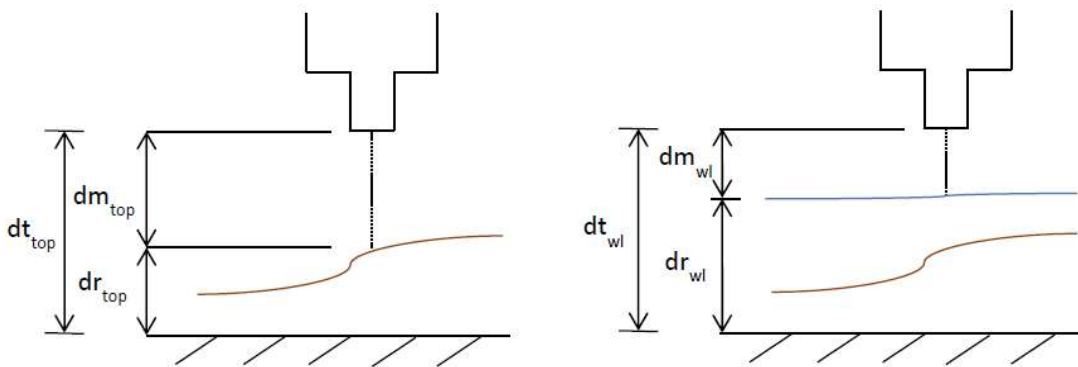


Figure 3.10 – Relative distances for the probes.

3.1.3 Flow velocity measurements

The velocities were measured using a Vectrino probe, which was attached to the main channel robot. The Vectrino (Figure 3.11) is a velocimeter that can measure the 3D flow velocity over a given vertical range, with a resolution of 1 mm, at rates up to 100 Hz. The basic measurement technology is coherent Doppler processing, which is characterized by accurate data at high rates with no appreciable zero offset.

Besides the velocities, the output data generated by the Vectrino probe is divided into amplitude, SNR and correlation. The amplitude measures the strength of the signal. The SNR, or Signal-to-Noise Ratio, expresses amplitude relative to the probe noise level in dB. The higher the SNR is the better the measurements are. Finally, the correlation is a measure of the signal quality in percent, which means that higher correlations are synonym of better results. Mixing these performance indicators is the key factor on deciding if measurements are eligible for post-treatment or not.

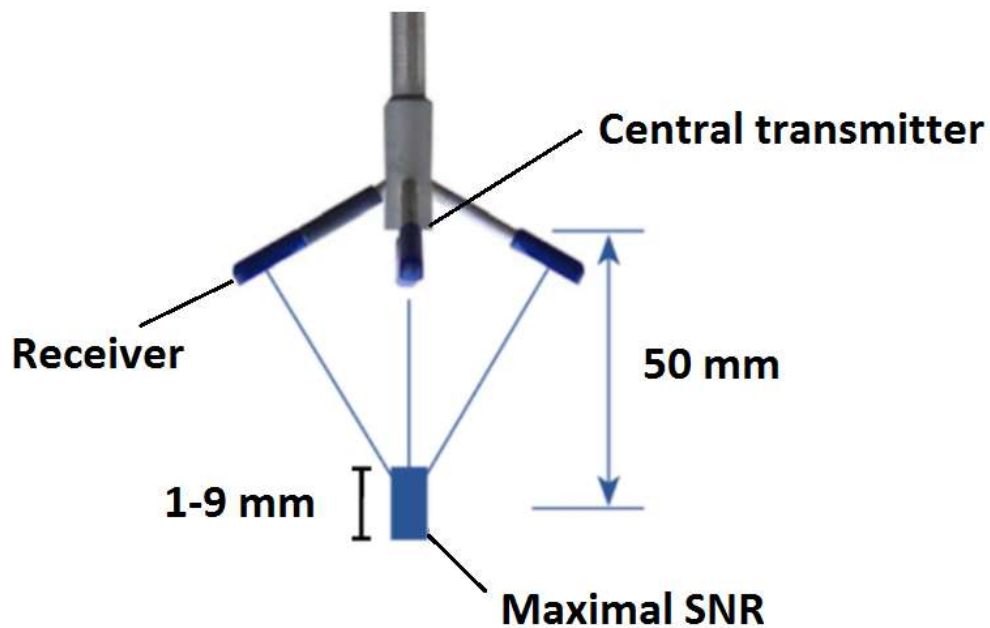


Figure 3.11 – Vectrino transmitter and receivers.

Particles scattered in the water reflect acoustic pulses. The movement of these particles relative to the transmitter results in a Doppler shift, which is the change in frequency or wavelength of a wave (or other periodic event) for an observer moving relative to its source, which Vectrino uses to estimate velocities using the Doppler relationship. The Doppler shift is estimated from a change in phase between two signals.

The sample volume of a single point can be simply considered like a “cylinder”, as represented in Figure 3.11, which is a result of the intersecting beam patterns.

It should be also noted that the measurements were done with a sidelooking Vectrino probe (see Figure 3.12). The design of the probes results in different noise levels for the different components. For the sidelooking probe there is usually more noise in the vertical component, while for the downlooking probe there is usually a higher noise level in the horizontal components.



Figure 3.12 – Sidelooking Vectrino probe.

A grid was defined prior to the measurements (Figure 3.13), which the Vectrino probe uses as a reference for the points measured. This grid was characterized by varying intervals on the X axis, which depend on the importance of the area of measurement. Naturally, it was denser at the confluence area, since this is where the three-dimensional processes are more complex, requiring more extensive data. On the Z axis, the grid was characterized by intervals of 0,5 cm, starting 3 cm below the water surface and ending 2 cm above the bed.

The limits of the grid, which neither extend from the surface of the water to the bed nor from the left to the right bank, are related to the physical limits of the Vectrino sidelooking probe. Starting with the vertical limits, as explained, the data obtained by the probe is affected by the Signal-to-Noise Ratio, which is very low near the surface of the water, since the uppermost receivers of the probe get intermittently out of the surface. On the other hand, the probe cannot get to the lowest point near the bed, since its lower receivers are located on a lower position relatively to the measuring “cylinder”.

For the width limits, since the probe can only “look” to one side, the left bank was neglected, while the right bank was close to full coverage.

As most of the measuring procedure was automated by the usage of this grid on the software Conflume, the attention could be focused on SNR and correlation values which, if low, could have a negative effect on the results.

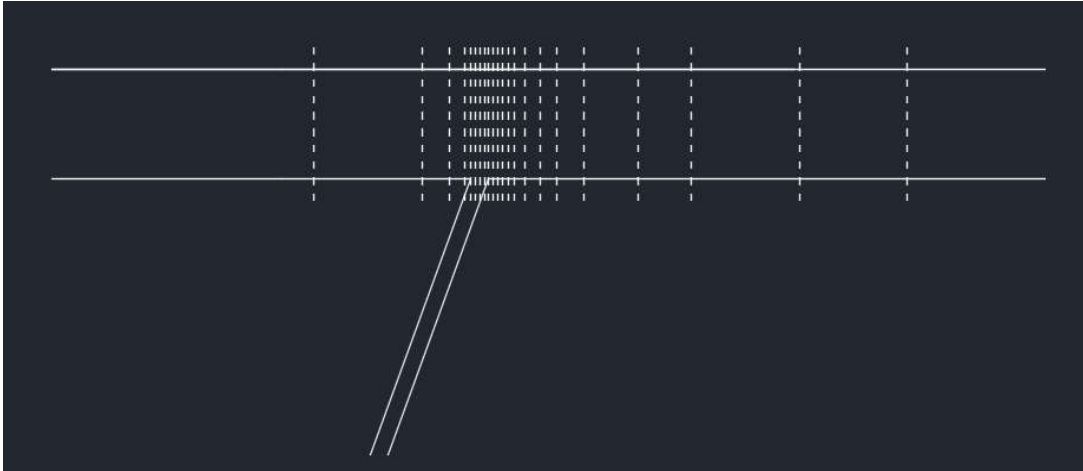


Figure 3.13 – Sections measured by Vectrino.

Before the measurements could be started, however, a calibration of the cars had to be done. The Vectrino probe needed to be installed at $z = 0$ m, relatively to the Conflume software referential, which was translated into $z = 0,1$ m according to the used referential. This was caused by a discrepancy between the experimental and the Conflume referential. The used referential X and Y axis are shown on Figure 3.3. The $z = 0$ m of this referential corresponds to the top of the downstream concrete bed sill on the main channel.

Another relevant consideration revolves around the fact that there is a gap between the point measured and the Vectrino position. This is illustrated on Figure 3.11 and the solution is to simply add this difference to the final results, on the Y position (since the probe used is sidelooking).

3.1.4 Water surface streamlines

The water surface streamlines were obtained by processing the images captured by a high-resolution camera, installed on the ceiling above the confluence area. The camera position could be adjusted horizontally along a rail, allowing the recording of several sub-surface areas of the water surface. The objective was to take several images of floating styrofoam balls, which flowed downstream, and then draw the resulting streamlines from the obtained frames. The styrofoam balls were poured into the channel using a distributor that was manually operated [Figure 3.14 a)]. A net [Figure 3.14 b)] was installed downstream of the main channel to collect the styrofoam, so that it could be removed from the water circuit and be reused on later runs, after drying out.



Figure 3.14 – a) Styrofoam distributor installed upstream of the main channel. b) Downstream net after collecting styrofoam.

A metallic square grid, with 1 m x 1 m dimensions, was used as referential for the recording of the streamlines [Figure 3.15 a)]. This grid had horizontal and vertical threads spaced by 0,1 m, dividing it in a 10 x 10 grid, composed by smaller 0,1 m x 0,1 m squares. Since the camera could not capture the full grid, the recording was divided into four sections. A spotlight was used to enhance the images taken by the camera and was installed on a metallic adapter that could be placed perpendicularly to the main channel [Figure 3.15 b)].



Figure 3.15 – a) Square metallic grid installed on the main channel. b) Spotlight and its metallic adapter.

The area considered for characterizing the streamlines was greater than the grid dimension. To enable full coverage of this area, the recording was divided into several runs. Each run corresponded to the recording of a given section and the schematic can be observed on Figure 3.16. I, II and III correspond to the three positions where the grid was installed, each composed by four sections. At position III, only two sections are present since the sections

further downstream were out of reach for the camera rails. Note that this figure is merely representative, having the main objective of depicting the recording sections without regard of dimensions or proportions of both channels geometry.

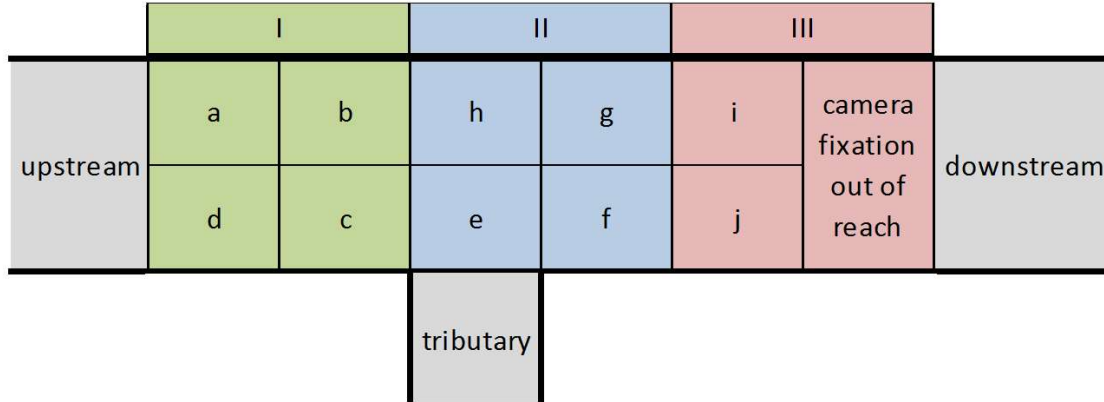


Figure 3.16 – Streamline recording sections.

3.2 Control variables and parameters

From the description of the experimental facility, it can be concluded that the widths of the tributary and main channels were $B_t = 0,15$ m and $B_m = 1,00$ m, respectively, meaning the value of the width ratio adopted in this study was $B_r = 0,15/1,00 = 0,15$.

The junction angle of natural confluences is approximately $2\pi/5 = 72^\circ$, according to Devauchelle et al. (2012). In this experiment's case, the adopted junction angle was $\alpha = 70^\circ$, very close to the central value observed in rivers.

The main channel discharge was $Q_m = 43,0$ l/s and the tributary discharge was $Q_t = 7,0$ l/s and, consequently, the discharge ratio was $Q_r = 7,0/43,0 = 0,16$. However, the unit discharge ratio was much higher: $Q_m/B_m = 43,0/1,0 = 43,0$ and $Q_t/B_t = 7,0/0,15 = 46,7$, resulting in a unit ratio of $Q_r/B = 46,7/43,0 = 1,09$. The solid discharge was $Q_{sm} = 12,0$ kg/h for the main channel and $Q_{st} = 30,0$ kg/h for the tributary channel, resulting in a solid discharge ratio of $Q_{rs} = 30,0/12,0 = 2,5$. The unit solid discharge ratio was much higher: $Q_{sm}/B_m = 12,0/1,0 = 12$ and $Q_{st}/B_t = 30,0/0,15 = 200,0$, resulting in a unit ratio of $Q_{rs}/B = 200,0/12,0 = 16,7$.

The adopted downstream water depth, y_d , right upstream of the sediment trap, was $y_d = 0,10$ m, which was calculated using the Manning-Strickler equation:

$$Q = KA \frac{2}{3} S^{\frac{1}{2}} \quad (1)$$

where Q is the discharge (m^3/s), K is the roughness coefficient ($m^{1/3}/s$), which is given by the formula

$$K = \frac{26}{\frac{1}{d_{90}^6}} \quad (2)$$

A is the cross sectional area (m^2), R_s is the hydraulic radius (m), $R_s = A/P$, S is the channel slope and d_{90} is the sand characteristic diameter.

3.3 Experimental procedure

3.3.1 Achieving equilibrium bed morphology

Before the experiment, the initial flatbed was prepared using a well-graded sand, characterized by $D_{50} = 0,86$ mm and $\sigma = 1,36$. The particle-size distribution can be observed on Figure 3.17. To speed up the bed topography evolution process, initial bed slopes of 0,2% and 1% were imposed to the main and tributary channels, respectively, and a slight discordance between both channels was added. This initial state was possible to control with the help of the ultrasound probe. The initial bed morphology does not affect the equilibrium bed morphology since the initial slopes and discordance are lower than on equilibrium (Leite Ribeiro, 2012).

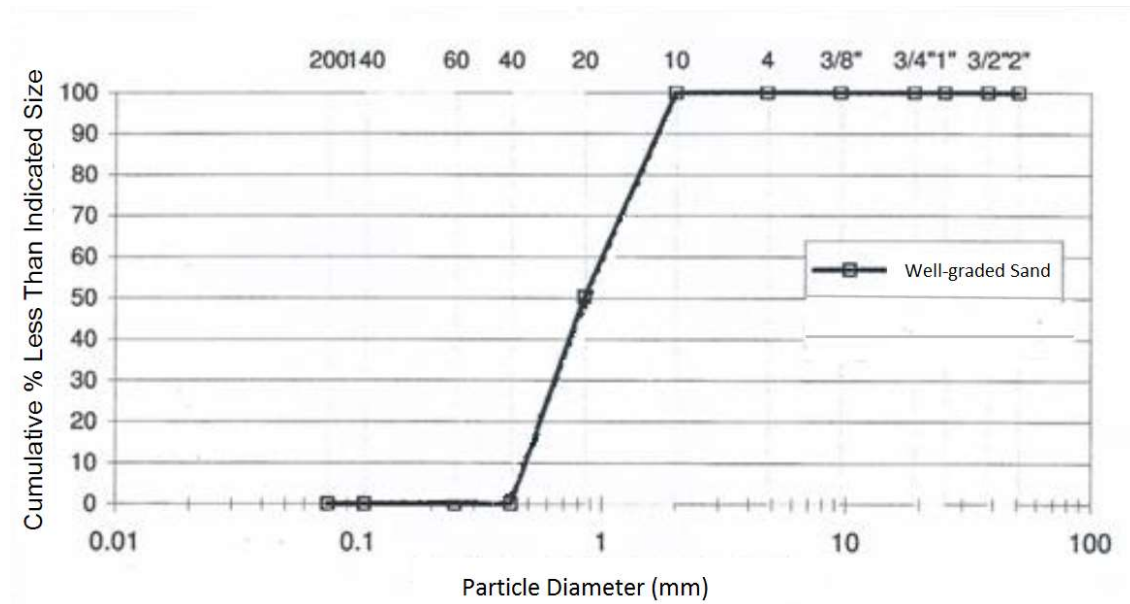


Figure 3.17 – Particle-size distribution for the sand used on the experiments.

After the bed was prepared, the tailgate was completely closed and the flume was slowly filled with water. The initial topography was then measured using the Echo-sounder probes. Both sand conveyors were prepared for the upcoming run, filling the main channel one with 18 kg and the tributary one with 45 kg.

The flow discharges were then adjusted to the previously mentioned values, while the tailgate was slowly opened to achieve the desired flow depth. These two steps had to be done carefully, as too much instabilities could damage the bed. After the desired conditions were established, the sand conveyors and the pumps were turned on and the first run began ($t = 0$ h).

Each run had the duration of 1,5 h and was performed under movable bed conditions, while continuously feeding sediment supplies to both channels. After each run, the tailgate was slowly raised and the pump discharges were greatly reduced, raising the water level and lowering the flow velocity, stopping the sand discharge and providing a stable environment for the use of the echo-sounder probe. This was mandatory since the probe needs to slightly penetrate the water surface. This stable environment was accomplished by lowering the main channel discharge to 10 l/s and turning off the pump that fed water to the tributary channel through its V-weir, as well as the pump that fed water mixed with sediments to the main channel V-weir. On these conditions, the topography was measured and the next run began.

To start a new run, both channel discharges were adjusted to the defined experimental values, the tailgate was slowly lowered to achieve the desired flow depth and the sand conveyors were turned on. After the downstream pumps were submerged, they were turned on and the new run began.

Since the Ultrasound probes do not have to be submerged, the water level measurements were done without the need of stopping the run. The water level measurements were done after the time elapsed for each run was half an hour.

On the main channel, the bed topography and water level measurements consisted of longitudinal profiles spaced by 0,01 m along the X axis. This ultimately led to the measurement of 87 profiles. On the tributary only one longitudinal profile was recorded.

This procedure was done until the equilibrium was met, meaning solid output being equal to the input. To assess the equilibrium, the sediment transport rate was evaluated by weighting the amount of sediments collected by the sediment recovery system between runs. After shutting down the downstream pump that fed the main channel V-weir tank, a valve on the bottom of the tank was opened, draining its water and the sediments were extracted. The

time to reach equilibrium was 22,5 h and an illustrative graphic of this iterative process is shown on Figure 3.18.

The red line shows the target sand weight for the equilibrium (63 kg per 1,5h, or 42 kg/h), while the dashed lines represent the acceptable 5% error band. Take note that each point on the graph occurs with an interval of 1,5 h, which is the duration of each run.

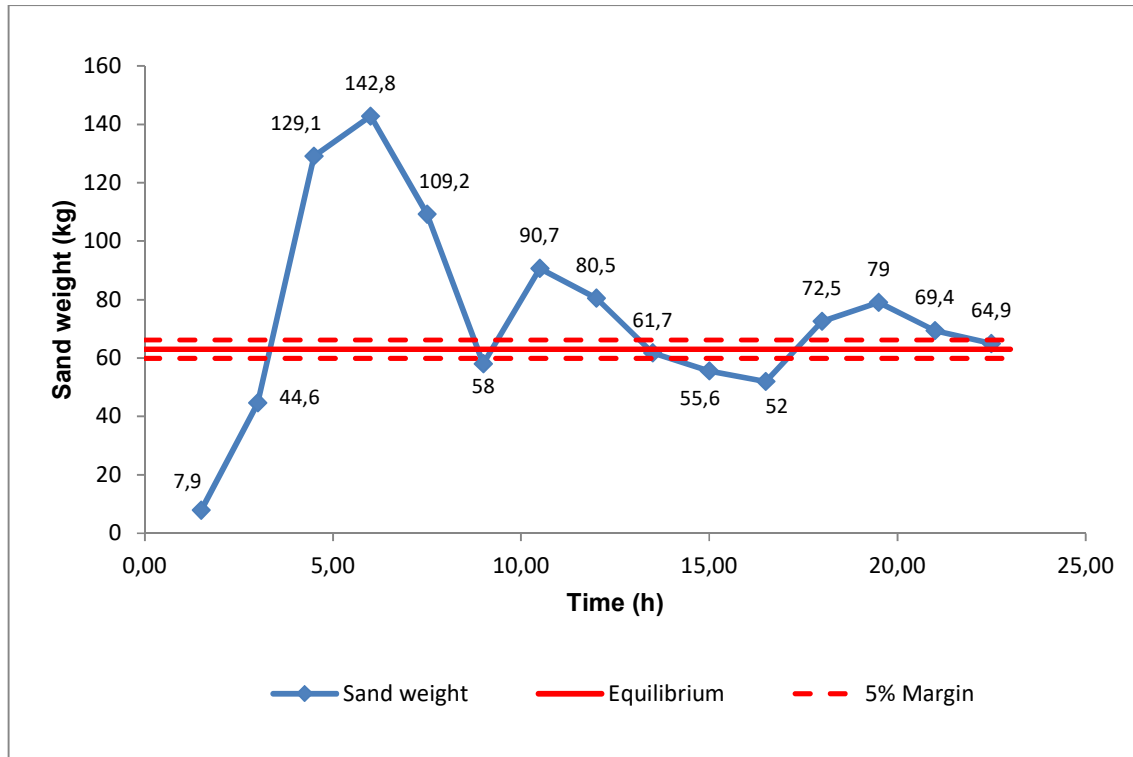


Figure 3.18 – Graph portraying the equilibrium determination.

Having achieved equilibrium state, the water was drained through a drain located at the bottom of the channel, which was controlled by a valve. Since there was a relatively high discordance between channels, as the water was drained a high velocity downstream flow was created on the tributary channel, which could greatly erode the confluence area. To prevent this occurrence, the valve was closed almost completely, right before the flow started gaining velocity.

After the water was drained, the bed was covered by a layer of cement [Figure 3.19 a)]. A layer of varnish was later added, providing a much more stable and resistant bed [Figure 3.19 b)]. The outcome of this procedure was a “frozen” bed morphology corresponding to the equilibrium stage of the movable bed confluence reach. On these conditions (final conditions),

a final run was made and both water level and topography were measured, using the respective probes, to account for minor changes on the flow and bed conditions. The final run had no solid discharge, since the equilibrium was already met.



Figure 3.19 – a) Aspect of the flume after cement cover. b) Applying the varnish on the flume.

3.3.2 Measuring flow velocities

After the final conditions for the bed were achieved, the preparations for the second phase began. The Echo-sounder and the Ultrasound probes were removed from the main channel adapter and the Vectrino probe was installed (Figure 3.20).

Since the grid (Figure 3.13) had a very high number of points and each point took two minutes to measure, which meant several days, completing this phase on a single run would not be wise. Many variables could render the run useless, such as the laboratory power source shutting down, a blue screen occurring on the computer used or very low SNR values occurring on particular areas of the channel. With this in mind, the grid was divided into six parts, which were used on separate runs.

The channels had to, once again, be filled with water, so a small discharge was fed to the main channel, the tailgate was completely lifted and the flume was slowly filled with water. Since the bed was covered by a layer of cement and varnish, the raise of the water level caused the compression of the air contained in the sand against the impermeable layer, which could damage and alter the bed morphology. To mitigate this phenomenon, orifices were done on the impermeable layer using a small stake, allowing the passage of the air trapped beneath it.



Figure 3.20 – Installed Vectrino probe.

The flow discharges were then adjusted to the experimental values, while the tailgate was slowly lowered to achieve the desired flow depth. The first grid part was loaded into Conflume, the car was positioned at the first point of the grid and the run started. After each run ended, another grid part was loaded into Conflume and another run started. This procedure was done until all grid parts were completed, generating a very large data set, ready to be treated and exploited.

3.3.3 Measuring the water surface streamlines

The third and final phase preparations began by installing the styrofoam distributor on the main channel, upstream of the confluence, and filling it with styrofoam balls. The styrofoam trapping net was then placed downstream of the main channel. A high definition camera was installed on a rail located on the ceiling, above the confluence area, and the grid was positioned on the first section, according to the recording plan (Figure 3.16).

The camera lens was pointed towards the first section and then focused using floating styrofoam balls as reference. Note that the water surface was used as a focusing reference instead of the grid, since the objective was to have frames with particles that were as clear as possible. The spotlight was installed and pointed towards the first section. Some details had to be considered when installing the spotlight: firstly, the laboratory lights were turned off, minimizing external light reflections to the camera; secondly, the spotlight itself could also produce light reflection, which had to be minimized with careful positioning.

Before each run, a single frame was taken with the grid in position. This served as referential for each section, providing a metric for the processed trajectories. The grid was then removed, clearing the section for the upcoming run.

After the preparations were completed, the first run began. The styrofoam was released into the stream using the distributor and the camera started recording. The distributor had a separator which allowed the release of styrofoam into the desired section of the channel. This would later be a problem, leading to inaccurate streamlines, which will be discussed at the experimental results chapter. For sections E, F and J (Figure 3.16), the styrofoam was also released on the tributary channel. The recording was done by taking 100 frames per second, for 20 seconds, resulting in a total of 2000 frames per run. Once the run was over, the frames were saved into the hard drive and a new run was prepared. This procedure was repeated until all sections were covered, while periodically emptying the downstream net as needed.

Since this was the final phase of the experiment, after all runs were over, the temporary installed equipment was removed and stored and the water was drained from the channel.

Finally, having all sections recorded, the frames were processed using Matlab. Basically, the raw images were pre-processed with a contrast function, which also converted the peaks into coordinates on a matrix. Using proximity between particles found on each consecutive frame and multiple mechanisms for error reduction, e.g. eliminating a particle if it disappeared during a given number of frames, the trajectories were then calculated and saved on individual matrixes for each section. The 10 resulting matrixes were then joined and a final streamline planview was obtained.

4 Experimental Results

4.1 Introduction

In this chapter, the flow hydrodynamics will be analyzed, establishing a relationship between the brief introduction presented on the state of the art and the current experimental study. Although the morphology is not the focus of this study, a short analysis of the features that are present on the flume bed will be made at the start of this chapter.

Due to the high quantity of processed figures, most of them will be presented as appendices, although some extracts will be done to better illustrate the observations being made throughout the result discussion.

As a remark, all the figures were obtained with the usage of Matlab and went through a heavy process of data treatment and processing. This data treatment was extensive and could only be properly explained by guiding the reader through each batch of code used for each process.

Generally speaking, most of the data was processed by using contours with the data matrixes obtained from the measurements. The topography and water level measurements were simple to treat, since the data is much more intuitive and is a simple file containing the x , y and z values for each run. On the other hand, the velocity outputs were much more complex and had to be simplified by averaging the various measurements for each point.

4.2 Morphology and water surface configuration

Before the measurements on the velocities were made, the topography was measured at intervals of $t = 1,5$ h. Using Matlab, it was possible to draw both $2D$ and $3D$ views of the flume's bed topography. Only the last topographic measurement instant will be shown, $t = 22,5$ h, which corresponds to the equilibrium state of the flume. All morphological features of confluences, identified by Best (1988), were present on the flume (Figure 4.1).

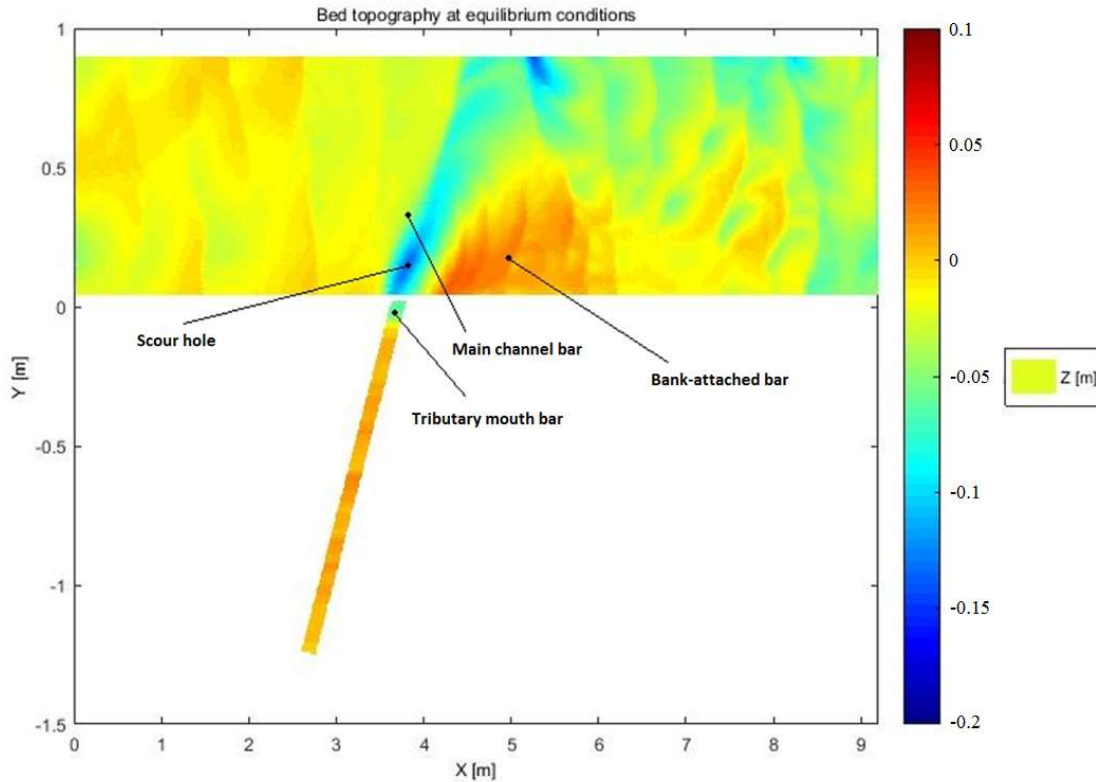


Figure 4.1 – Bed topography on 2D view.

The bars formed at the end of both tributary and main channels appeared right upstream of the confluence. The scour hole was very pronounced, with a height difference between the deeper zone and the average upstream height of $0,175\text{ m}$. Ripples were formed along the main channel. These bed configurations were perpendicular to the channel walls upstream of the confluence, but were distorted downstream, approximately perpendicular to the bank-attached bar. There was another scour hole along the left bank, due to the forced confinement of the flow in there.

It is clear that a bed discordance between channels was present, although not very pronounced. This discordance was $\sim 0,05\text{ m}$ high.

The 2D view of the water level can be observed at Figure 4.2. The water level dropped 8% between the upstream ($x = 0\text{ m}$) and downstream limits ($x = 9,20\text{ m}$). The water level dropped mostly at around $x = 5\text{ m}$, downstream of the confluence.

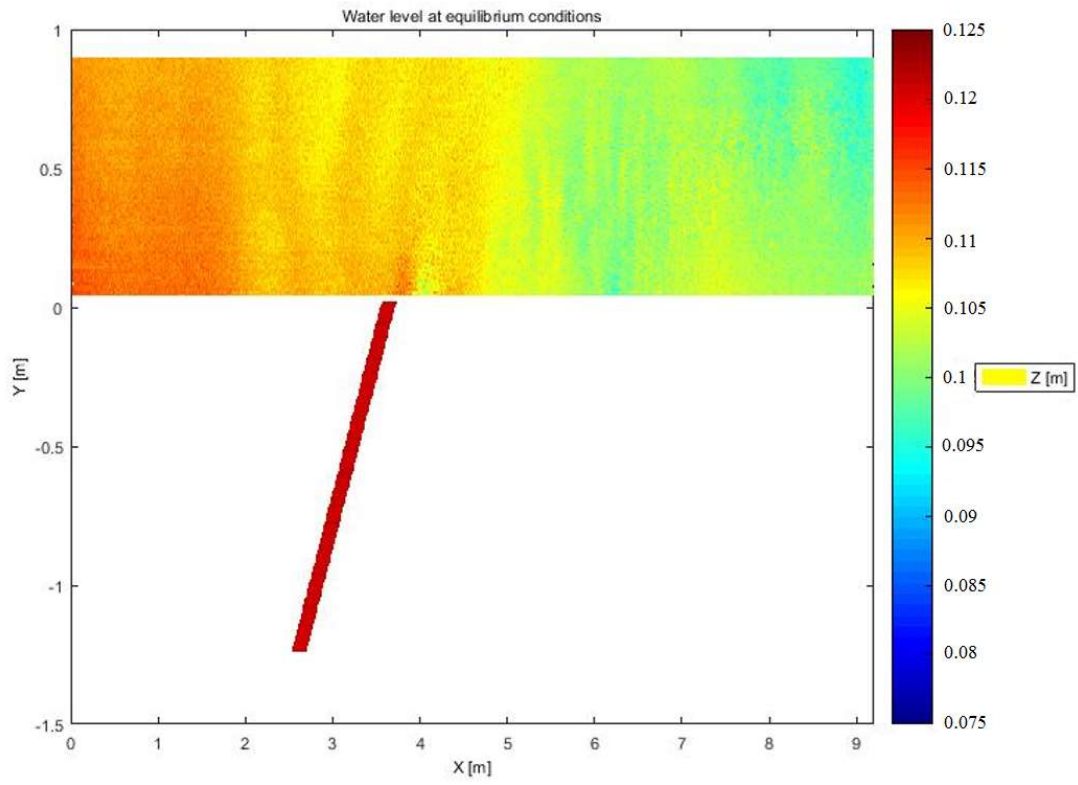


Figure 4.2 – Water level on 2D view.

4.3 Hydrodynamics

The figures referent to the hydrodynamics are presented in the Appendices with greater resolution, and cover the relevant velocity profiles and streamlines regarding the flume. The measurements were only done after the flume reached the equilibrium, which corresponds to the topography presented on Figure 4.1. As stated before, all figures were obtained with Matlab after treating the data retrieved from Conflume, which receives data from the Vectrino probe. The sections correspond to those represented on Figure 3.13.

The figures represent, firstly, each section, regarding u/U , v/U , w/U isolines and vw cross-sectional flow directions, considered as pseudo-streamlines. Secondly, the 2D planview of the flume is represented for two heights, $Z = 0,09\text{ m}$ and $Z = 0,05\text{ m}$. These planviews are important to consider on the present study, since they allow that a connection between cross sections and a complete overview of the flow is made. Lastly, the surface streamlines are presented, wrapping up all the experimental data.

Starting upstream, the flow seems relatively undisturbed by the confluence further downstream (Figure 4.3). The bed is approximately flat and the flow is approximately symmetrical, meaning the flow velocities are approximately evenly distributed throughout the channel width, which is shown through the values of u/U . The values of v/U , w/U and vw are roughly zero, indicating low flow instability and reinforcing the observation of symmetrical flow. Since the flow appears symmetrical until the disturbance of the confluence affects it, other sections ($x = 2,38\text{ m}$ and $x = 3,63\text{ m}$) that also depict upstream symmetrical flow can be consulted in the Appendices.

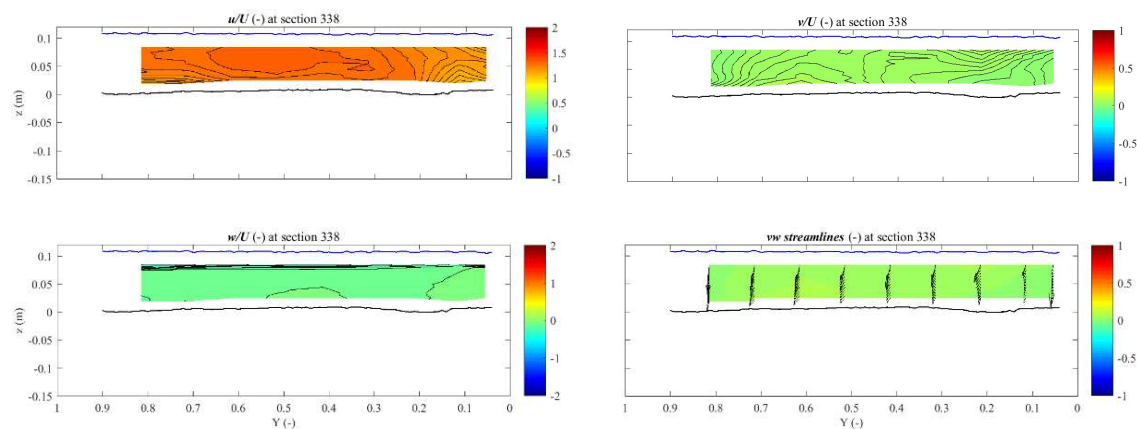


Figure 4.3 – u/U , v/U , w/U and vw “streamlines” at section $x = 3,38\text{ m}$.

These conclusions can also be drawn by observing the u/U planviews (Figure 4.4 and Figure 4.5). In both Figure 4.6 a) and b), which are excerpts of Figure 4.4 and Figure 4.5, respectively, it is observable that the channel flow is approximately symmetrical upstream of the confluence.

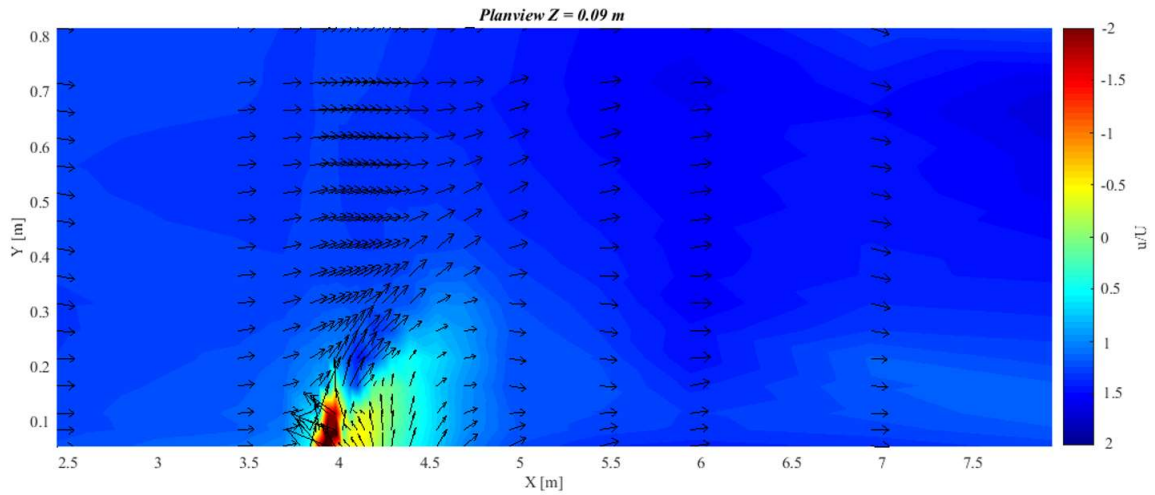


Figure 4.4 – Full planview of u/U for $z = 0,09$ m, with uv streamlines.

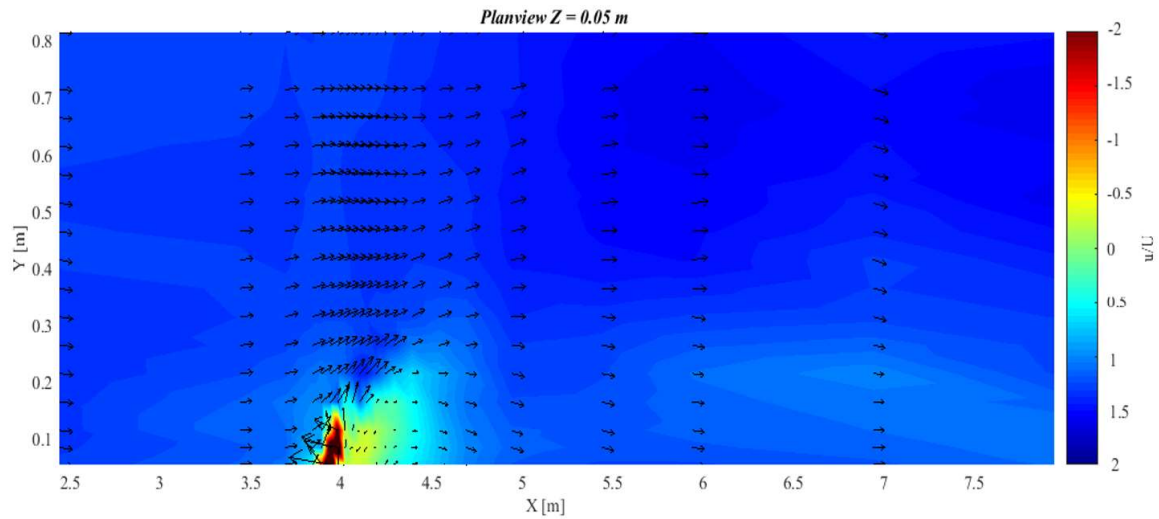


Figure 4.5 – Full planview of u/U for $z = 0,05$ m, with uv streamlines.

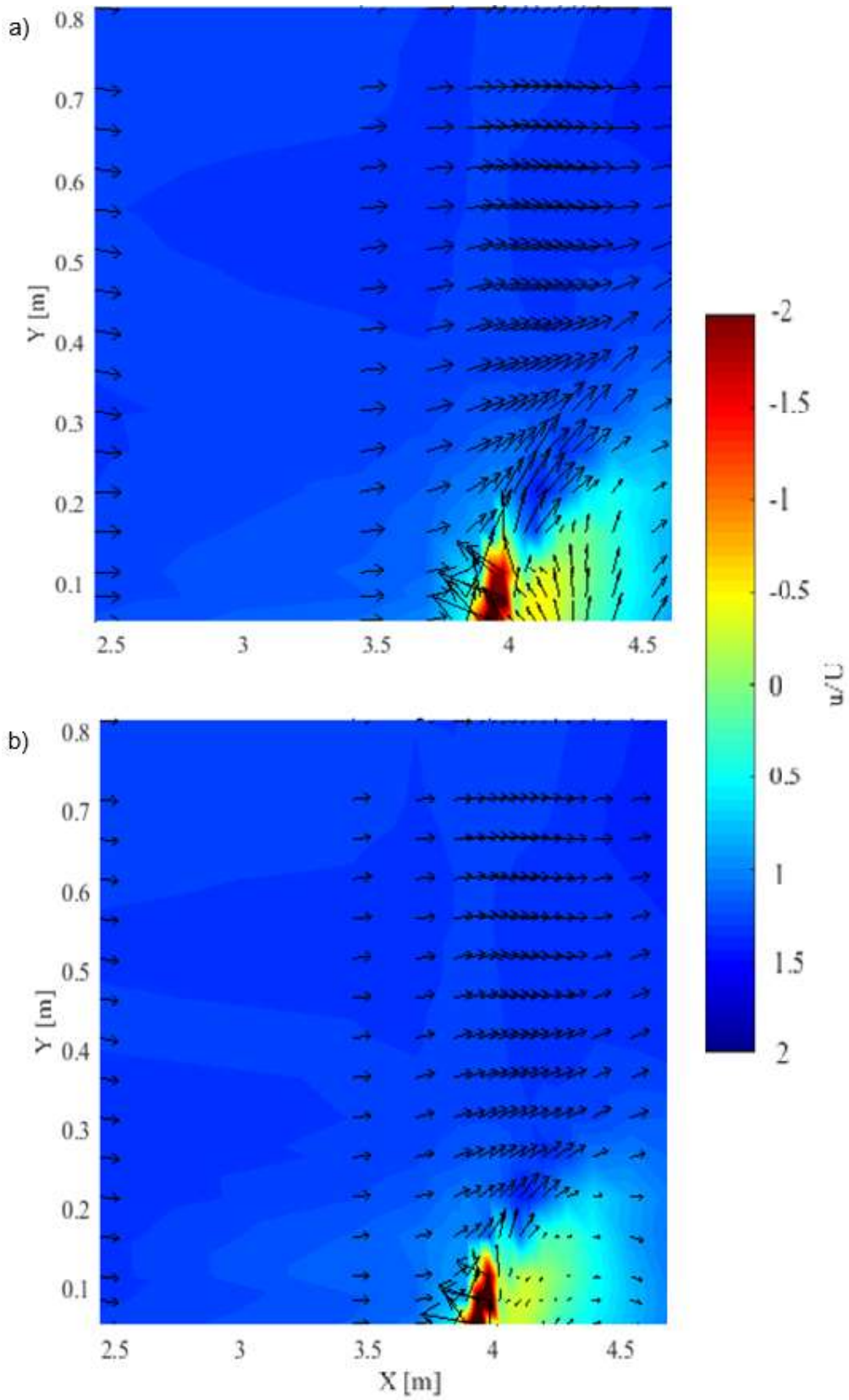


Figure 4.6 – a) Detail of u/U planview for $Z = 0,09$ m. b) Detail of u/U planview for $Z = 0,05$ m.

As the main channel flow reaches the confluence, velocity begins to decrease at the right bank. This probably happens because the tributary flow acts as a wall and effectively reduces the main channel flow velocities, deflecting it to the outer bank. It was also expected that a rise on the water level would be more pronounced than the actual rise of the experiment, near the inner bank at the stagnation zone [see Figure 4.2].

An increase of the transverse velocity, v/U , can be observed, starting at $x = 3,78 \text{ m}$ (Figure 4.7), which corresponds to the deflection caused by the transverse input of the tributary, creating a highly turbulent 3D flow field, and this velocity is greater near the surface, where the effect from the tributary is greater, due to the bed discordance between channels. The transverse velocity is greater near the inner bank and decreases with the distance from this bank, resulting in the flow near the outer bank being mostly unaffected by the tributary input for this cross-section.

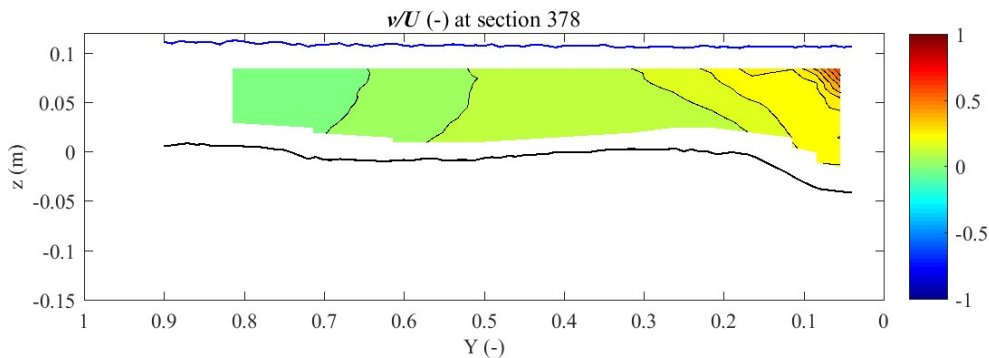


Figure 4.7 – v/U isolines at section $x = 3,78 \text{ m}$, depicting the deflection caused by the transverse input of the tributary.

Figure 4.6 a) and b) also portray the deflection effect. The flow direction starts deflecting as the confluence is approached and is stronger near the surface [Figure 4.6 a)]. If we compare this deflection with the bed topography presented on Figure 4.1, it is concluded that the flow deflection is related to the existence of the main channel mouth bar, and vice-versa.

On Figure 4.8 a), a clear shear layer is observed where flows from main and tributary channels intersect, created by strong velocity gradients. The relative velocities have negative values, portraying a direction opposite to the main channel flow direction. These shear layers are characterized by high turbulence intensity, generating a complex three-dimensional flow. By also observing a cross section near that area, an upwelling of the flow near the surface can be seen, as shown in Figure 4.8 b).

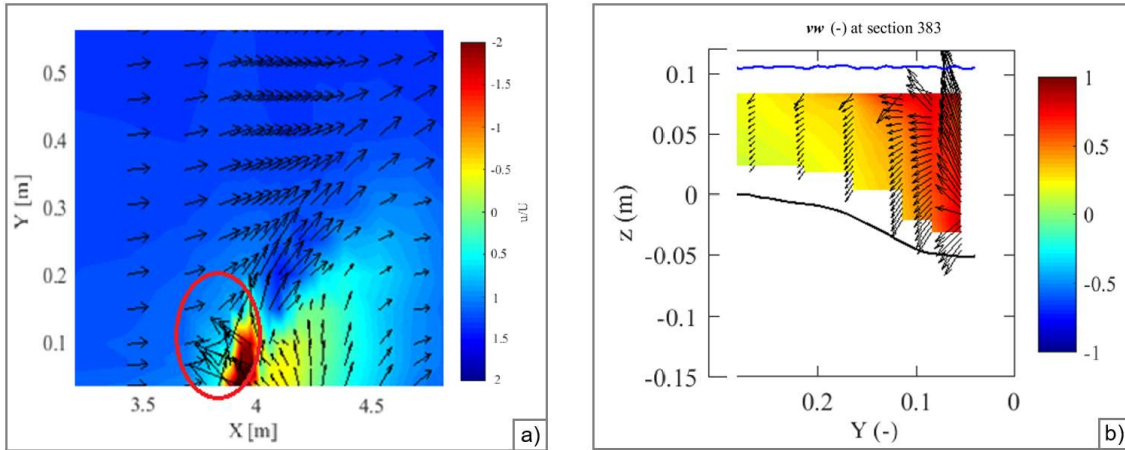


Figure 4.8 – Shear layer that starts upstream of the confluence on planview. b) Flow upwelling near the upstream corner of the confluence, on section $x = 3,83 m$.

By comparing the observed shear layer with the topography presented on Figure 4.1, a relation can be observed – the shear layer matches, almost perfectly, with the preferential flow corridor, or maximum velocity zone, delimited by the avalanche faces (Figure 4.9). At this zone the flow velocity is higher, as it delimits an area of the channel where the combined flows must pass. As such, this zone is of great importance regarding bed erosion and sediment transport, and is where the most accentuated bed scour is observed. Around 70% of the width of the main channel flow is affected and diverted by the action of the tributary. This effect can also be seen on Figure 4.9 by observing the upper red line.

As observed earlier, at $x = 3,80 m$ (the upstream corner of the confluence) the flow coming from the tributary is so strong that actually inverts the flow direction coming from the main channel, turning it upstream. The stagnation zone is pretty small due to this effect, although near zero velocities can be seen when observing the cross section at Figure 4.10. Scour starts appearing at this section and aggravates downstream.

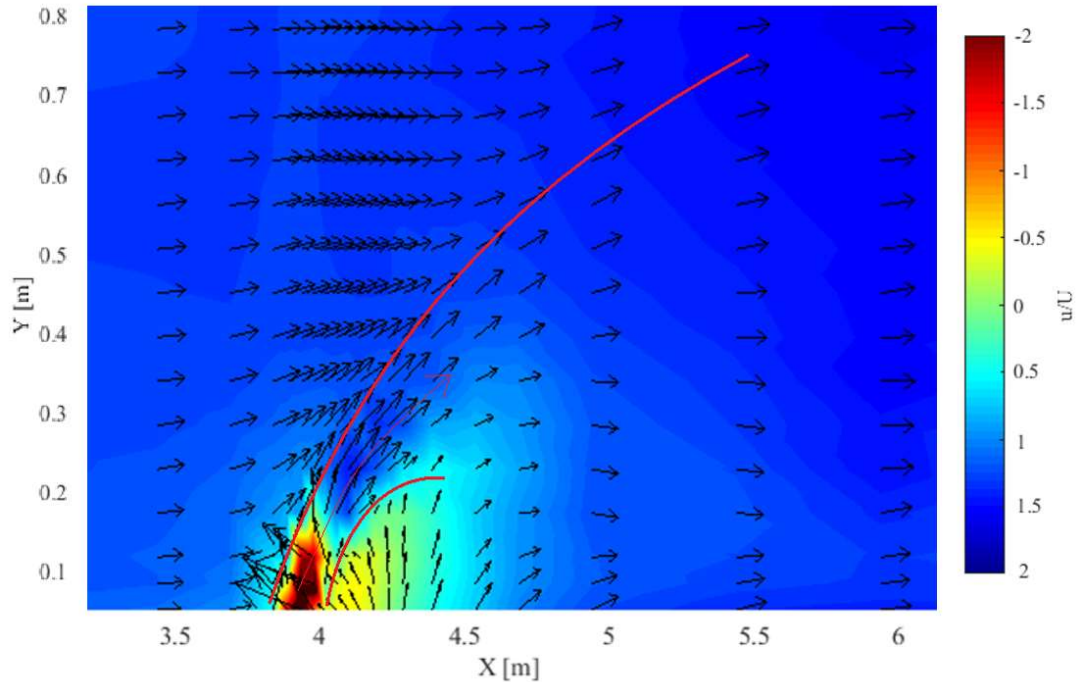


Figure 4.9 – Preferential corridor, or maximum velocity zone, delimited by shear layers.

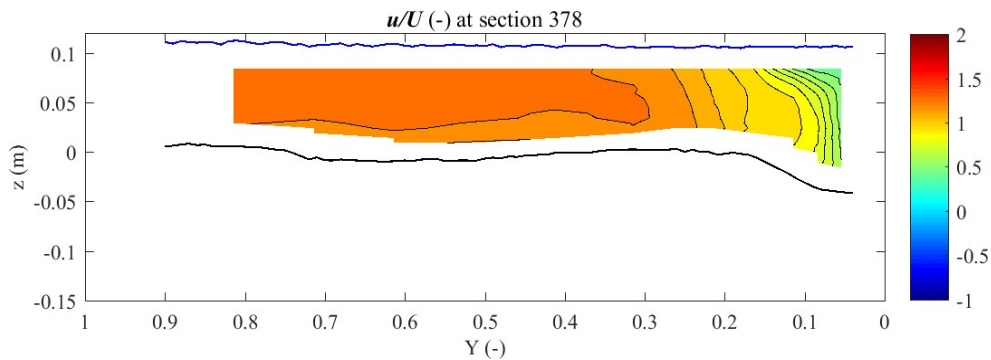


Figure 4.10 – u/U isolines at section $x = 3,78$ m, depicting the low velocities caused by the transverse input of the tributary.

Although this flow inversion phenomenon occurs, a part of the main channel flow plunges below the tributary flow, which can be hard to see in all cross sections, since there is no data of velocity when the distance relatively to the bed is approximately less than $0,02$ m. However, when observing the cross sections closely, the u component of the flow direction is above zero near the bed, which indicates that the flow from the main channel was not deflected by the tributary (Figure 4.11).

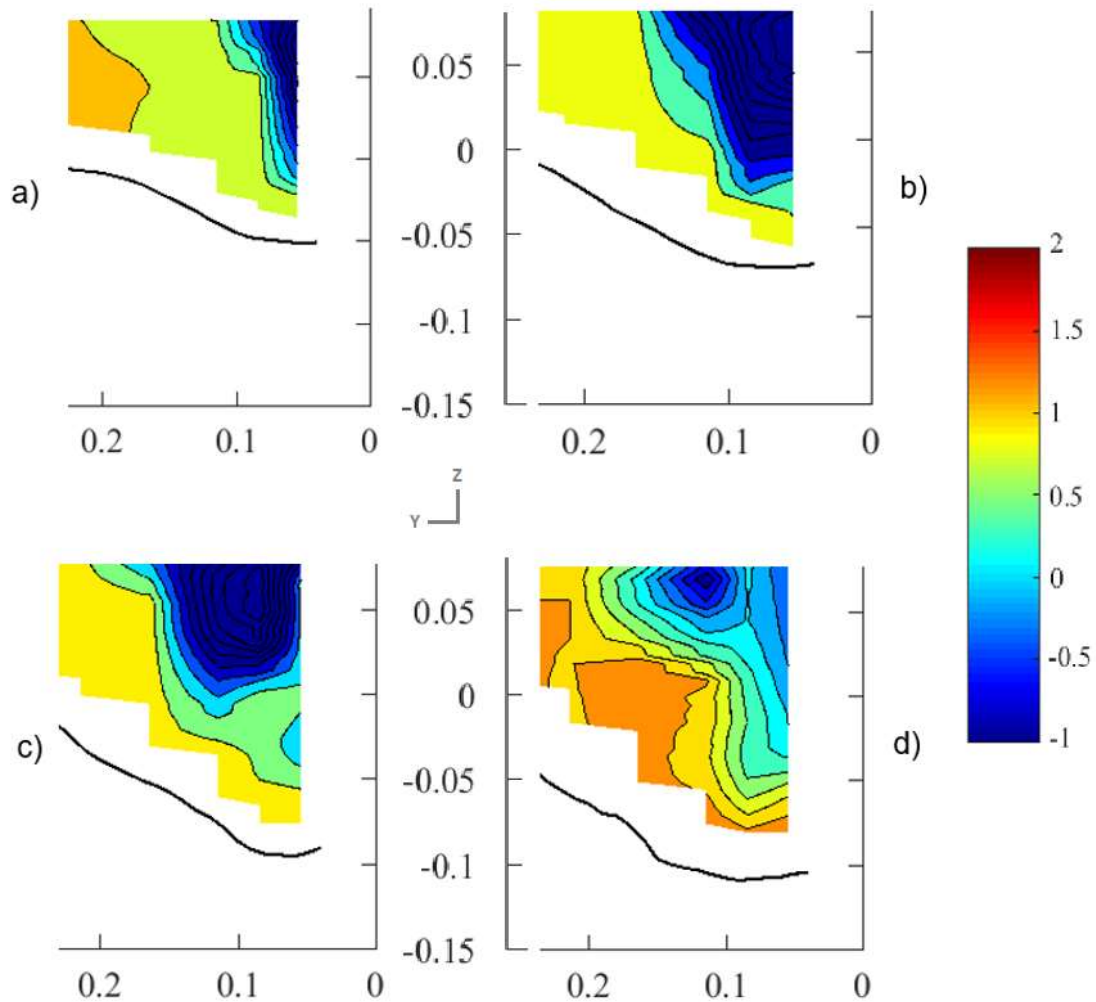


Figure 4.11 – Extract from cross sections $x = 3,83$ m (a), $x = 3,88$ m (b), $x = 3,92$ m (c) and $x = 3,96$ m (d), for u/U isolines, indicating passage of main channel flow below tributary flow.

The two-layer flow structure presented in Figure 4.11 is related to the existing bed discordance, which nullifies the model of flow recirculation described by Best (1987). However, Biron et al. (1996) foresaw this and described the flow upwelling generated by the bed discordance, which applies to the current study. This two-layer flow structure is composed by an upper layer and a lower layer. The upper layer consists of flow from the tributary channel, which enters the main channel with an angle that is slightly lower than the junction angle, obstructing the flow coming from the main channel. The lower layer flow consists of obstructed flow from the main channel, which flows under the upper layer flow. This lower layer collides with the bank-attached bar and leads to an upwelling zone near the downstream confluence junction corner (Figure 4.12). This near-bed flow prevents the formation of a zone of flow recirculation at this depth.

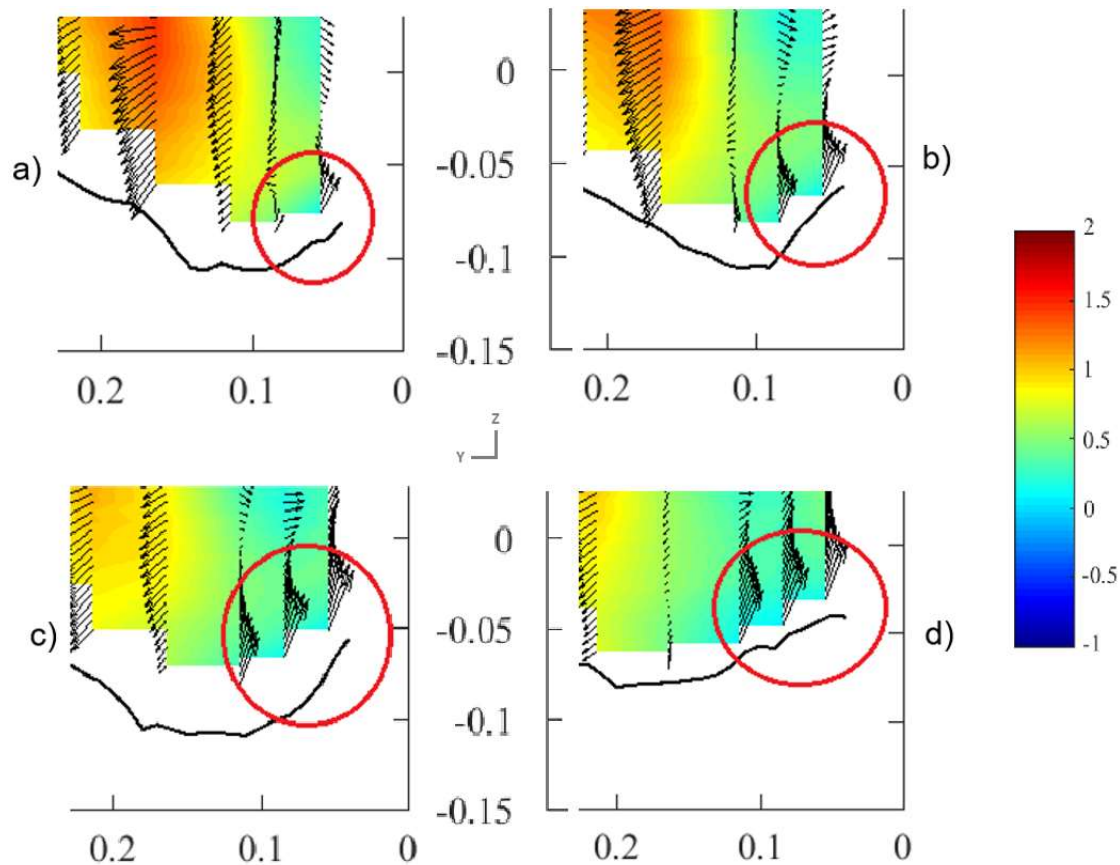


Figure 4.12 – Extract from cross sections $x = 4,00$ m (a), $x = 4,04$ m (b), $x = 4,08$ m (c) and $x = 4,13$ m (d), for v_w “streamlines”, indicating upwelling zone.

The difference between upper and lower layers of the flow lead to different layer velocities. This can be clearly seen by observing and comparing Figure 4.4 and Figure 4.5. As previously said, about 70% of the width of the flow is diverted by the action of the tributary near the surface. This changes drastically at deeper levels. At $z = 0,05$ m the affected width of the main channel flow is around 40%.

Starting at around $x = 4,00$ m, there is a relevant velocity decrease and flow recirculation occurs. This can be seen at Figure 4.13, and happens in a relatively small area. Recirculation happens near the inner bank until around $x = 4,40$ m, but with no data of the velocities to back it up – measurements at less than $\sim 0,05$ m from the inner bank were not made – it is hard to validate this assumption. This assumption was made based on observations of the flow *in situ*, by noticing small sand particles getting systematically trapped around this location.

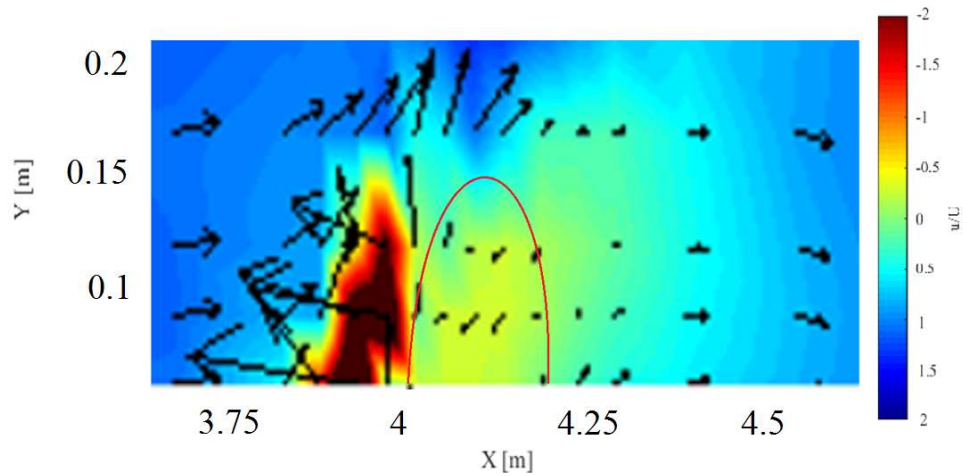


Figure 4.13 – Detail of the separation zone for $z = 0,05\ m$.

A separation zone is also formed near the surface, matching Biron et al. (1996) observations, although the velocity reduction is less significant (Figure 4.14). According to these observations, for discordant beds, even though the separation zone is destroyed near the bed, it does exist near the water surface. In the present study, however, the separation zone is more significant at a deeper depth than at the surface, weakening again as the bottom is reached. The most likely reason for this result discrepancy is the equilibrium state morphology used on the present experiment, which simulated mobile bed conditions, contrasting with the fixed bed conditions of Biron et al. observations. The separation zone location matches with the upstream-most part of the bank-attached bar, seen at Figure 4.1. Figure 4.15 overlays the planview of $z = 0,09\ m$ with the bed topography, which highlights the relevant interactions between hydrodynamics and morphology (full figures of this overlay, for both $z = 0,09\ m$ and $z = 0,05\ m$, can be analyzed at Appendix G).

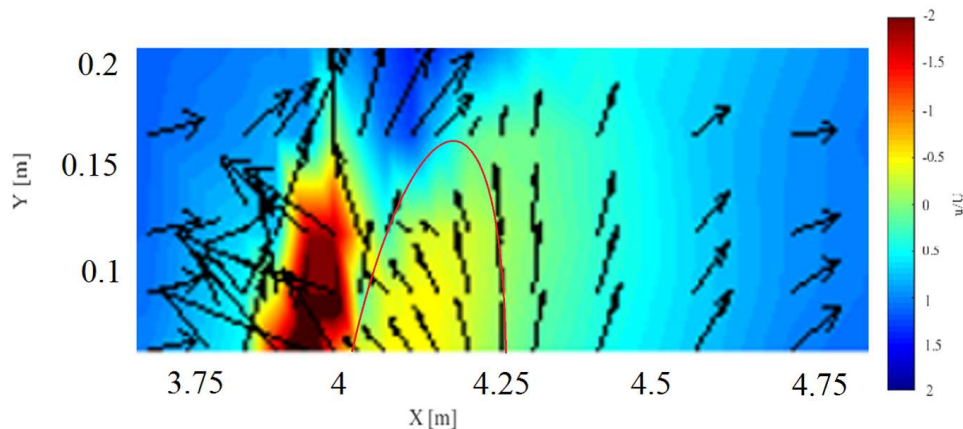


Figure 4.14 – Detail of the separation zone for $z = 0,09\ m$.

The maximum velocity zone, described at Figure 4.9, can be identified by observing Figure 4.15. This zone is initially delimited by both shear layers and scour walls, and then only by the later.

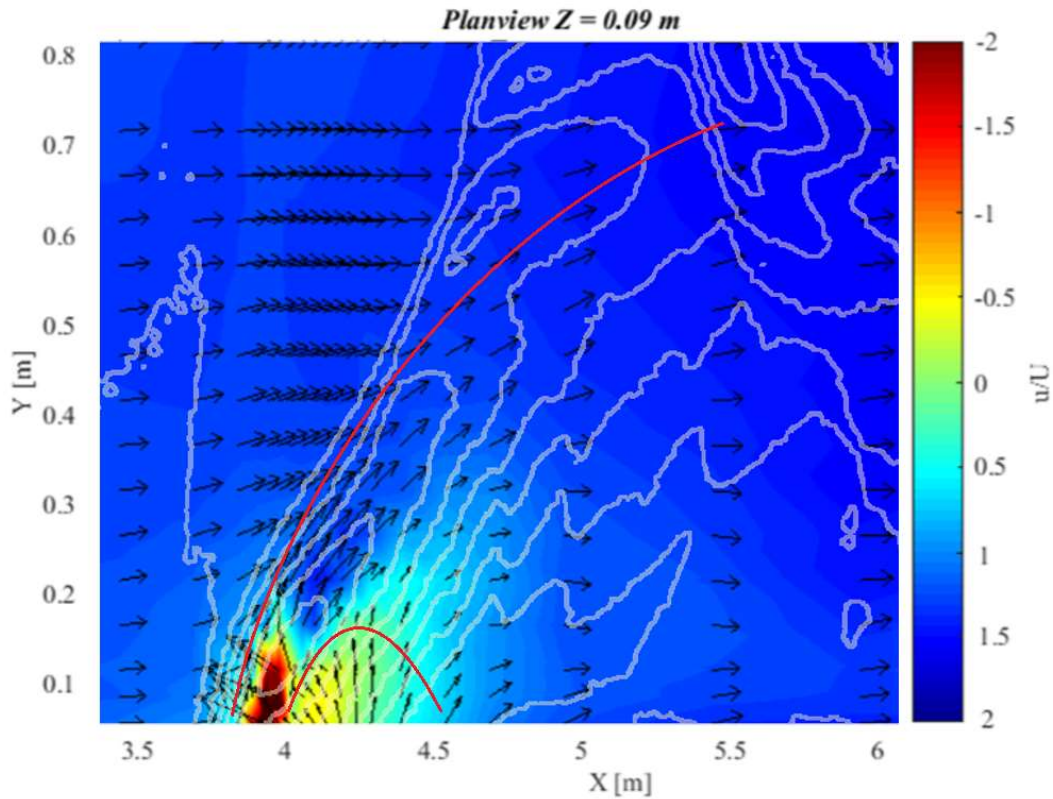


Figure 4.15 – Detail of u/U planview with bed topography and shear layer overlays.

The very strong vertical motion that is formed right near the downstream confluence junction corner (Figure 4.12) is the cause for the destruction of the separation zone near the bed, as mentioned before. Still, the separation zone exists for this zone at $z = 0,05 m$, where this vertical motion is much less significant, corroborating the observations made on Figure 4.13.

A slight helical cell is generated, which contradicts the starting assumptions. This can be observed starting at section $x = 4,00 m$ (Figure 4.16), where a helical motion can be observed. The helical motion persists until $x = 4,33 m$ (Figure 4.22), where the deflection effect, caused by the tributary, lowers. The streams from both channels remain mostly separated through the scour hole, mixing gradually downstream. This separation occurs due to vertical vortices on the shear layer.

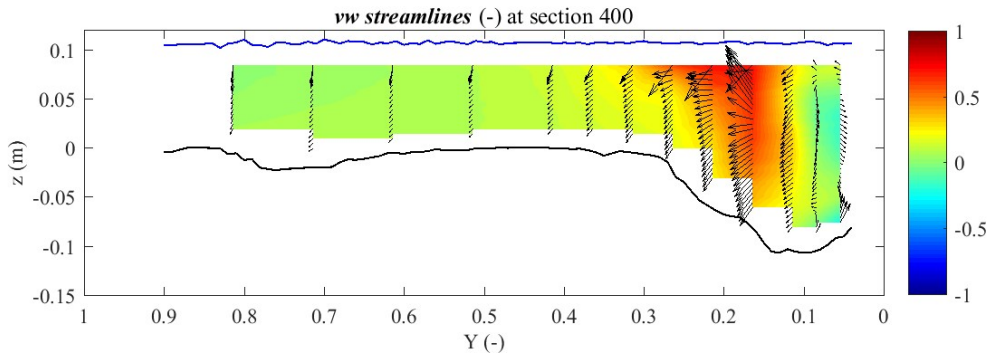


Figure 4.16 – vw “streamlines” at section $x = 4,00 m$.

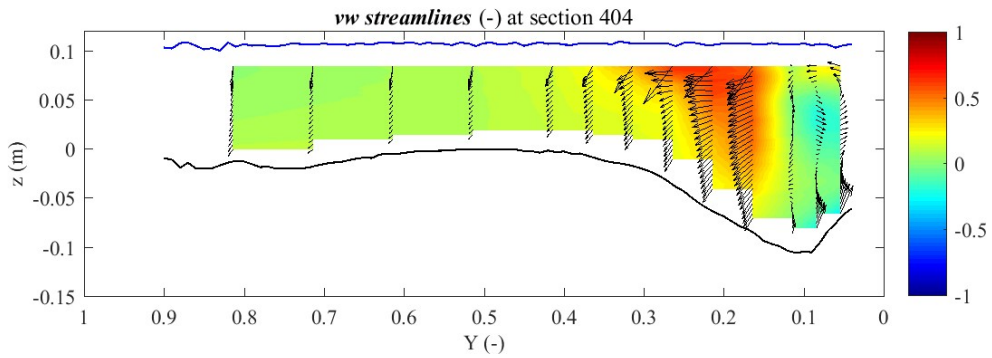


Figure 4.17 – vw “streamlines” at section $x = 4,04 m$.

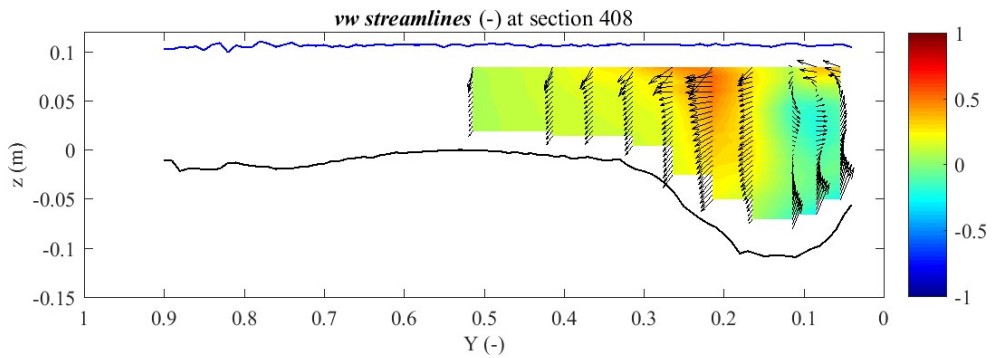


Figure 4.18 – vw “streamlines” at section $x = 4,08 m$.

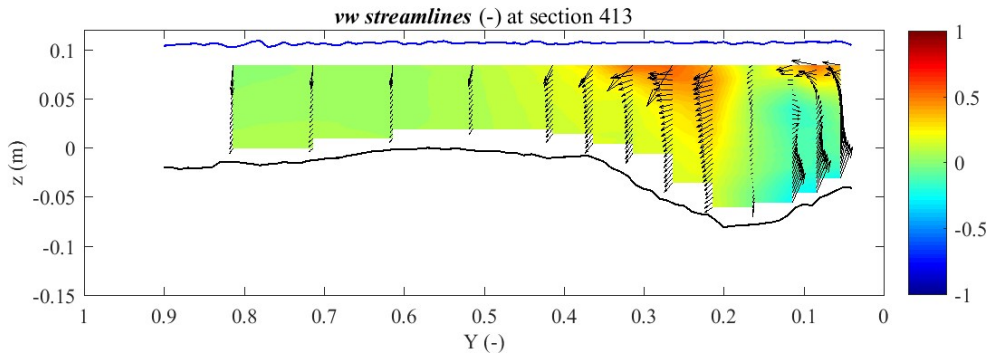


Figure 4.19 – vw “streamlines” at section $x = 4,13$ m.

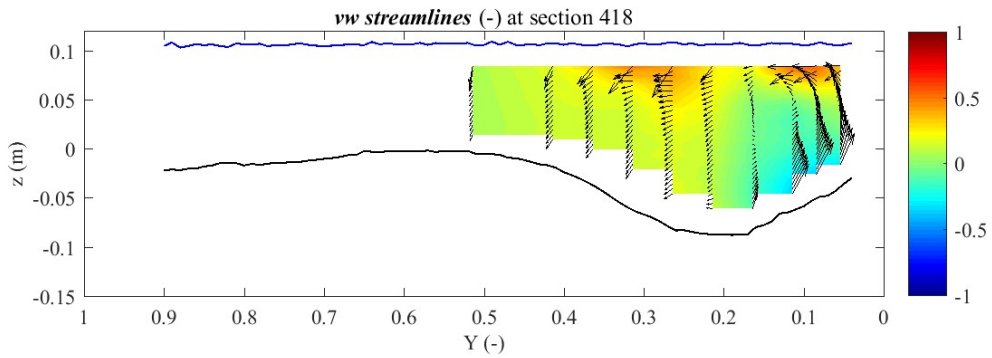


Figure 4.20 – vw “streamlines” at section $x = 4,18$ m.

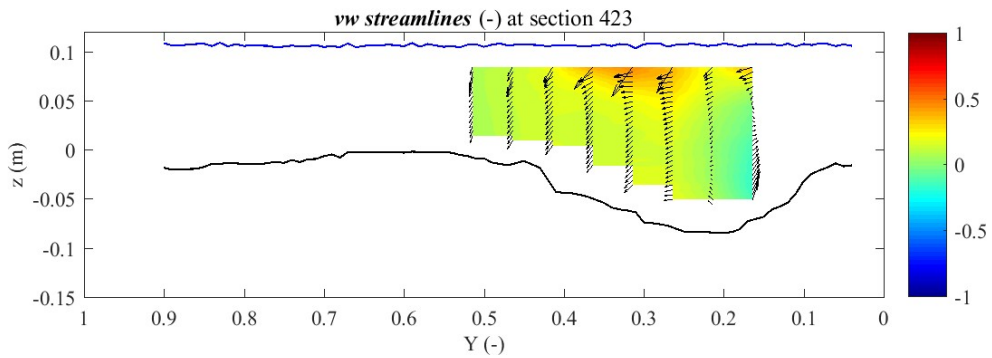


Figure 4.21 – vw “streamlines” at section $x = 4,23$ m.

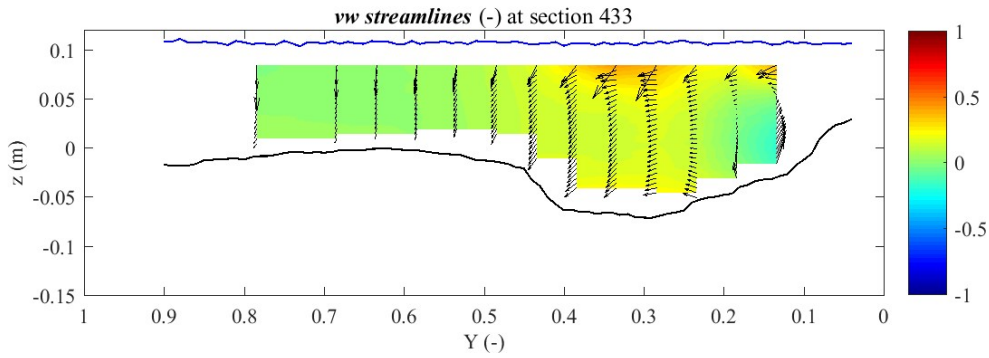


Figure 4.22 – vw “streamlines” at section $x = 4,33$ m.

Finally, the flow starts recovering at $x = 6,88$ m (Figure 4.23), slowly regaining its symmetrical properties, while both flows gradually mix and turbulence declines.

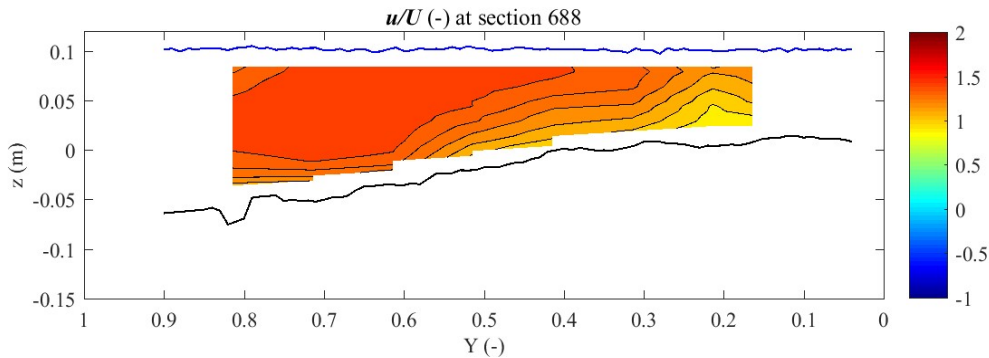
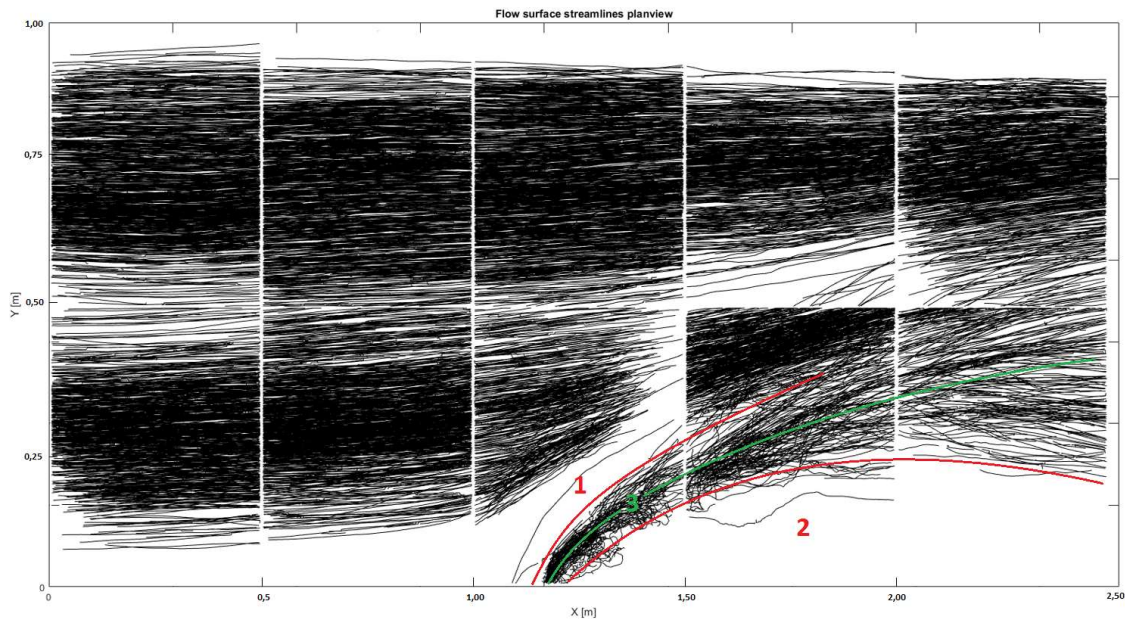


Figure 4.23 – u/U isolines at section $x = 6,88$ m, depicting the start of flow recovery.

A planview of the surface streamlines, portraying the major features of the present flow dynamics, can be seen at Figure 4.24. It should be noted that major flaws exist on this planview due to two important facts, regarding the experimental procedure. Firstly, the styrofoam balls were only dropped on the interval of Y that corresponded to the section being recorded (see the Y axis at Figure 4.24). This means that sections recorded on the left half of the channel only possess streamlines resulting of styrofoam balls dropped on this interval. The same applies to the right side of the channel. Secondly, the styrofoam balls were only dropped at a specific X section upstream of the confluence. This led to huge blank areas with no recorded trajectories. These flaws will be discussed on 5.1.

Both flaws could be easily avoided. For the first one, the styrofoam balls should have been dropped along the channel's full width for all runs. For the second one, the styrofoam balls should have been dropped at multiple positions along the channel length.



- 1 - Flow deflection zone**
- 2 - Low velocity zone**
- 3 - Maximum velocity zone**

Figure 4.24 – Flow surface streamlines planview.

On Figure 4.24, a maximum velocity zone can be observed (3), delimited by the flow deflection zone (1) and a low velocity zone (2), matching the observations portrayed at Figure 4.9. Particles can be seen with very unstable trajectories near the low velocity zone, describing vortex-like streamlines.

5 Result discussion

5.1 Introduction

This chapter is dedicated to the discussion of the results presented on the previous chapter, relating them to other studies. It will be divided into two sections – morphology and hydrodynamics – although some connections between them will inevitably be made.

5.2 Morphology

The flume bed presented a scour hole near the inner bank, approximately 0,175 *m* deep. According to Mosley (1976), this scour hole is a consequence of the flow structure on high angled confluences, which was the case of the present study. The scour walls define the shape of the scour and appear to have a curved shape, which progresses along with the tributary flow jet that penetrates the main channel. At the confluence area, the sediments flow preferentially along the scour walls instead of the bottom, joining further downstream (Best, 1988). These transport corridors slowly eroded the bed and ultimately formed the scour hole present on Figure 4.1.

It should be noted that Leite Ribeiro (2011) did not observe any scour hole on his experiments, which diverges from the current study. However, Guillén-Ludeña *et al.* (2015) also observed scour holes on his studies, which he explains with the differences of discharge ratios used. According to him, higher discharges for the same channel widths generate higher flow velocities on the confluence, which causes more pronounced bed erosion, resulting in a deeper scour hole.

The scour hole shape was connected with the plunging of the main channel flow under the tributary flow. This plunging is caused by the discordance between channels, creating a two-layer flow structure with strong vertical vortices, effectively eroding the bed and shaping the scour hole. The scour hole, caused by the clash of the main and tributary channel flows, extended downstream by approximately bisecting the junction angle, although with a slightly lower angle, while also having a curved shape, which coincided with the maximum velocity zone described by Best (1987).

The $\sim 0,05$ m discordance between channels is mostly due to the high sediment discharge rate, since the solid discharge per width on the tributary was 16,67 times greater than on the main channel. Although this ratio was higher than the one used by Leite Ribeiro (2011), the discordance was higher for his case, with the value of 0,09 m. On the other hand, the discharge ratio used by Leite Ribeiro (2011) was 0,11, lower than the discharge ratio of the present study, which was 0,16. It can then be concluded that the discordance depends on both discharge and sediment discharge.

Another important fact to be considered is the bed armouring phenomenon, which was observed by Leite Ribeiro (2011) on his studies. Bed armouring is caused by the granular segregation of the sediments, where larger particles cover the surface of the channel bed, effectively generating some protection against erosion. Similarly to the observations of Abreu (2015), this phenomenon did not occur on the present study, mostly due to the usage of an approximately uniform sand, which hinders the granular segregation required for the formation of bed armouring.

The bank-attached bar, which is proposed by Best (1988) as a feature of open channel confluences and was observed by Leite Ribeiro (2011), Guillén-Ludeña *et al.* (2015) and Abreu (2015), is present and occupies around 50% of the width of the channel, as seen on Figure 4.1. According to Leite Ribeiro (2011), the presence of this deposition bar at the inner bank when in presence of low discharge ratios is related to high sediment discharge ratios. On the other hand, according to Guillén-Ludeña *et al.* (2015), the formation of this bank-attached bar is related to the low velocity zone located near the downstream junction corner. Both claims can be observed on the present study, which features a low discharge ratio, high sediment discharge ratio and a recirculation zone, where flow velocities are low. The combination of these features, allied with the flow deflection, forces the tributary channel sediments to deposit on the inner bank, downstream of the confluence, forming the observed bank-attached bar.

5.3 Hydrodynamics

Most of the hydrodynamic features observed on the present experiment are similar to features of previous studies. The presence of upwelling flow and a flow separation zone along with flow recirculation, downstream of the confluence and on top of the bank-attached bar, was observed, as described for discordant confluences by Biron *et al.* (1996). This shows the applicability of results obtained from fixed bed to mobile bed experiments. However, the flow recirculation existed in a very small area, as seen on Figure 4.13, being more significant at

mid-depth of the flow than near the surface. Near the bottom, the separation zone was destroyed by the upwelling, as seen on Figure 4.11. This separation zone destruction by upwelling flow was also described by Biron et al. (1993), Biron et al. (1996) and Leite Ribeiro (2011).

Near the confluence, the flow features two layers, where the main channel flow, which represents the lower layer, plunges below the tributary channel flow, which represents the upper layer. This feature is characteristic of confluences that possess discordance, as described by Biron et al. (1996), and low discharge ratios, as described by Leite Ribeiro (2011). This structure results in a very strong vertical motion, already described as the upwelling, formed close to the downstream junction corner and near the bottom, which prevents the formation of the separation zone above the bank-attached bar, at higher depths. The vertical motion is much less significant near the surface, resulting in the existence of the separation zone and flow recirculation.

An area of flow recirculation was observed downstream of the confluence, as seen on area 1 of Figure 5.1. Air bubbles were observed to ascend between the bottom and the water surface at area 1 of Figure 5.1, which was caused by detachment of the tributary channel flow from the right bank, due to the abrupt change on the channel geometry. The flow recirculation was not very significant, mostly because of the flume's state of equilibrium.



Figure 5.1 – Detail of flow surface near the confluence (flume not on equilibrium).

This generated a vertical vortex that induced hydraulic head loss, creating a low-pressure zone, which effectively lowered the water level for that area (Figure 5.2, zone 2). The water level is restored further downstream, as seen on Figure 5.2.

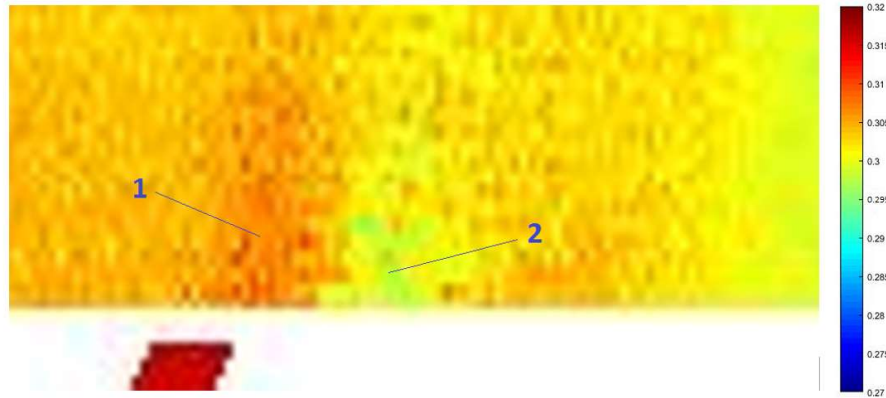


Figure 5.2 – Detail of the water level 2D view.

The clash between both channels created a deflection zone, as seen on Figure 5.1. The deflection zone is clearly related with the formation of the main channel mouth bar, since it mostly matches its position along its extension (Figure 4.9 and Figure 4.15). This deflection zone is also related with the mixing layer (Best and Roy, 1991). A stagnation zone is present near the upstream junction corner. Although its area is relatively small, when compared to the study of Best (1987), it is observable in Figure 4.10. The stagnation zone is characterized by rise of the water level, the start of flow deflection and a great flow deceleration, as described by Leite Ribeiro (2011). All these characteristics were observed on the present study, which corroborates his hypothesis: water level rise at Figure 5.2, zone 1 (It was also expected that a rise on the water level would be more pronounced than the actual rise of the experiment); start of flow deflection at Figure 4.9 and Figure 4.15; great flow deceleration at Figure 4.10.

The existence of the bank-attached bar reduces the flow cross-section area and induces the maximum velocity zone. Downstream of the stagnation zone, the preferential flow corridor, or maximum velocity zone, is present, delimited by the avalanche faces (Figure 4.9). At this zone the water level rises (Figure 5.2, zone 1) and the flow velocity is higher, as it delimits an area of the channel where the combined flows must pass, effectively generating a more accentuated bed scour. The beginning of the formation of the bed scour and the maximum velocity zone can be observed at Figure 5.1, zone 3.

A slight single helical cell is generated which, according to most studies, contradicts the starting assumptions where no helical cells would be observed, as this usually does not occur on confluences with discordant bed. This can be observed starting at section $x = 4,00 \text{ m}$ (Figure 4.16), where a helical motion can be observed. The helical motion persists until $x = 4,33 \text{ m}$ (Figure 4.22), where the deflection effect, caused by the tributary, lowers.

The flow coming from the tributary is so strong that actually inverts the flow direction coming from the main channel, turning it upstream, which results in the negative velocities observed at numerous instances, such as Figure 4.14. Although this phenomenon is interesting, it does not occur on other studies, which makes it dubious. By observing Figure 4.24, it can be concluded that no streamlines appear to be flowing upstream, further deepening the dubious nature of these negative velocities. This phenomenon could have only been caused by very significant flow instability at this area, which was the case. By analyzing the measured data, it was concluded that the measured values for u systematically fluctuate between low positive and high negative values, supporting this hypothesis. The resultant average is a relatively high negative value for u , generating the upstream pointed velocity vectors. On the other hand, the measured velocities were made at around 0,02 m underwater, where the turbulence conditions could have been different from the surface conditions, where the streamlines are observed.

Further downstream, the flow recovers and gradually adopts its initial symmetrical properties, while both flows gradually mix and turbulence declines (Figure 4.23), a behavior that is observed as long as the length of the post-confluence channel allows it. According to Biron et al. (2004), complete mixing for a discordant bed case can occur between 25 and 55 channel widths, corresponding to a natural site and a laboratory channel, respectively. The channel of the current study only has approximately 4 channel widths, so a complete mix between flows is not expected.

6 Conclusion

6.1 Conclusions

The flow structure spatial evolution of an open-channel confluence, with a junction angle of 70° and low discharge and width ratios, was investigated through experimental tests, using a low intrusion method for measuring the flow velocities, the Vectrino probe. The hydrodynamic results are represented through cross sections with isolines for three dimensions, cross-sectional flow directions and planviews with isolines and streamlines. Simple morphological results are also presented through 2D and 3D figures. The final results allow the identification of morphological and hydrodynamic differences between the current study and other studies.

From the velocity and streamlines profiles it was concluded that the flow behaved approximately according to the expectations, with some exceptions. In fact, the flow appeared to have most features that were considered after analyzing the existing literature: a flow deflection zone, a maximum velocity zone, shear layers delimiting these zones and a flow recovery zone. The flow separation zone had some differences, as its existence depended on the depth being considered. There was presence of a helical cell between $x = 4,00$ m and $x = 4,33$ m, which was not expected.

The measurements of the three-dimensional flow structure show how complex these are on open-channel confluences. Due to the slight bed discordance, the tributary flow penetrates the main channel mostly through the upper part of the water column, generating a two-layer flow configuration. On the other hand, the main channel flow is less affected on the lower part of the water column, which generates a two-layer flow near the tributary mouth. This two-layer flow configuration coincides with the description provided by Biron et al. (1996), for fixed bed channels, and is present in most studies of confluences with bed discordance, such as the work of Leite Ribeiro (2011).

A large bank-attached bar was present downstream of the confluence. This is a recurrent feature of confluences where tributaries have a large sediment supply, as observed by Leite Ribeiro (2011) and Abreu (2015). This bar effectively reduces the flow area and causes flow acceleration between the bar and the left bank. Near the downstream junction corner a recirculation zone was present, although with low significance. This low significance

was mainly caused by the equilibrium state of the flume, which contrasts with most studies, mainly those of fixed bed where the recirculation zone is very pronounced.

The scour hole was very pronounced, reaching a height difference between the deeper zone and the average upstream height of 0,175 *m*, much higher than other studies, such as Leite Ribeiro (2011) where there was no scour hole present, which was replaced by a preferential corridor instead (with similar height as the upstream main channel), and Abreu (2015), where this scour reached 0,10 *m*. This can be mostly explained by the relatively high unit sediment discharge on the tributary channel and the high unit sediment discharge ratio, when compared with these studies.

In summary, the present study suggests that when confluences feature high tributary sediment supply, bed discordance occurs and a relatively large bank-attached bar is formed. On the other hand, in the presence of the combination of high tributary sediment discharges and low tributary widths, the bed erosion is greatly enhanced at the scour zone, resulting in a greater scour hole. This combination also enhances the water jet flowing from the tributary channel, consequently enhancing the flow deflection, causing approximately 70% of the width of the main channel flow direction being affected and deflected by the action of the tributary.

Although the main objective of this study was to characterize the flow on confluences with low discharge ratios, the observed morphology, which is intrinsically connected with the hydrodynamics, can also represent great interest on river intervention projects. Using this knowledge, confluences which present similar control variables and parameters can be better interpreted, rendering possible rehabilitation and future interventions easier. It should be noted that the model used on the experiments had rigid margins, a fact that does not occur on natural rivers, which might result in a different bed morphology.

6.2 Limitations and Improvements

Laboratory experiments are limited by the low number of configurations that cannot cover all the relevant aspects of a specific experimental study. At the present study, this fact obviously impoverishes it, since only one configuration was possible to be studied. Moreover, the conditions were simplified, since it was done on a “frozen bed” in equilibrium conditions. An interesting study would be the investigation of different stages of the scour, which would make the characterization of its evolution possible.

The measurements could have had more coverage. Since the Vectrino probe used was sidelooking, the flow structure near the bed was left with no data, which makes

interpretation of this area a hard task. A downlooking probe should have been used to cover this problem. On the other hand, the grid could have been denser, favoring a more characterized flow on certain key areas, such as the scour hole.

Major flaws existed on the recording of the surface streamlines due to bad practices during the experiment, which could be easily avoided.

Possible improvements for this case study would be:

- Using more configurations, in terms of discharge ratios, width ratios or even solid discharge ratios at the preliminary stage.
- Using different measuring methods, such as a downlooking Vectrino probe or a PIV probe. A comparison between results could be made, which would increase their quality.
- Characterizing the turbulent flow field.
- Using a denser velocity measuring grid.
- Characterizing the scour hole evolution.
- Adding the tributary channel to the velocity measuring grid.

References

Abreu, P. (2015). Alterações morfológicas induzidas pelo alargamento da foz de um afluente numa confluência fluvial. Instituto Superior Técnico, Lisbon, Portugal.

Best, J. L., and Reid, I. (1984). Separation Zone at Open-Channel Junctions. *Journal of Hydraulic Engineering*, 110(11), 1588-1594. doi:10.1061/(ASCE)0733-9429(1984)110:11(1588)

Best, J. L. (1987). Flow dynamics at river channel confluences. Implications for sediment transport and bed morphology. *Recent developments in Fluvial Sedimentology, Spec. Publ. SEPM Soc. Sediment. Geol.*, (39), 27-35. doi:10.2110/pec.87.39

Best, J. L. (1988). Sediment transport and bed morphology at river channel confluences. *Sedimentology*, 35(3), 481-498. doi:10.1111/j.1365-3091.1988.tb00999.x

Best, J. L. (2008). Sediment transport, bed morphology and the sedimentology of river channel confluences. In S. P. Rice, A. G. Roy, & B. L. Rhoads (Eds.), *River Confluences, Tributaries and the Fluvial Network* (pp. 45-72). Chichester, UK: John Wiley & Sons, Ltd. doi:10.1002/9780470760383.ch4

Best, J. L., and Roy, A. G. (1991). Mixing-layer distortion at the confluence of channels of different depth. *Nature*, 350(6317), 411-413. doi:10.1038/350411a0

Biron, P., Roy, A.G., Best, J.L., and Boyer, C.J. (1993). Bed Morphology and sedimentology at the confluence of unequal depth channels, *Geomorphology*, 8, 115-129.

Biron, P. M., Best, J. L., and Roy, A. G. (1996a). Effects of Bed Discordance on Flow Dynamics at Open Channel Confluences. *Journal of Hydraulic Engineering*. doi:10.1061/(ASCE)0733-9429(1996)122:12(676)

Biron, P. M., Roy, A. G., and Best, J. L. (1996b). Turbulent flow structure at concordant and discordant open-channel confluences. *Experiments in Fluids*. doi:10.1007/BF00189046

Bristow, C. S., Best, J. L., and Roy, A. G. (1993). Morphology and facies models of channel confluences. In M. Marzo & C. Puigdefábregas (Eds.), *Alluvial Sedimentation* (pp. 91-100). Ltd, Oxford, Uk. doi:10.1002/9781444303995.ch8

- Guillén-Ludeña, S., Franca, M.J., Schleiss, A.J., and Cardoso, A.H. (2014). Morphodynamic differences induced by different confluence angles in widen confluences, In A. J. Schleiss, G. de Cesare, M. J. Franca, & M. Pfister (Eds.), *River Flow 2014* (pp. 983–988). CRC Press 2014. doi:10.1201/b17133-133
- Hager, W. H. (1989). Transitional Flow in Channel Junctions. *Journal of Hydraulic Engineering*, 115(2), 243-259. doi:10.1061/(ASCE)0733-9429(1989)115:2(243)
- Hsu, C.-C., Lee, W.-J., and Chang, C.-H. (1998a). Subcritical Open-Channel Junction Flow. *Journal of Hydraulic Engineering*. doi:10.1061/(ASCE)0733-9429(1998)124:8(847)
- Leite Ribeiro, M. (2011). Influence of Tributary Widening on Confluence Morphodynamics. École Polytechnique Fédéral de Lausanne, Lausanne, Switzerland.
- Mosley, M. P. (1976). An experimental study of channel confluences. *Journal of Geology*, 84(5), 535-562.
- Ramamurthy, A. S., Carballada, L. B., and Tran, D. M. (1988). Combining Open Channel Flow at Right Angled Junctions. *Journal of Hydraulic Engineering*, 114, 1449-1460. doi:10.1061/(ASCE)0733-9429(1988)114:12(1449)
- Rhoads, B. L., and Ramamurthy, S. T. (1995). Flow structure at an asymmetrical stream confluence. *Geomorphology*, 11(4), 273-293. doi:10.1016/0169-555X(94)00069-4
- Rhoads, B. L., and Kenworthy, S. T. (1995). Time-averaged flow structure in the central region of a stream confluence. *Earth Surface Processes and Landforms*, 23(2), 171-191. doi:10.1002/(SICI)1096-9837(199802)23:2<171::AID-ESP842>3.0.CO;2-T
- Rhoads, B. L., and Sukhodolov, A.N. (2001). Field investigation of three-dimensional flow structure at stream confluences: 1. Thermal mixing and time-averaged velocities. *Water Resources Research*, 37(9), 2393-2410. doi:10.1029/2001WR000316
- Rhoads, B. L., and Sukhodolov, A. N. (2004). Spatial and temporal structure of shear layer turbulence at a stream confluence. *Water Resources Research*. doi:10.1029/2003WR002811
- Ribeiro, L. (2011). Influence of Tributary Widening on Confluence Morphodynamics. *École Polytechnique Fédérale de Lausanne*.
- Shabayek, S., Steffler, P., and Hicks, F. E. (2002). Dynamic Model for Subcritical Combining Flows in Channel Junctions. *Journal of Hydraulic Engineering*, 128(9), 821-828. doi:10.1061/(ASCE)0733-9429(2002)128:9(821)

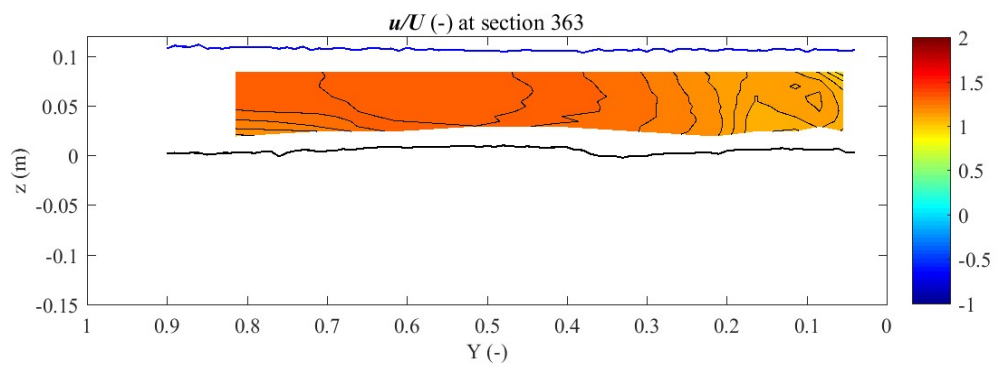
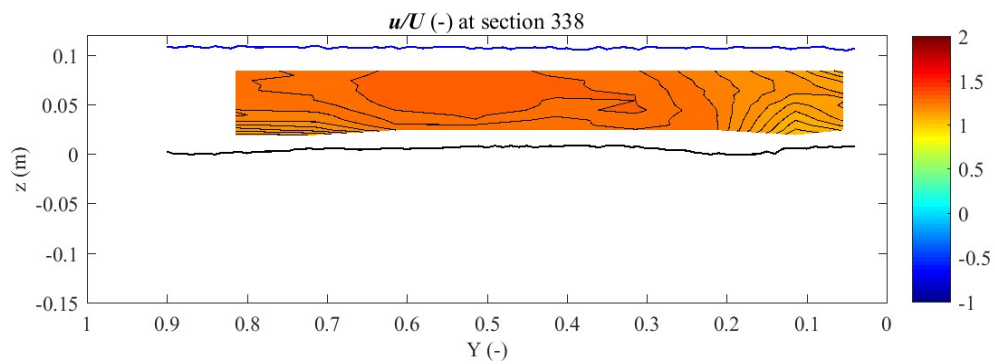
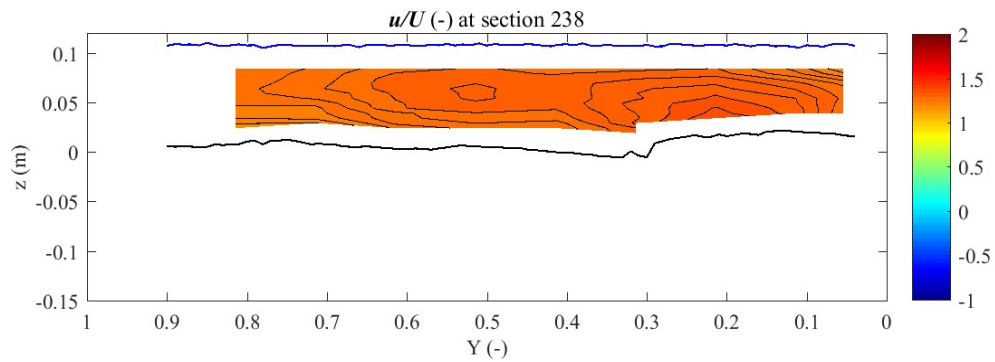
Sukhodolov, A. N., and Rhoads, B. L. (2001). Field investigation of three-dimensional flow structure at stream confluences: 2. Turbulence. *Water Resources Research*, 37(9), 2411-2424. doi:10.1029/2001WR000317

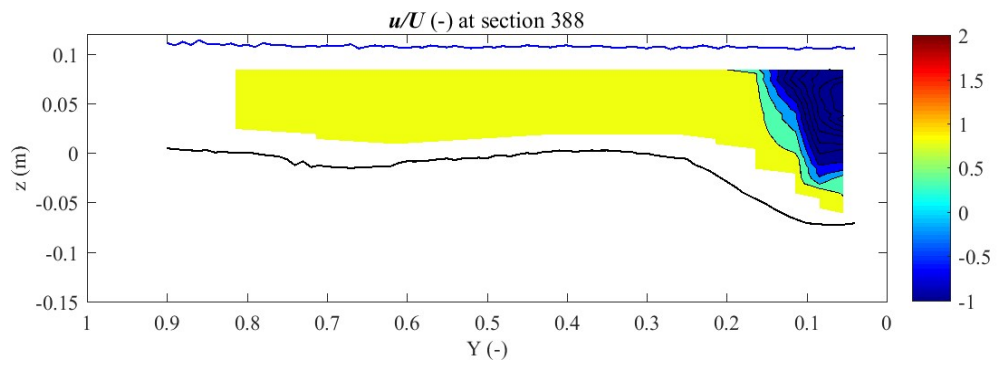
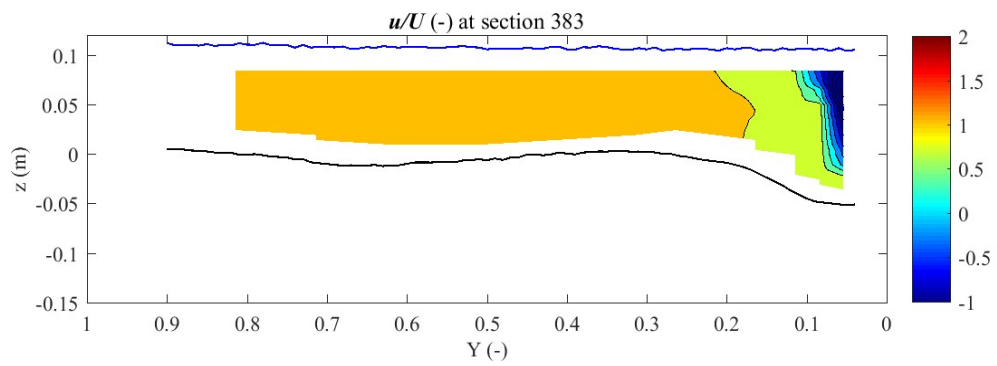
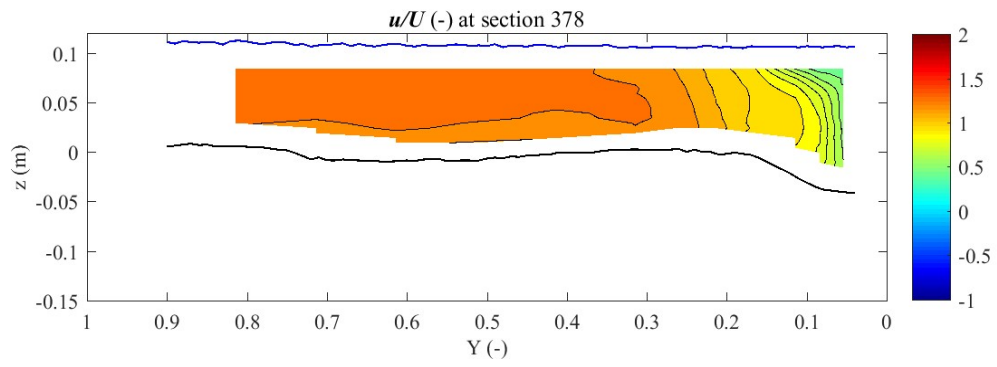
Taylor, E. H. (1944). Flow characteristics at rectangular open-channel junctions. *American Society of Civil Engineers*, 70, 119-121.

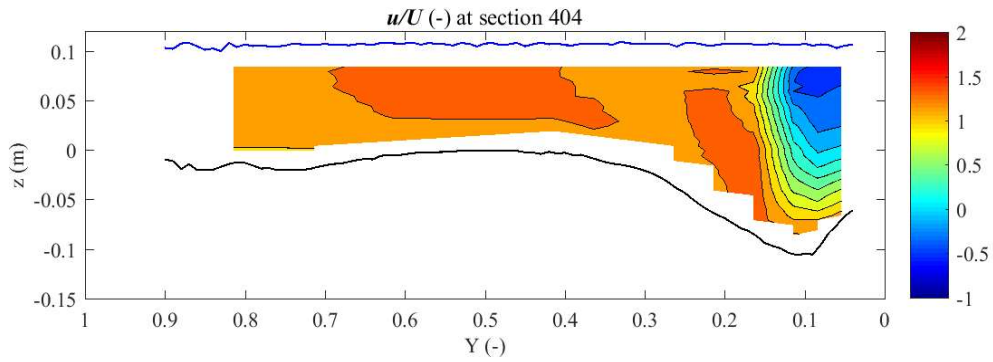
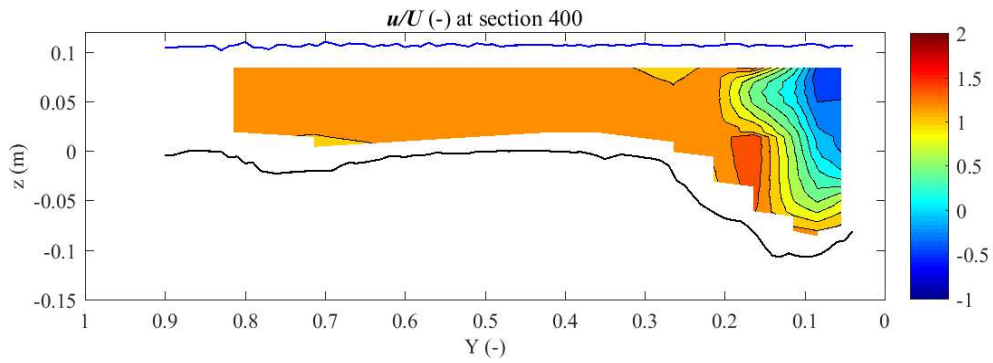
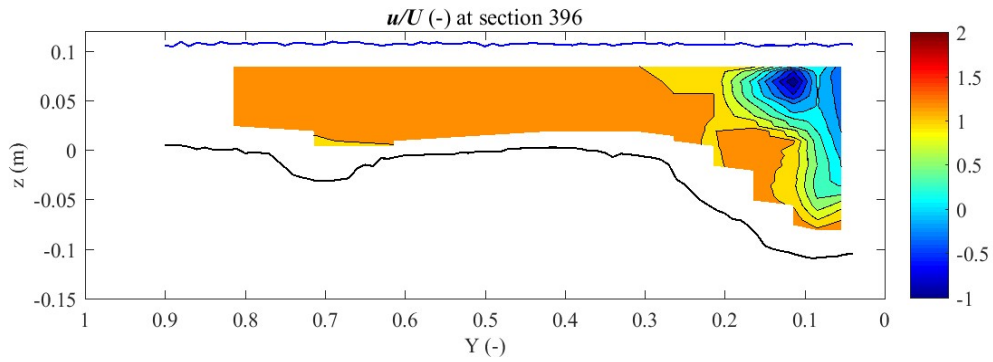
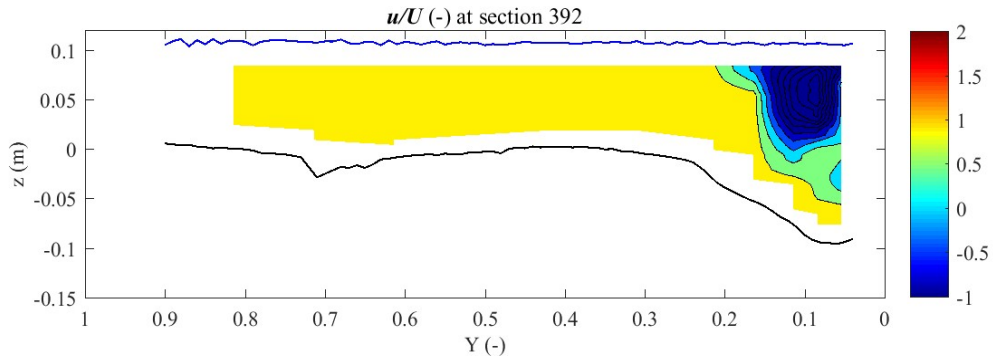
Webber, N. B., and Greated, C. A. (1966). An investigation of flow behavior at the junction of rectangular channels. *Proceedings of Institute of Civil Engineers*, 34(3), 321-334. doi:10.1680/iicep.1966.8925

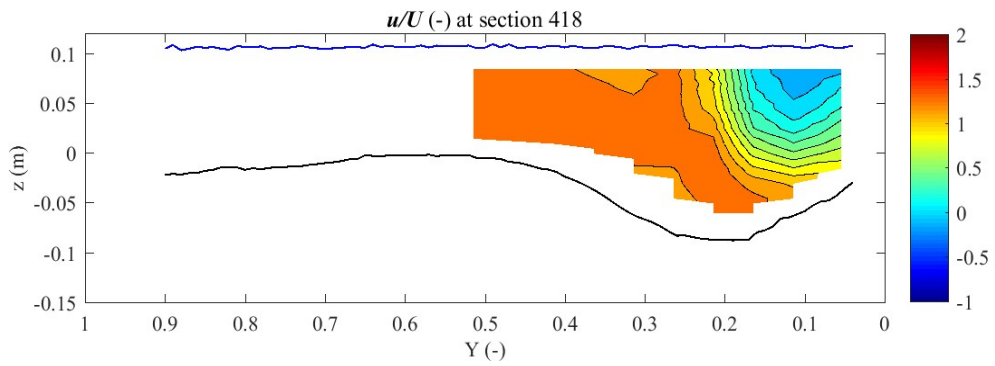
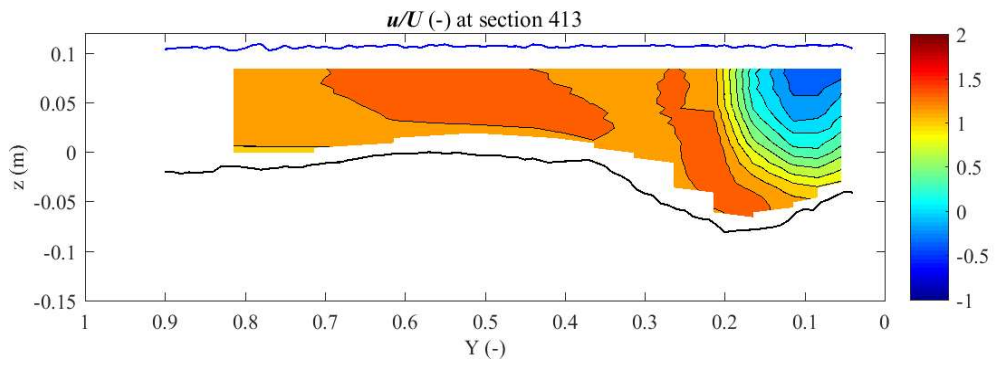
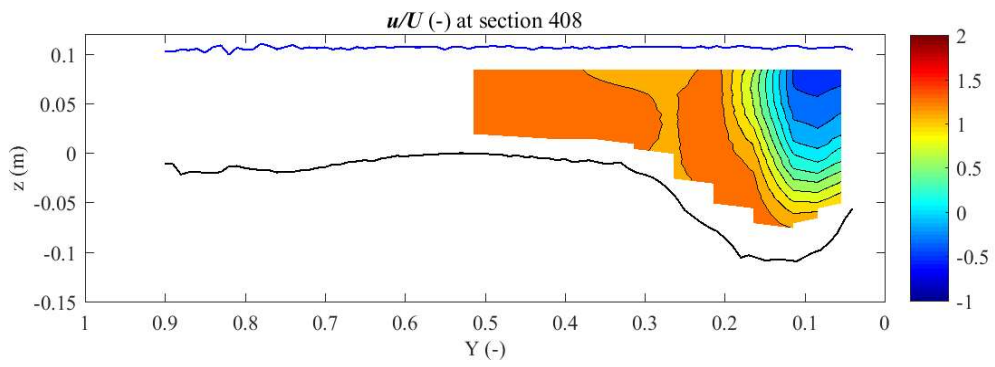
Appendices

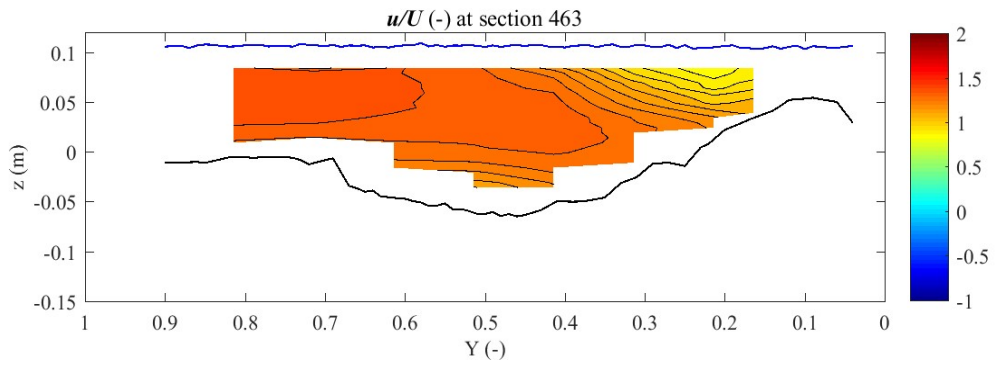
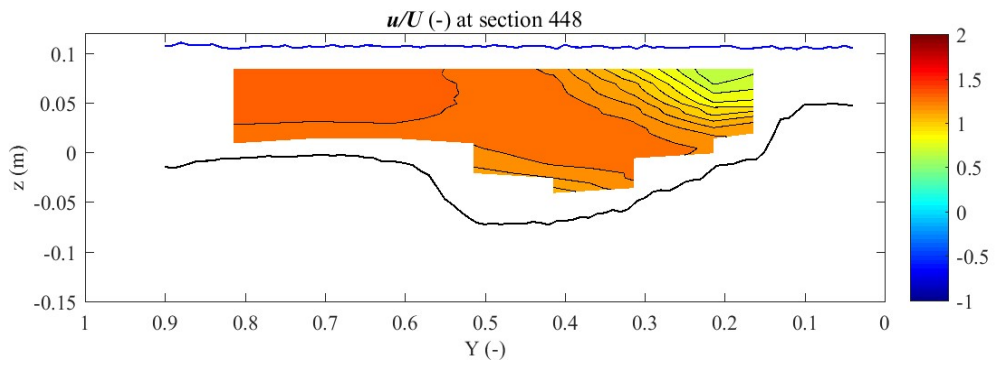
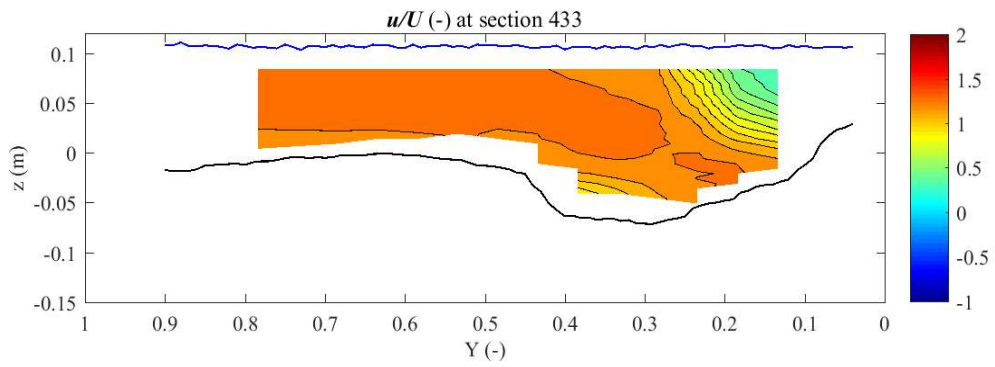
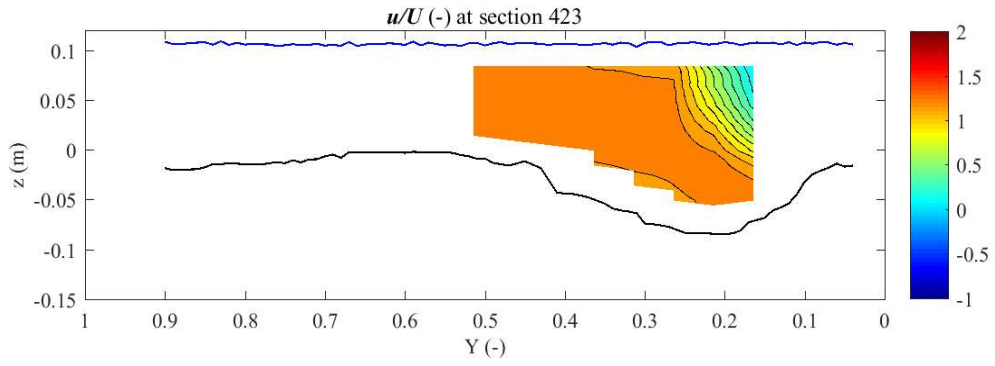
Appendix A – u/U isolines

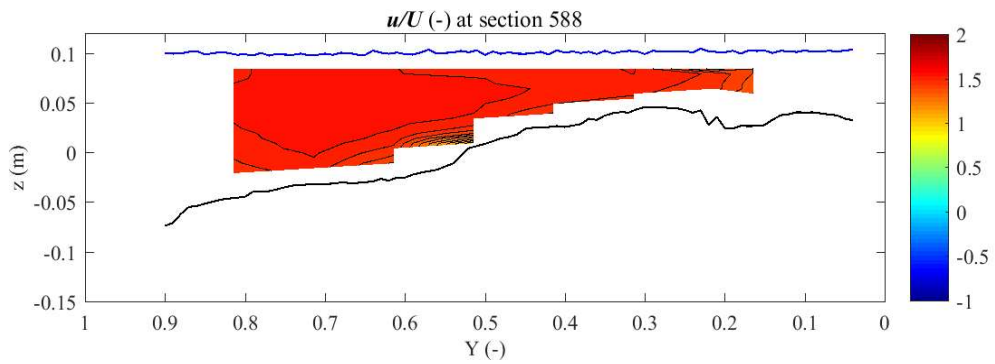
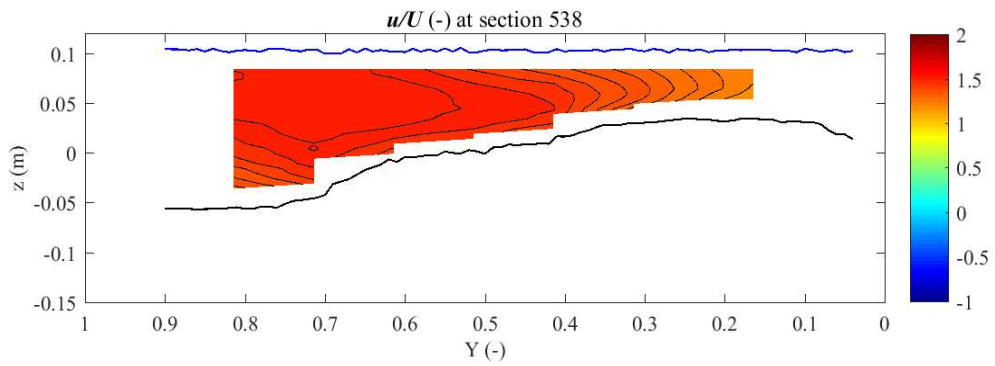
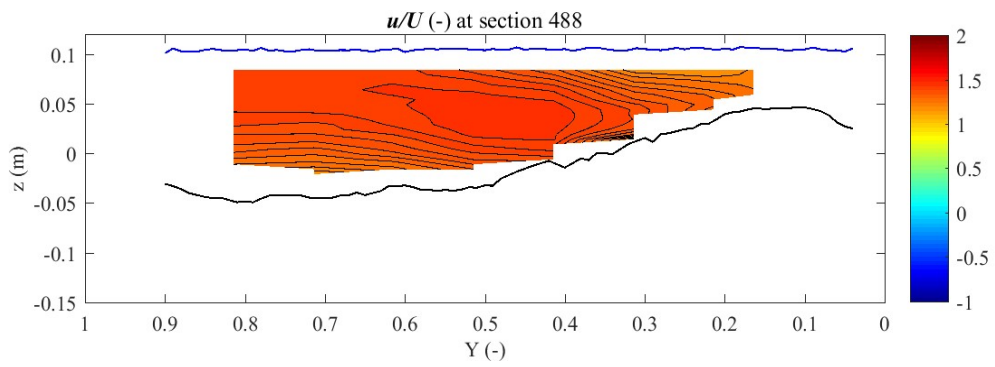


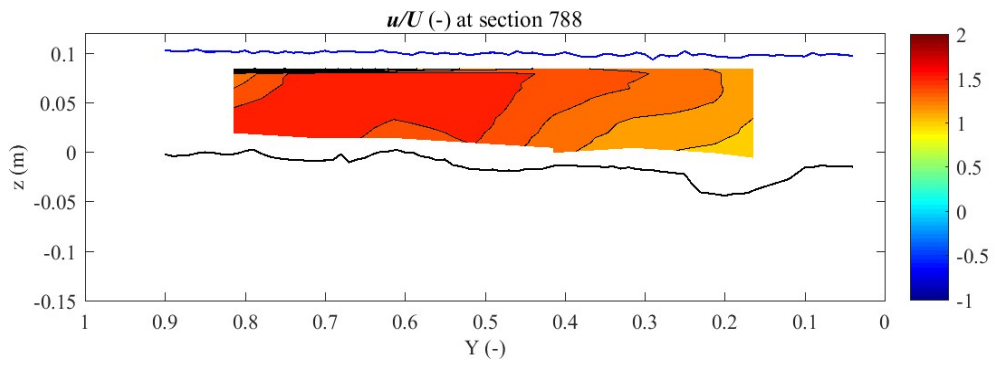
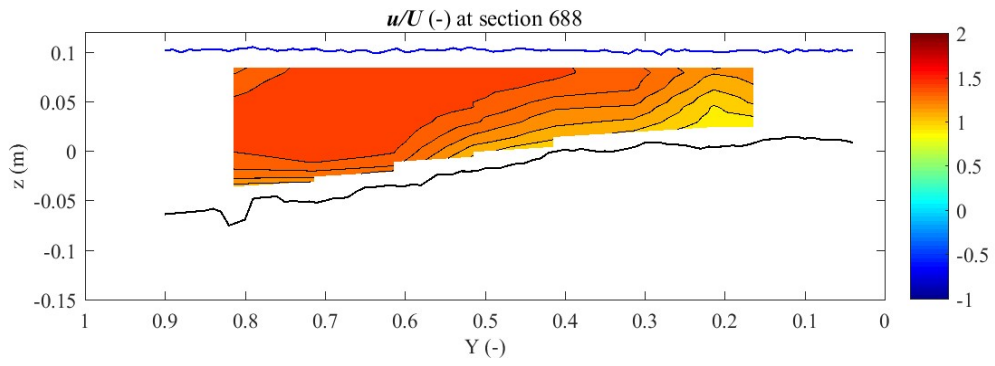




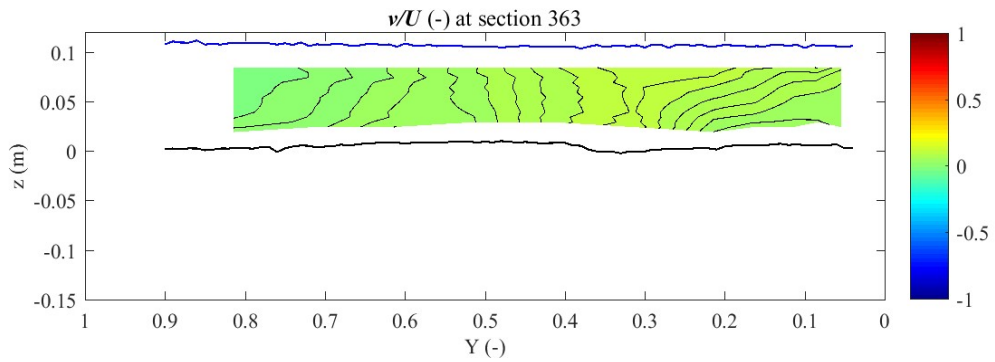
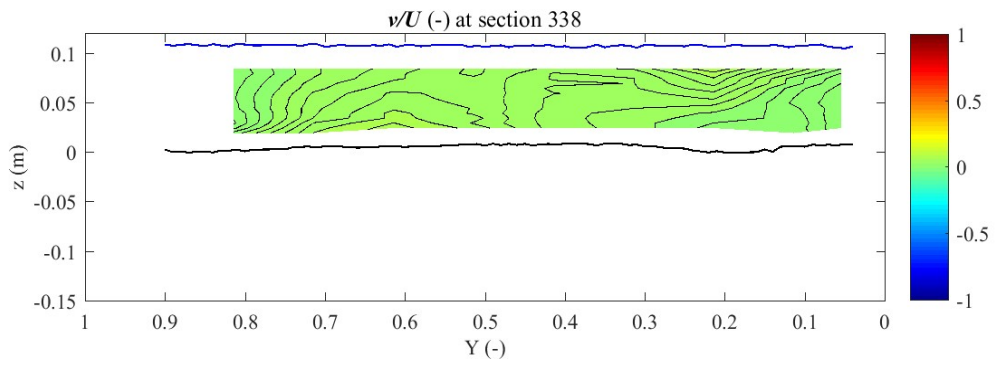
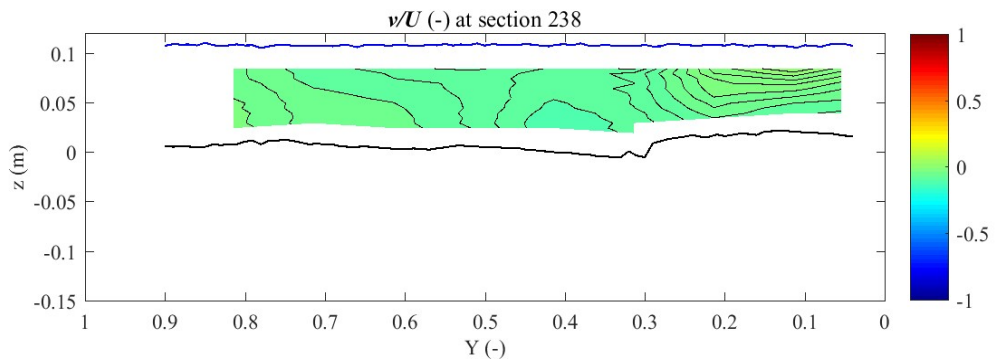


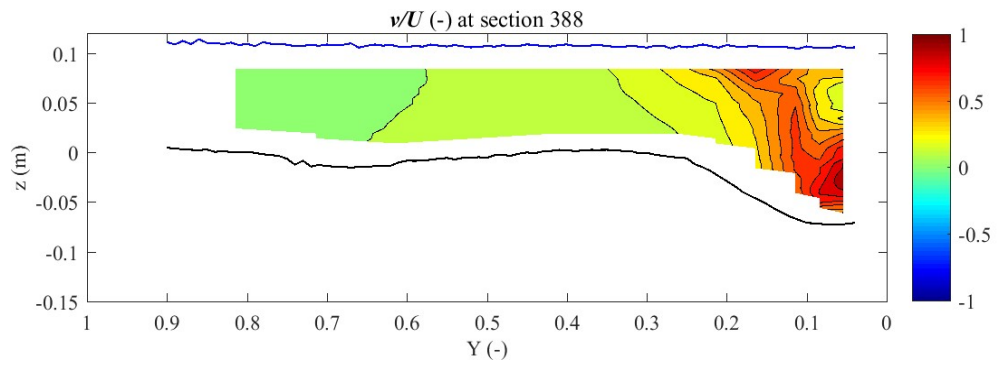
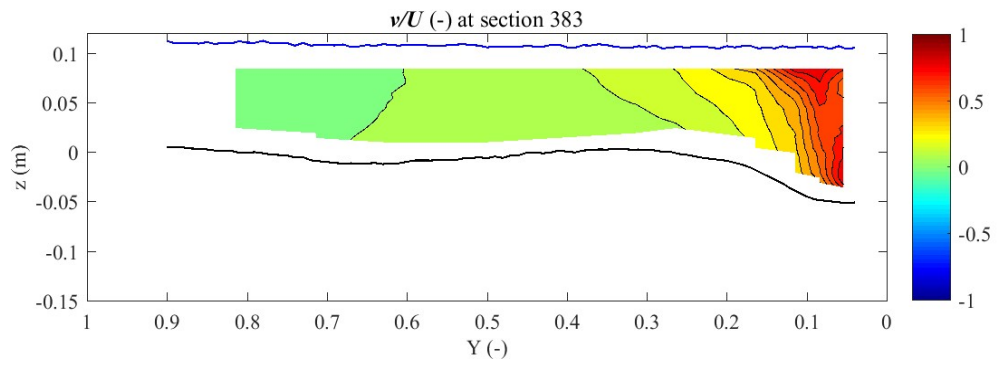
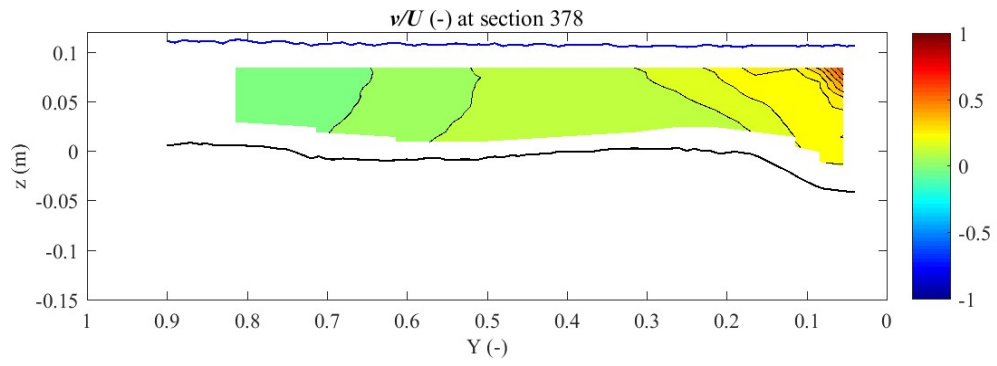


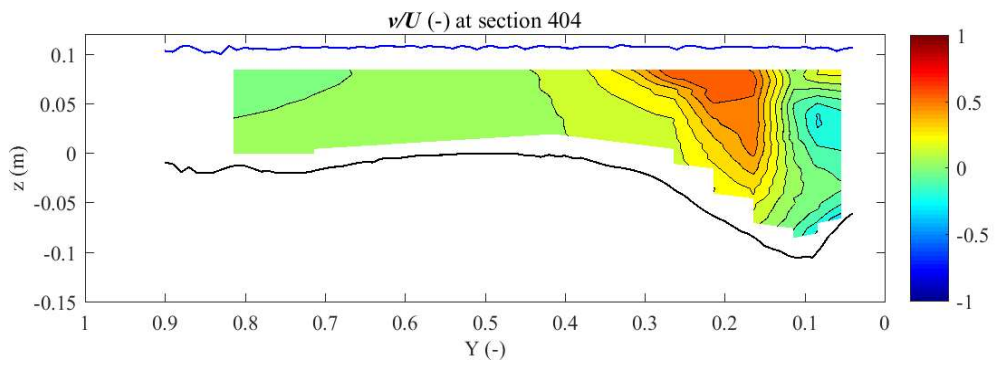
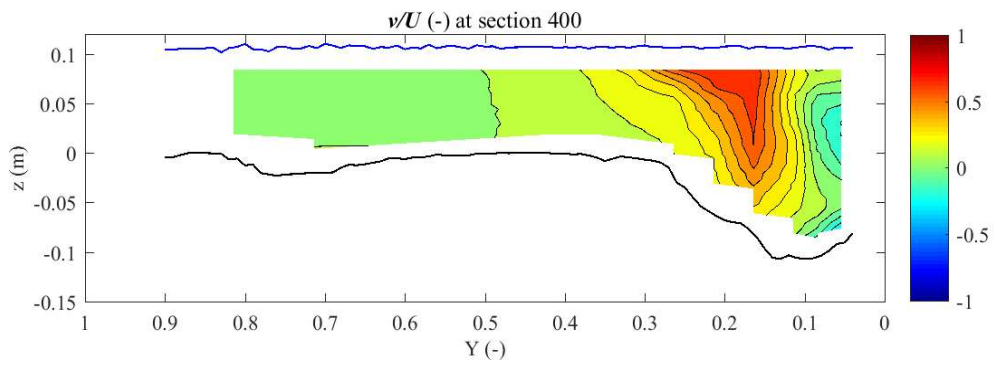
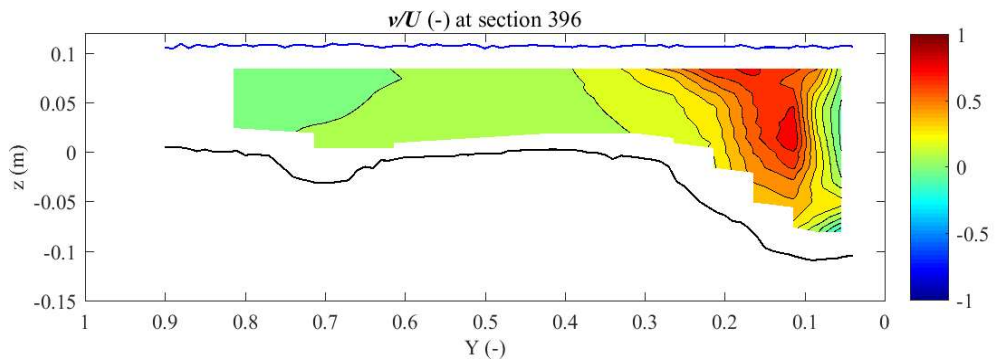
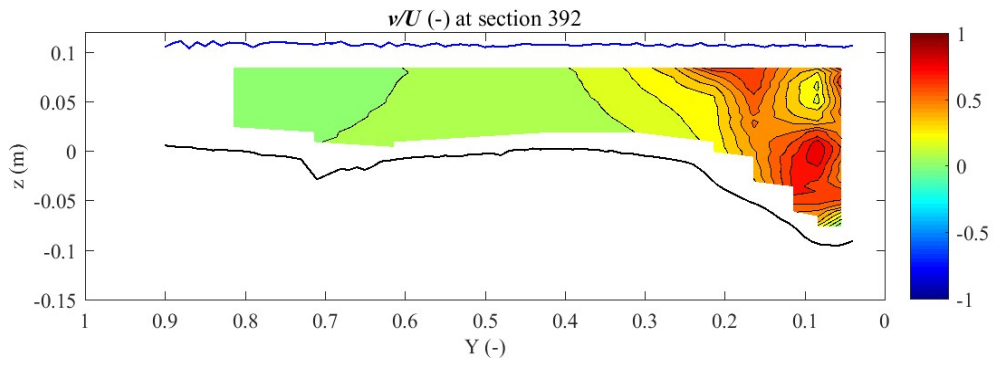


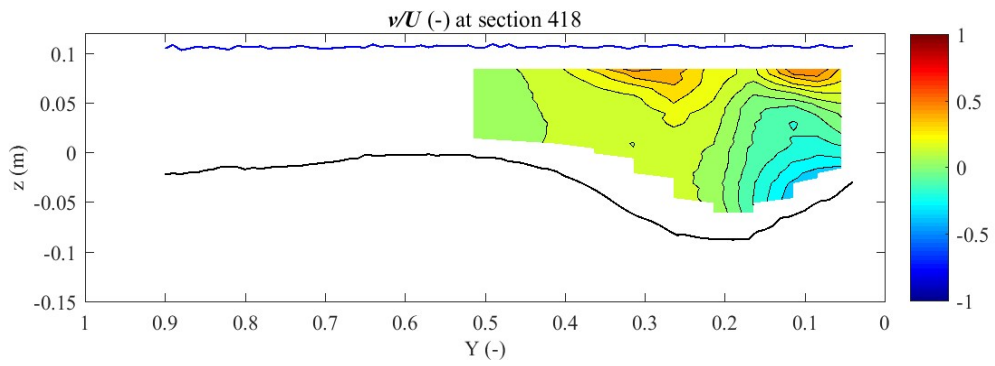
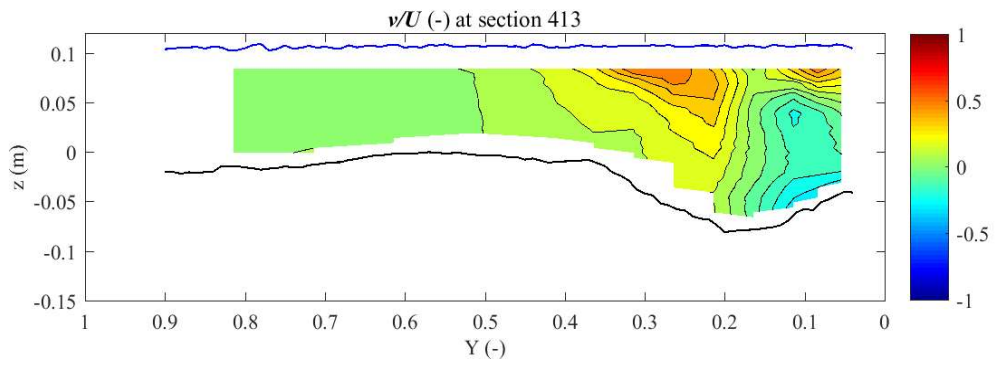
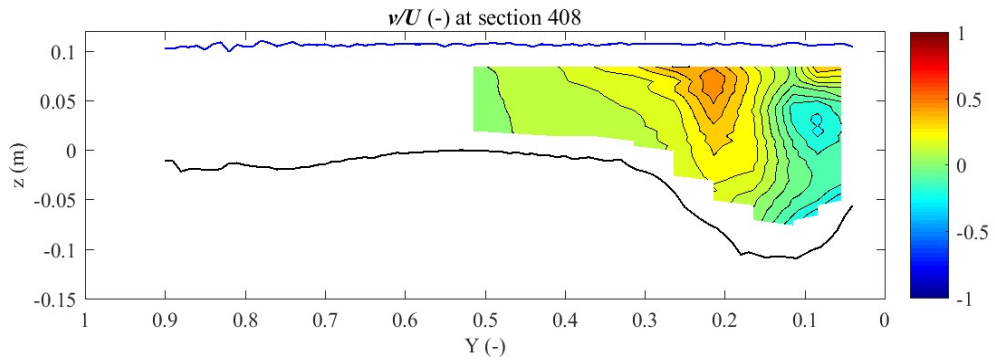


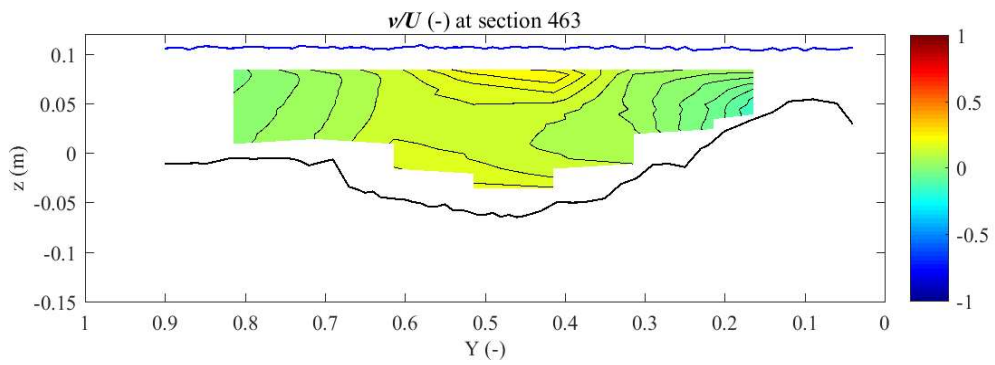
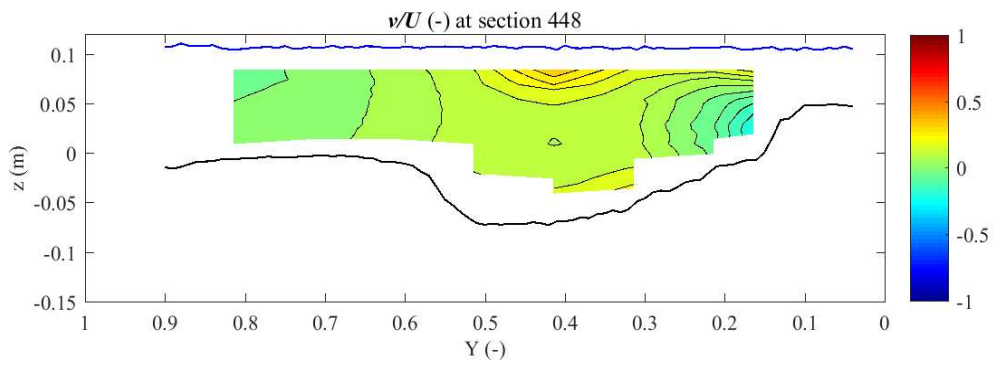
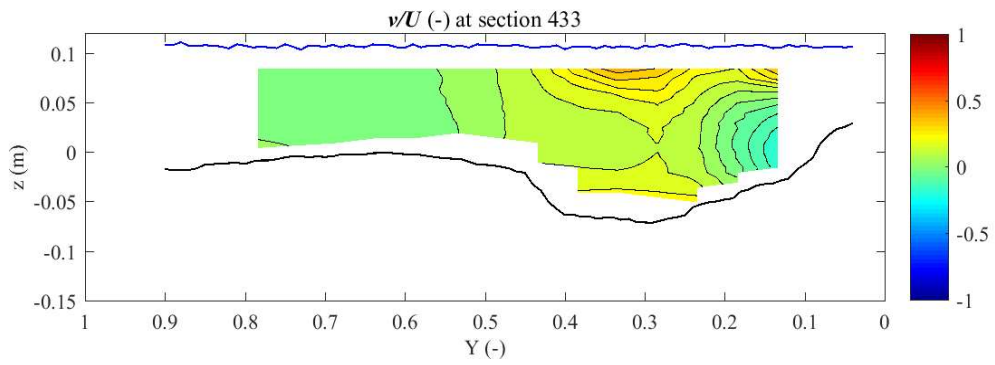
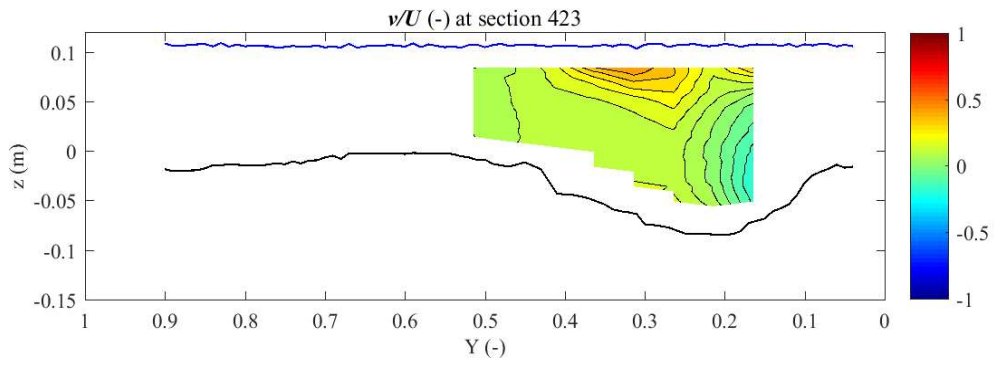
Appendix B – v/U isolines

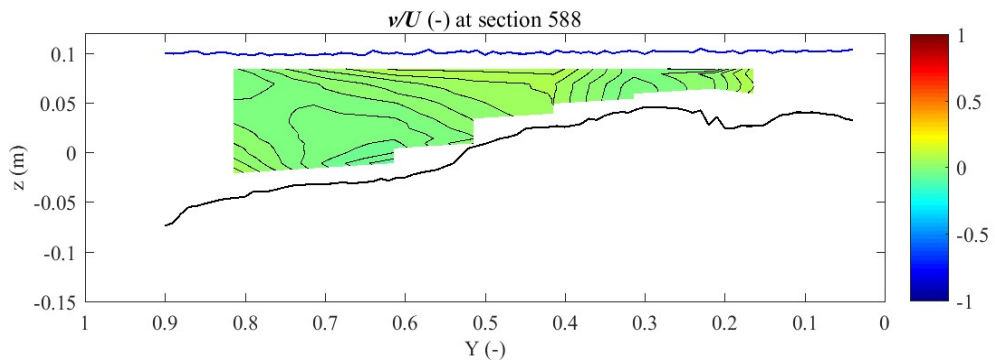
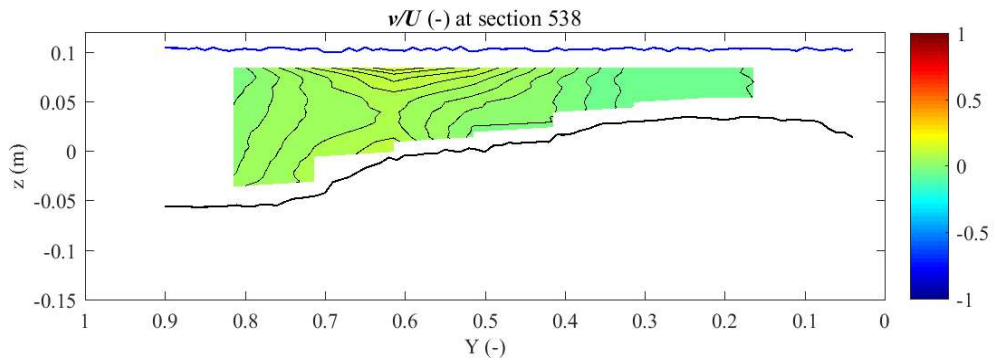
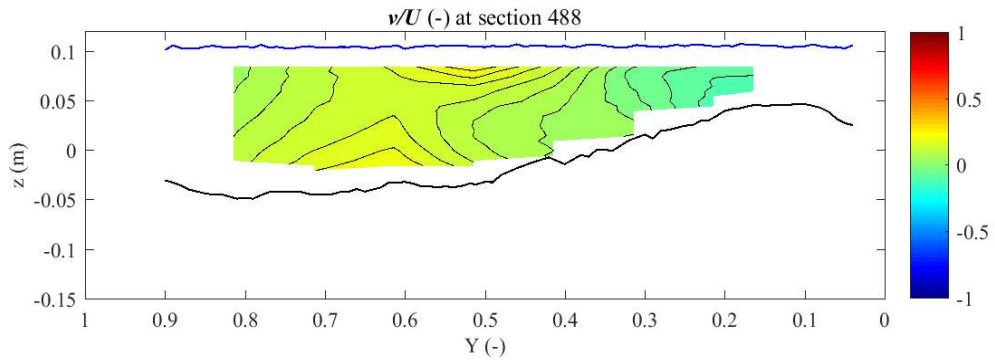


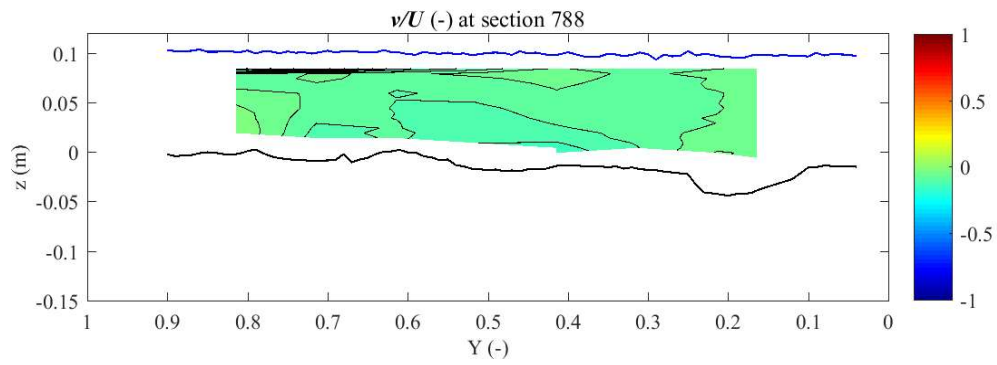
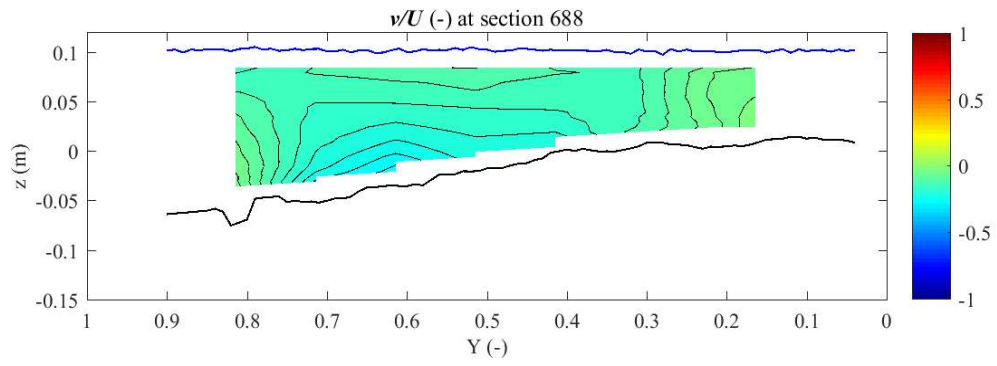




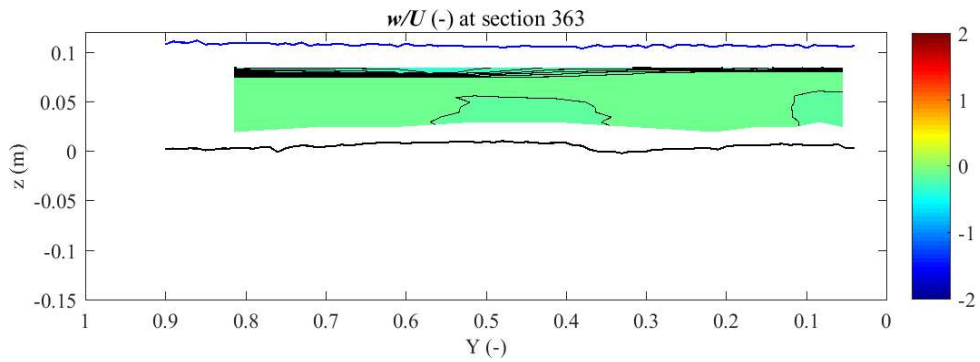
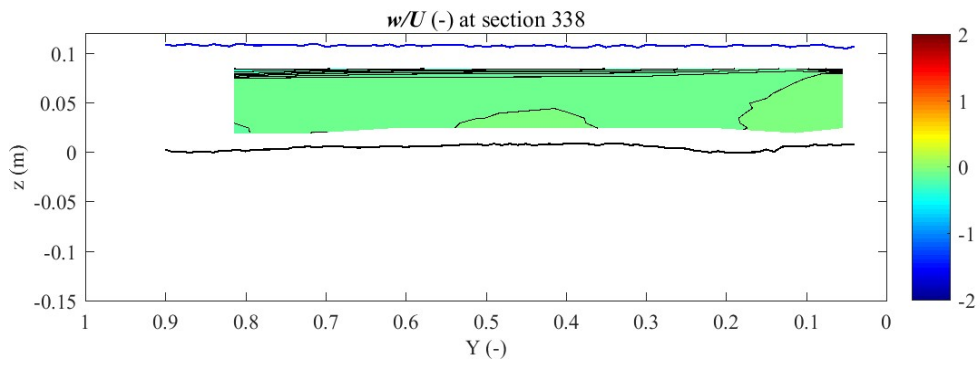
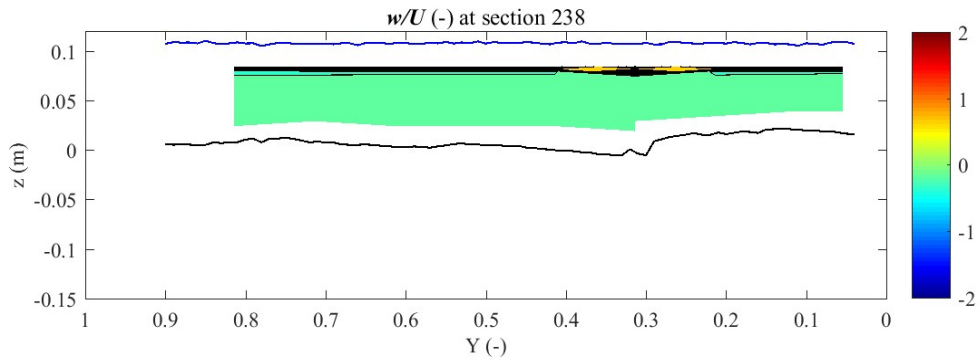


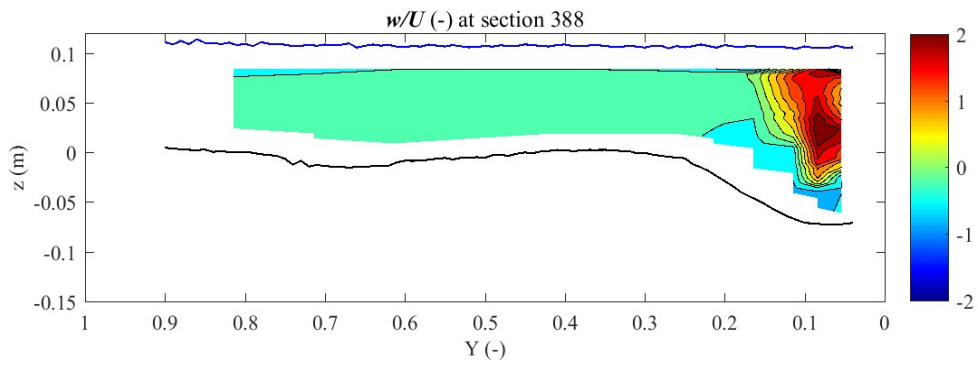
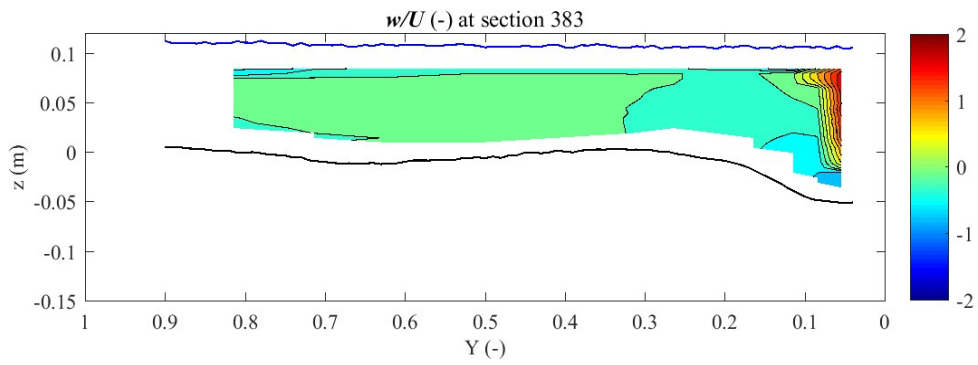
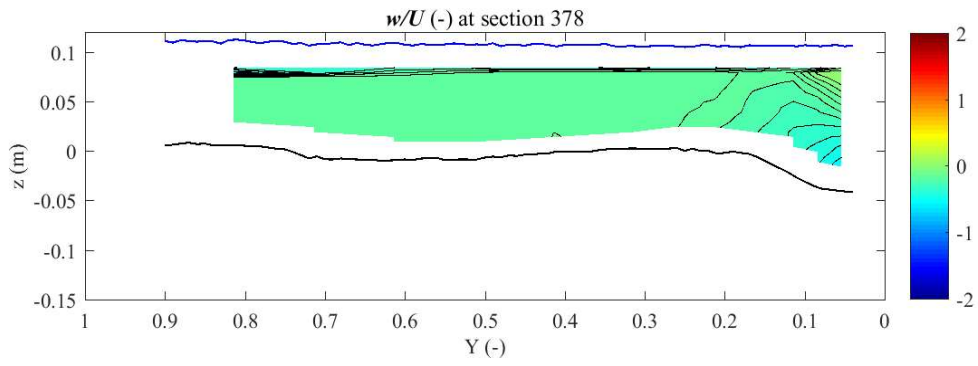


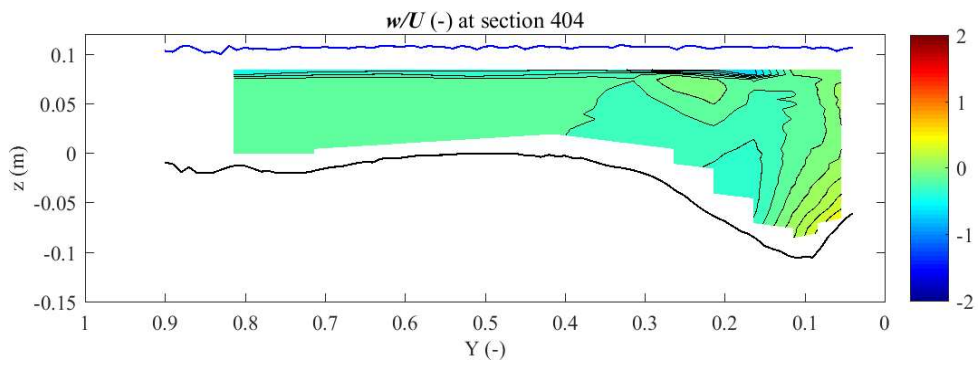
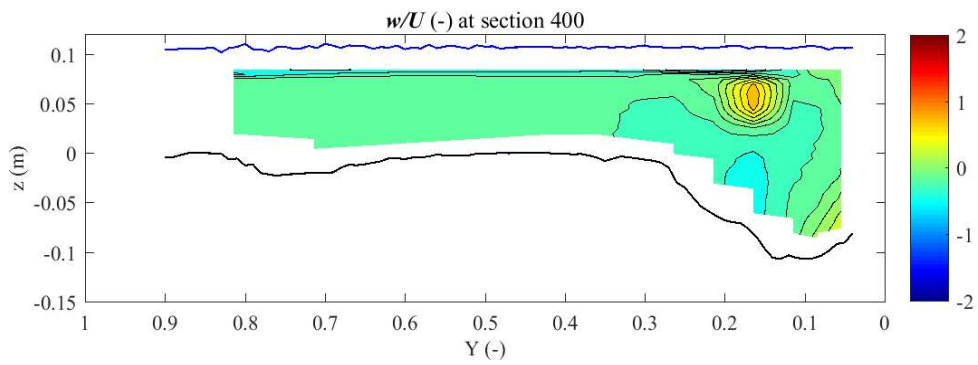
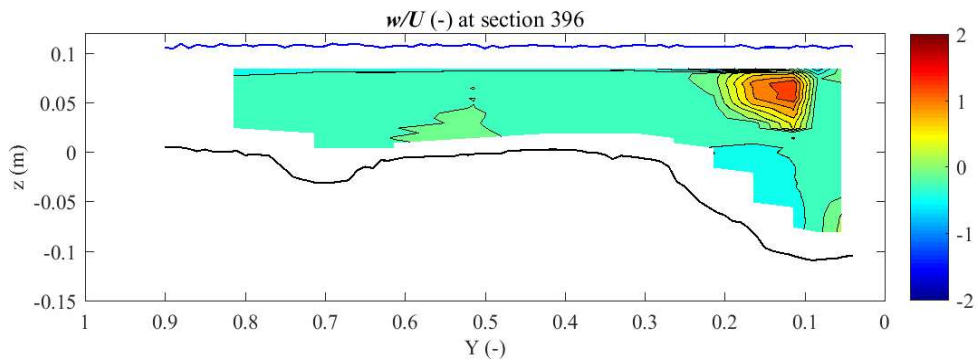
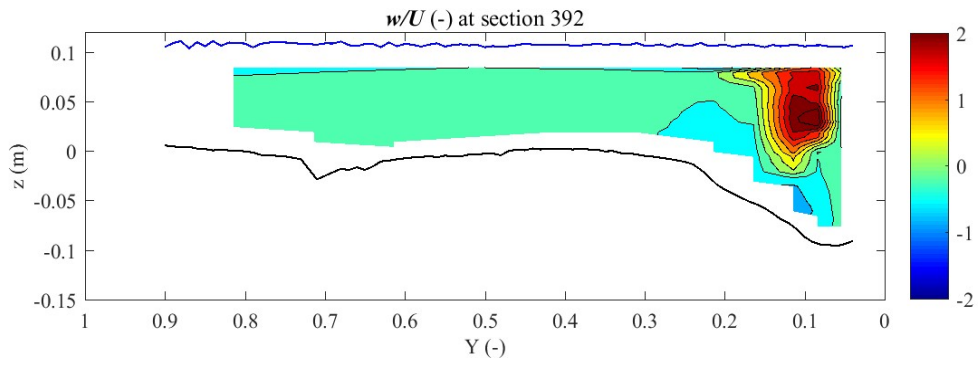


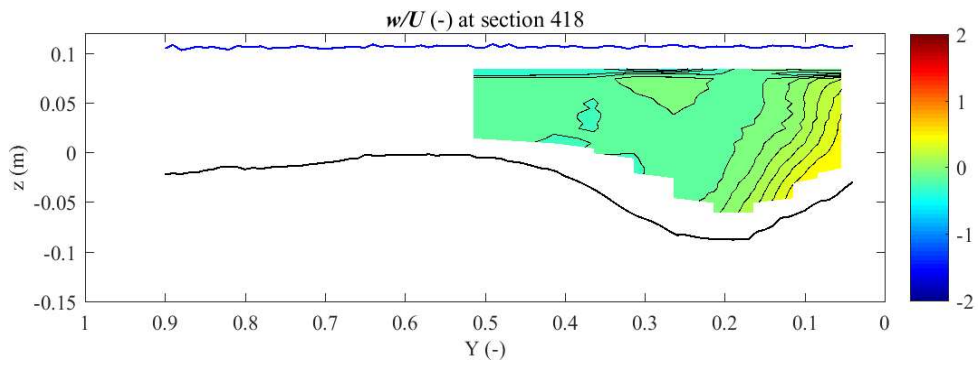
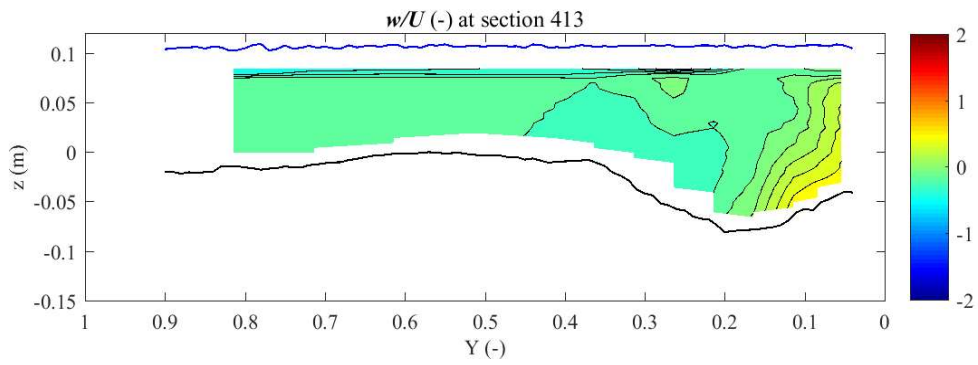
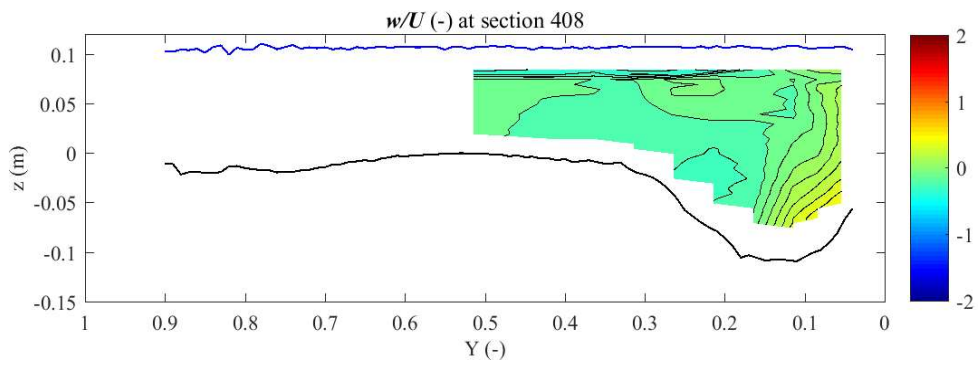


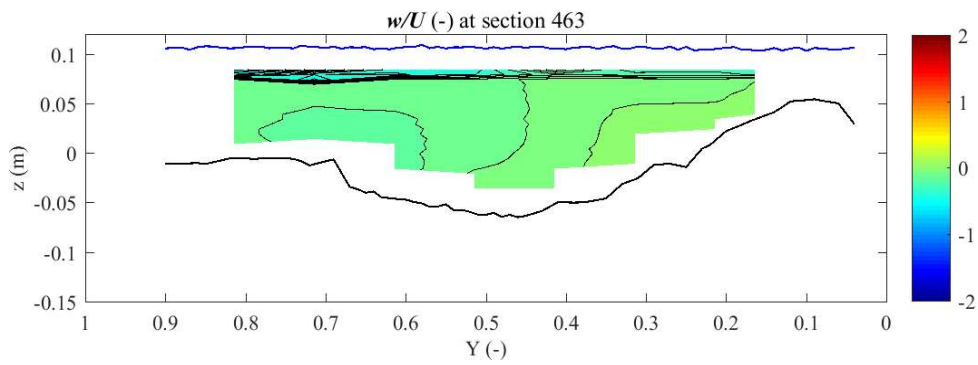
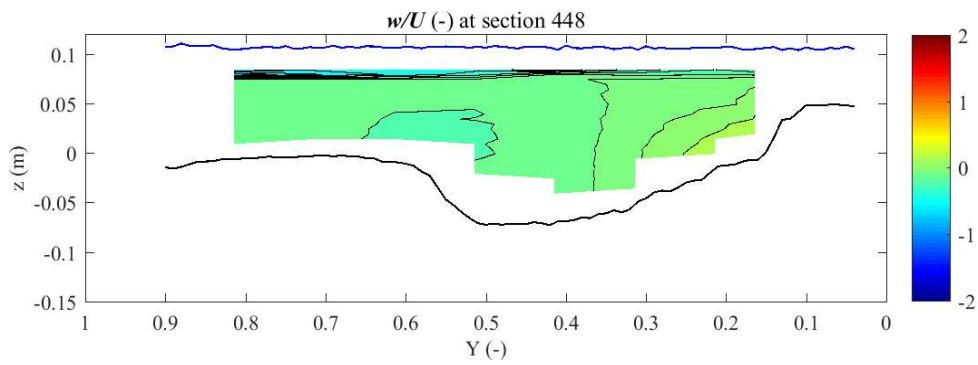
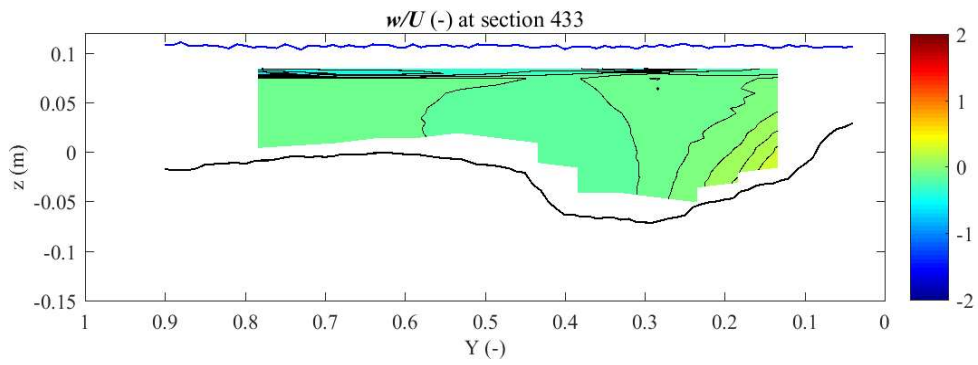
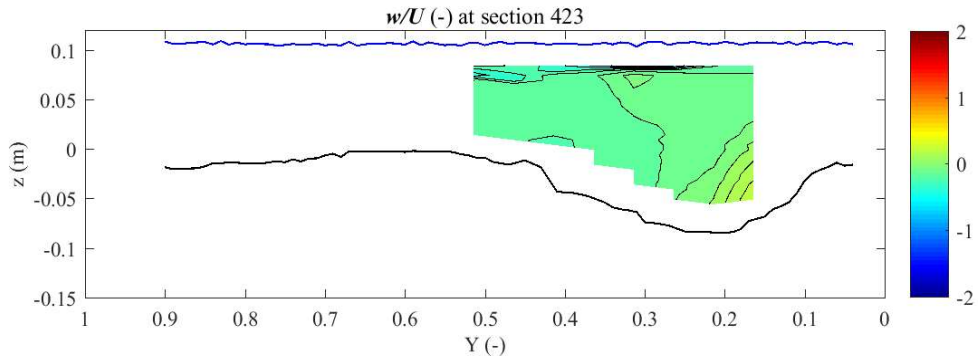
Appendix C – w/U isolines

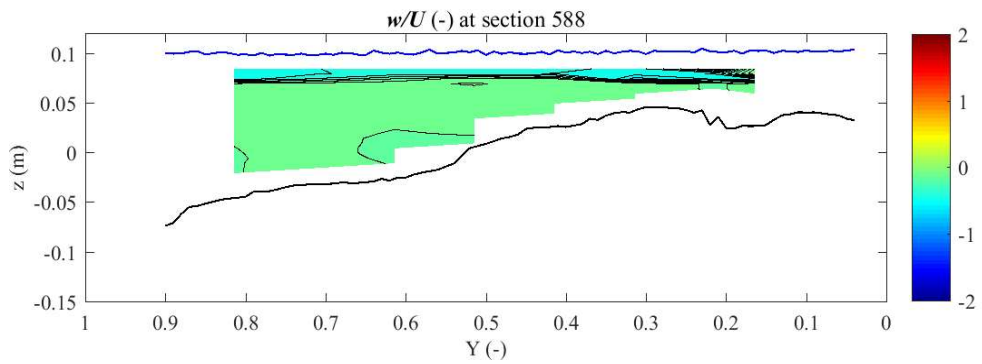
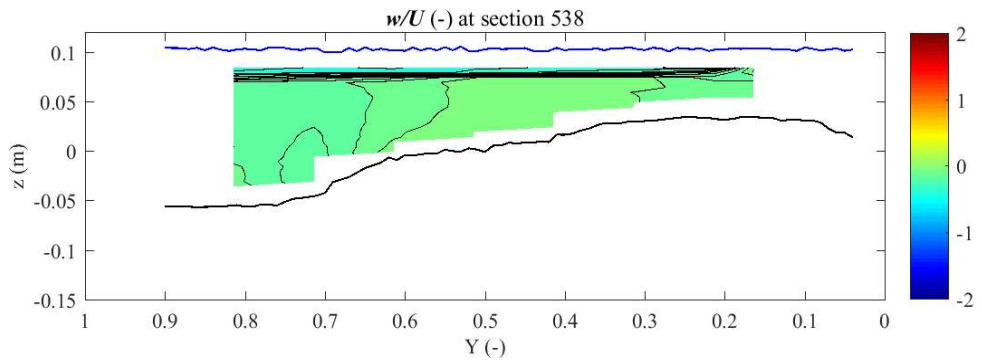
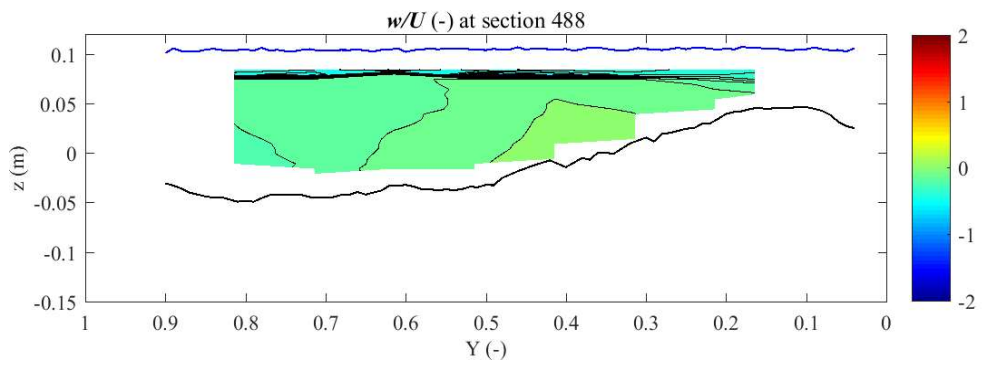


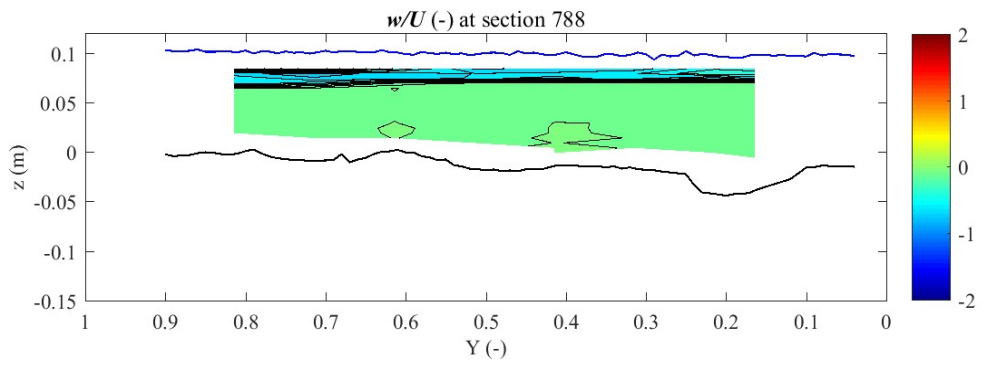
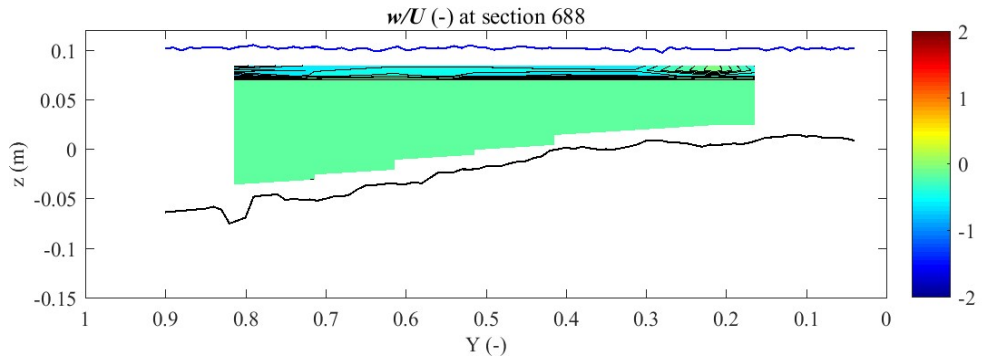




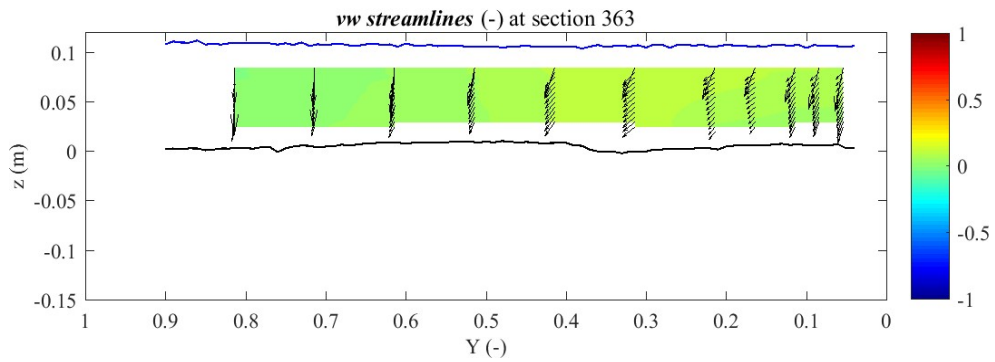
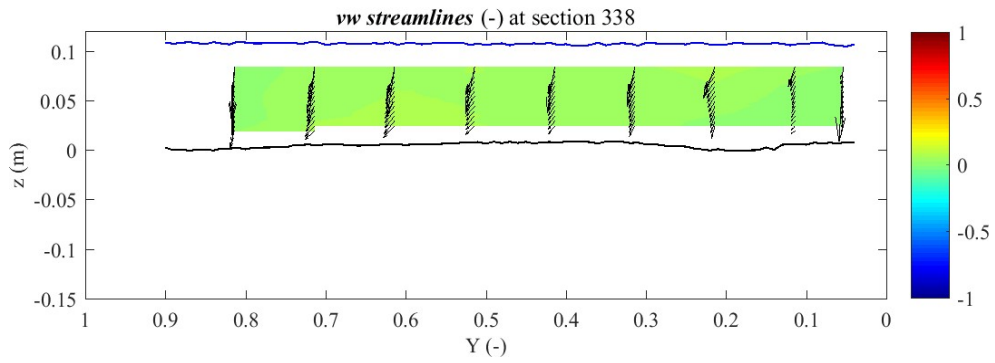
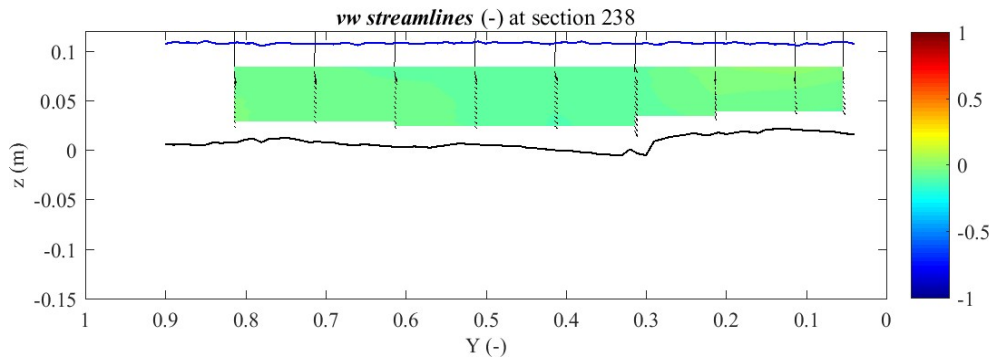


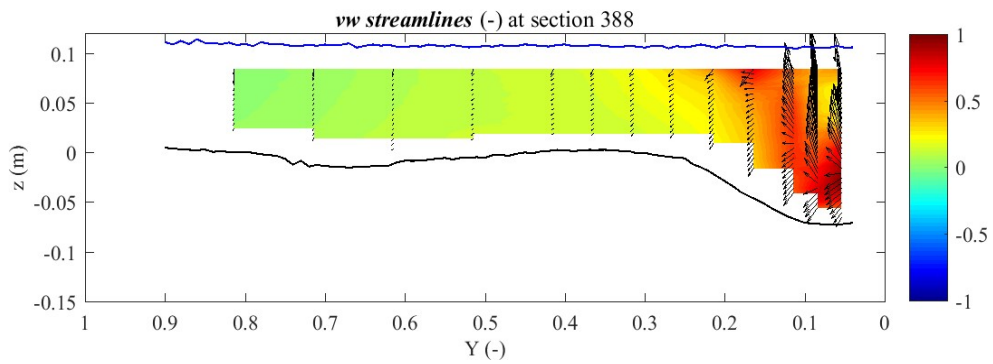
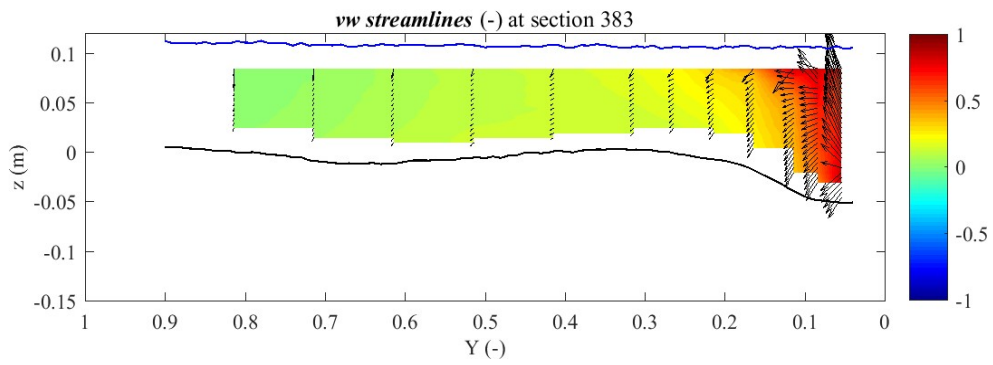
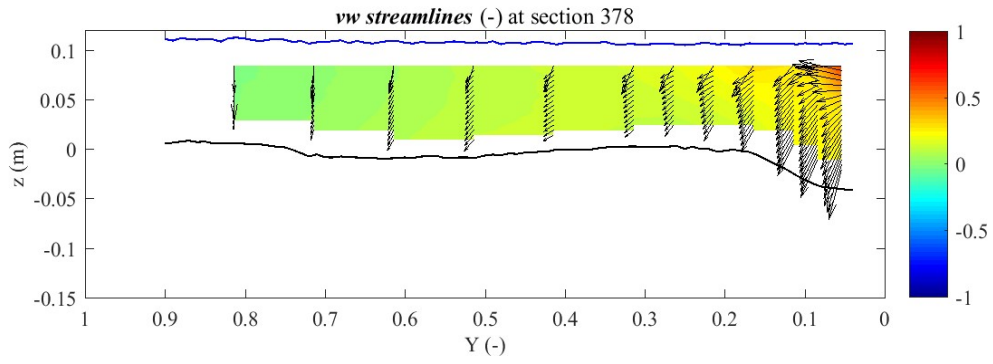


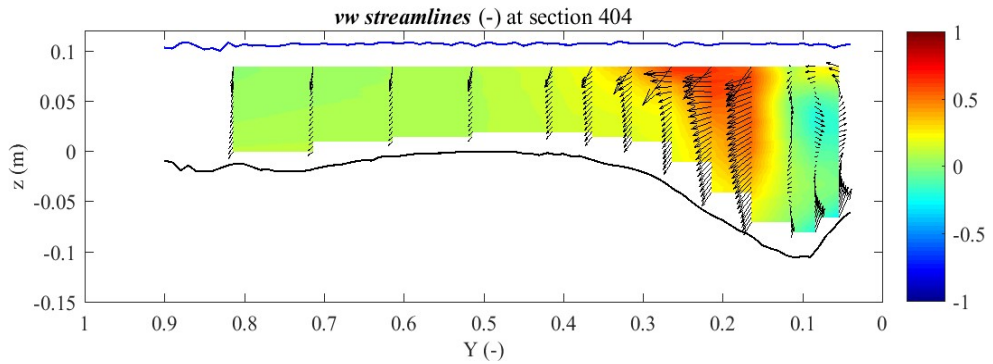
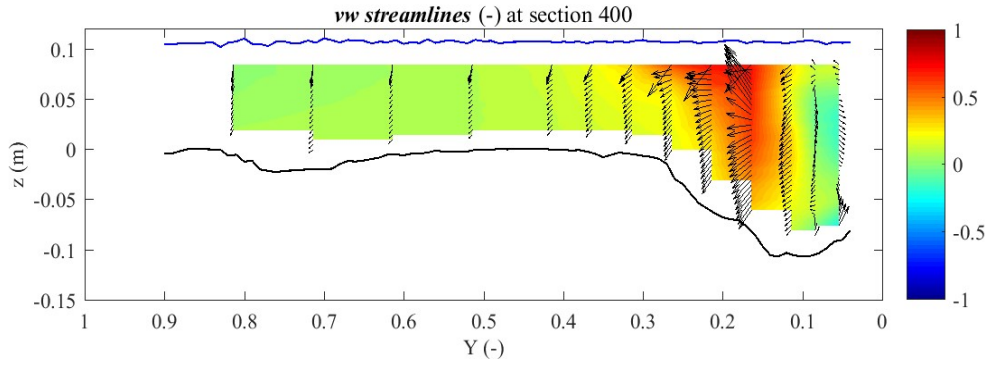
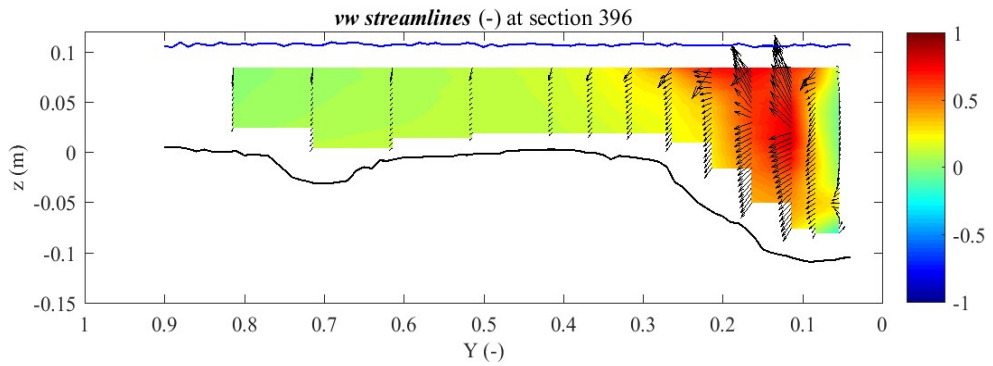
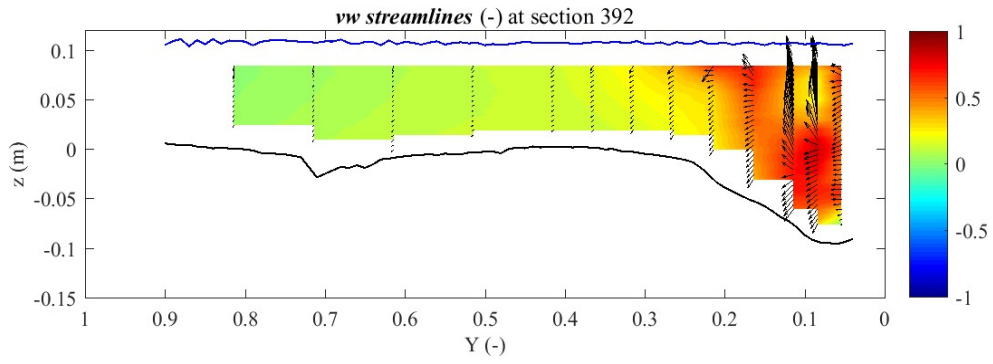


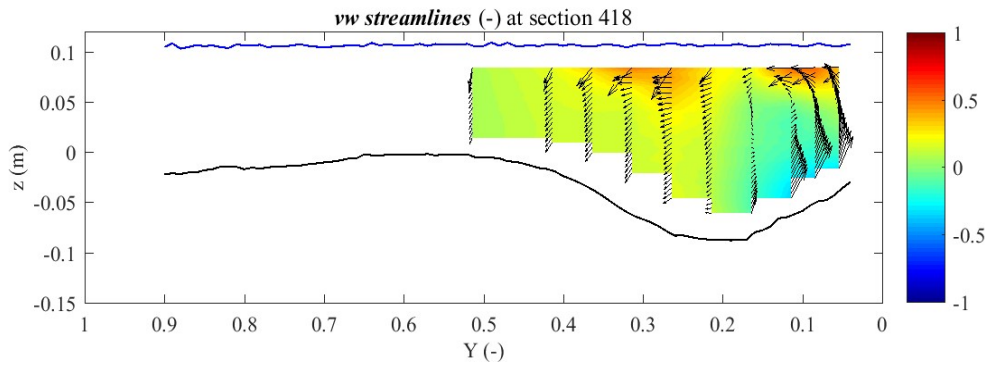
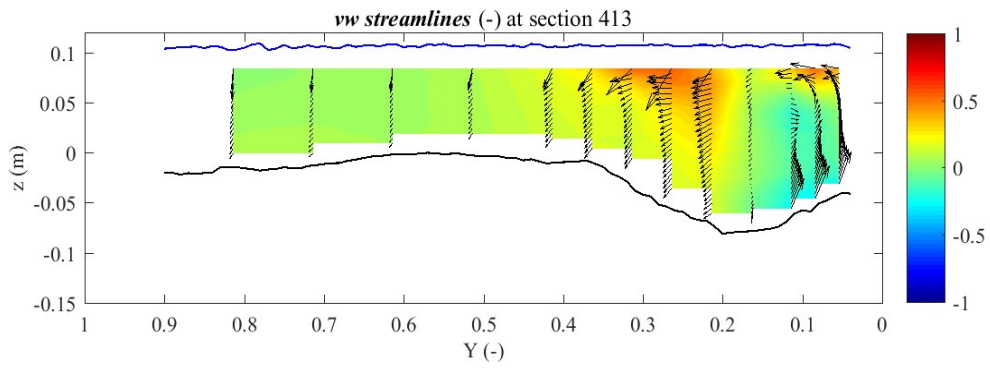
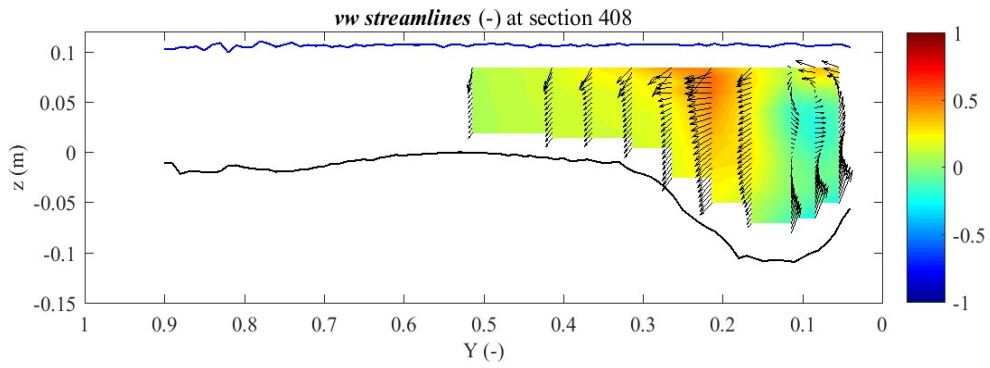


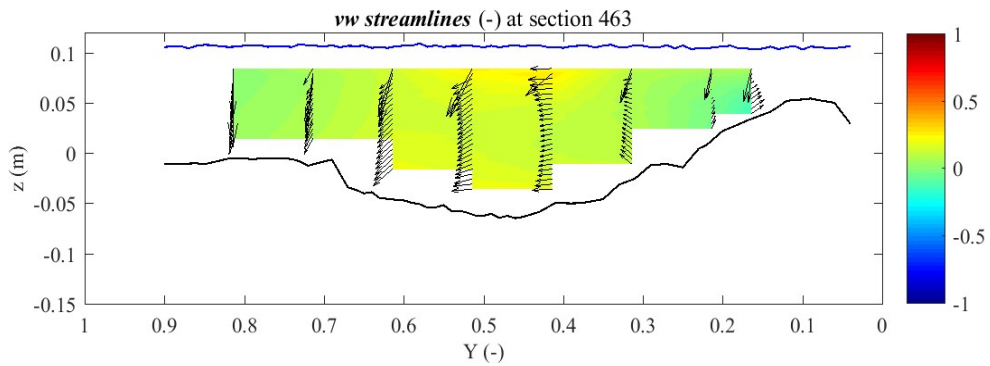
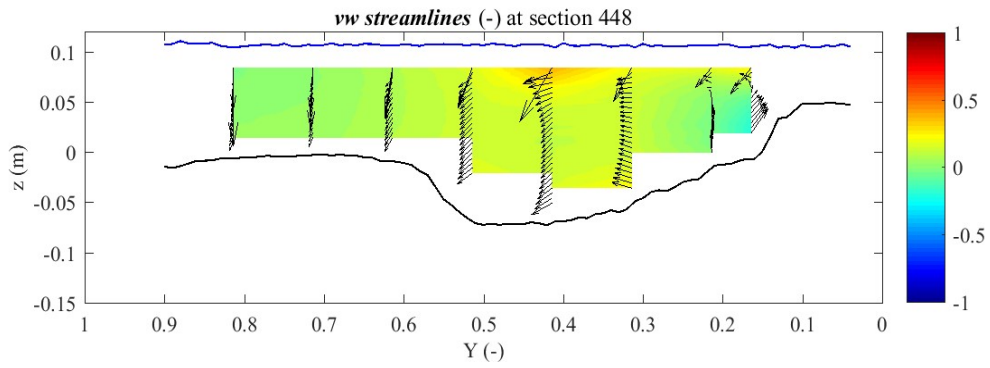
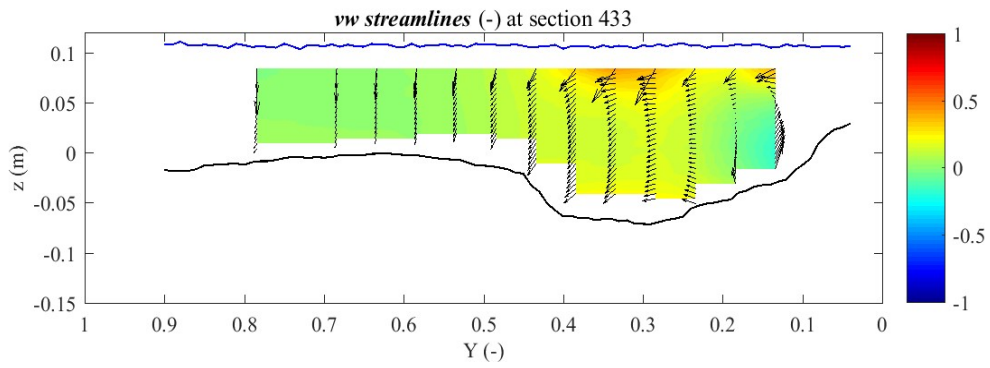
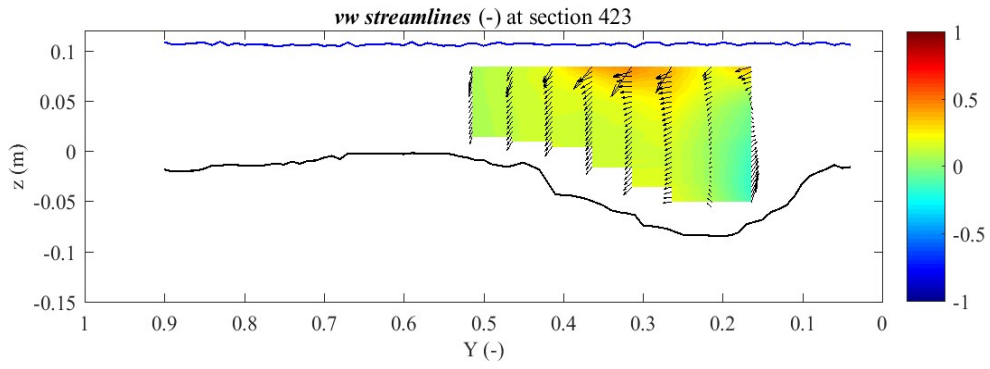
Appendix D – vw pseudo-streamlines

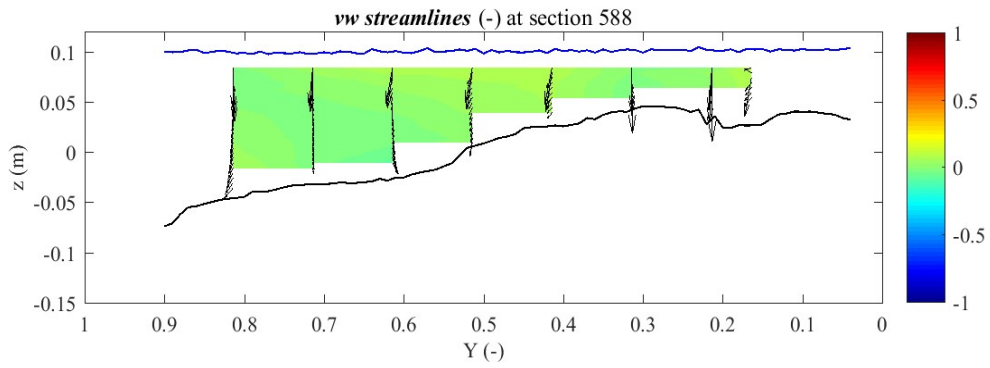
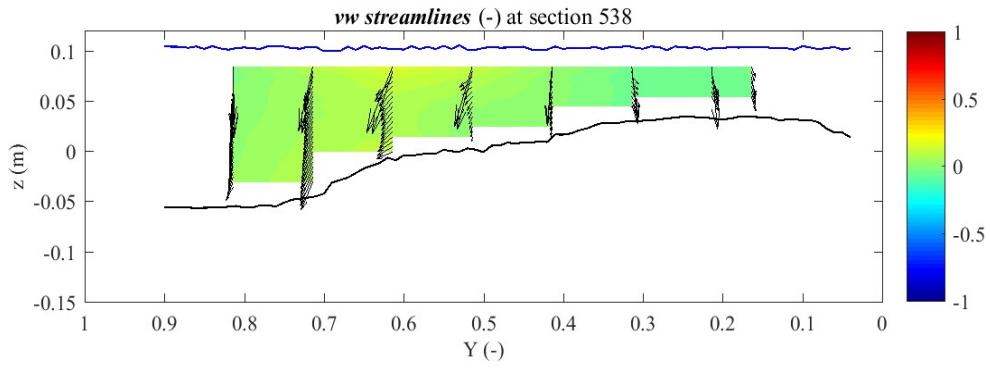
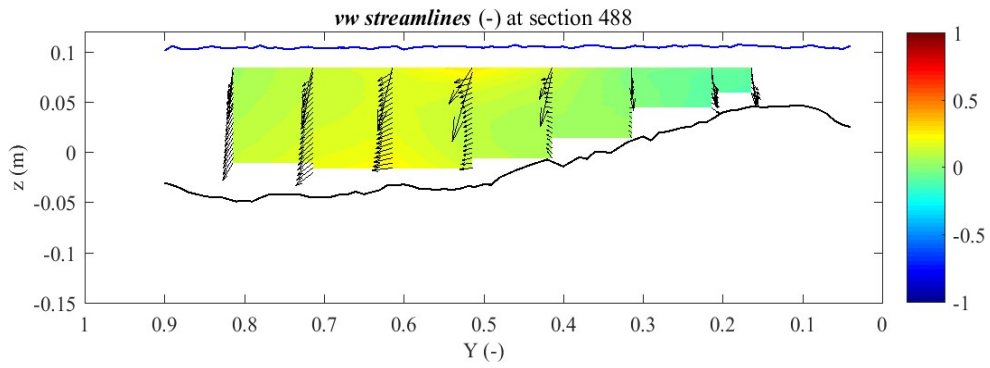


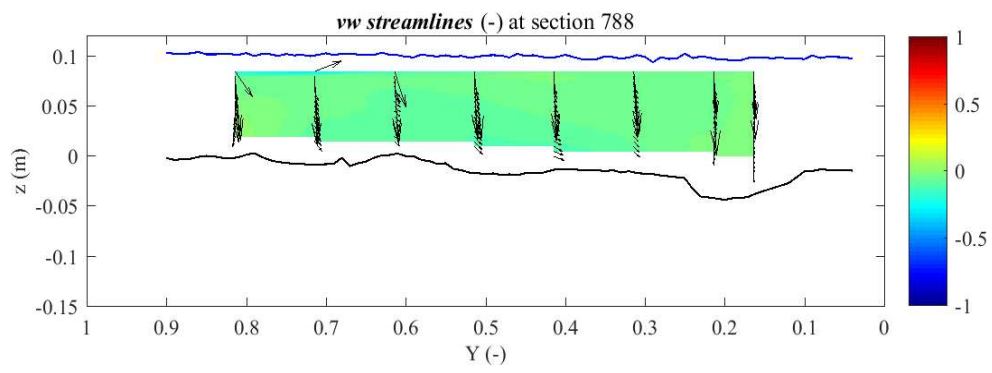
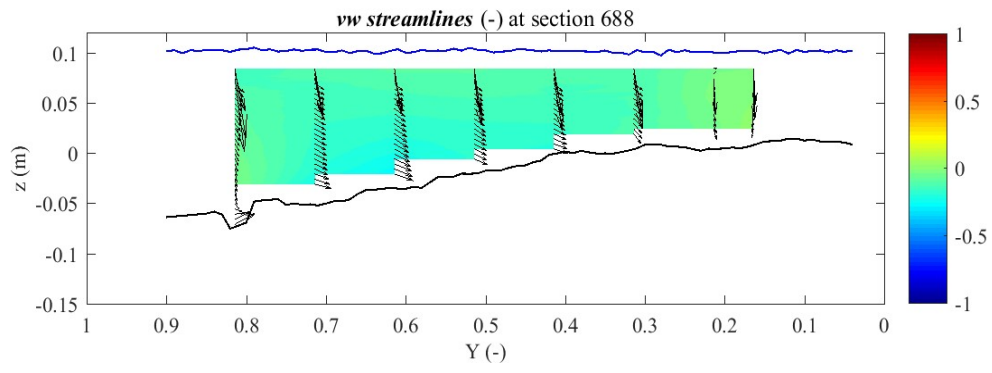




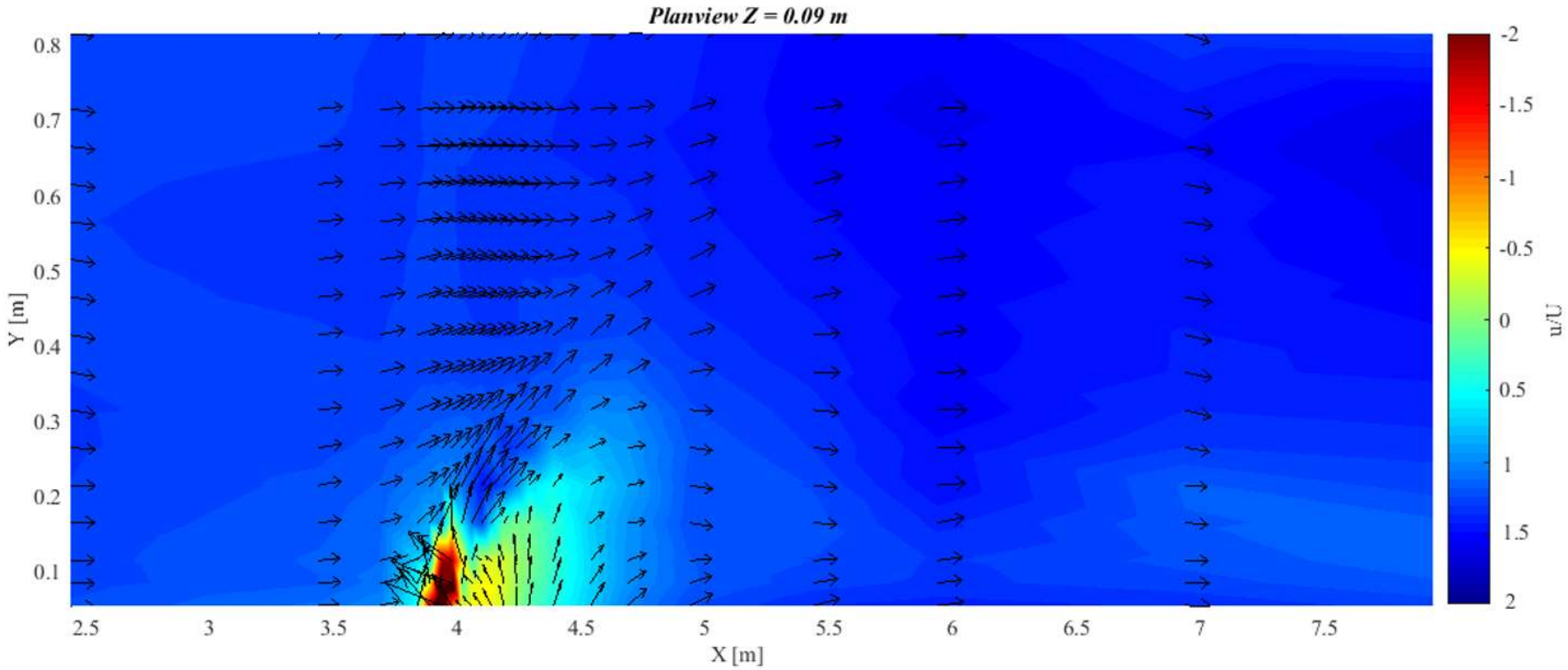


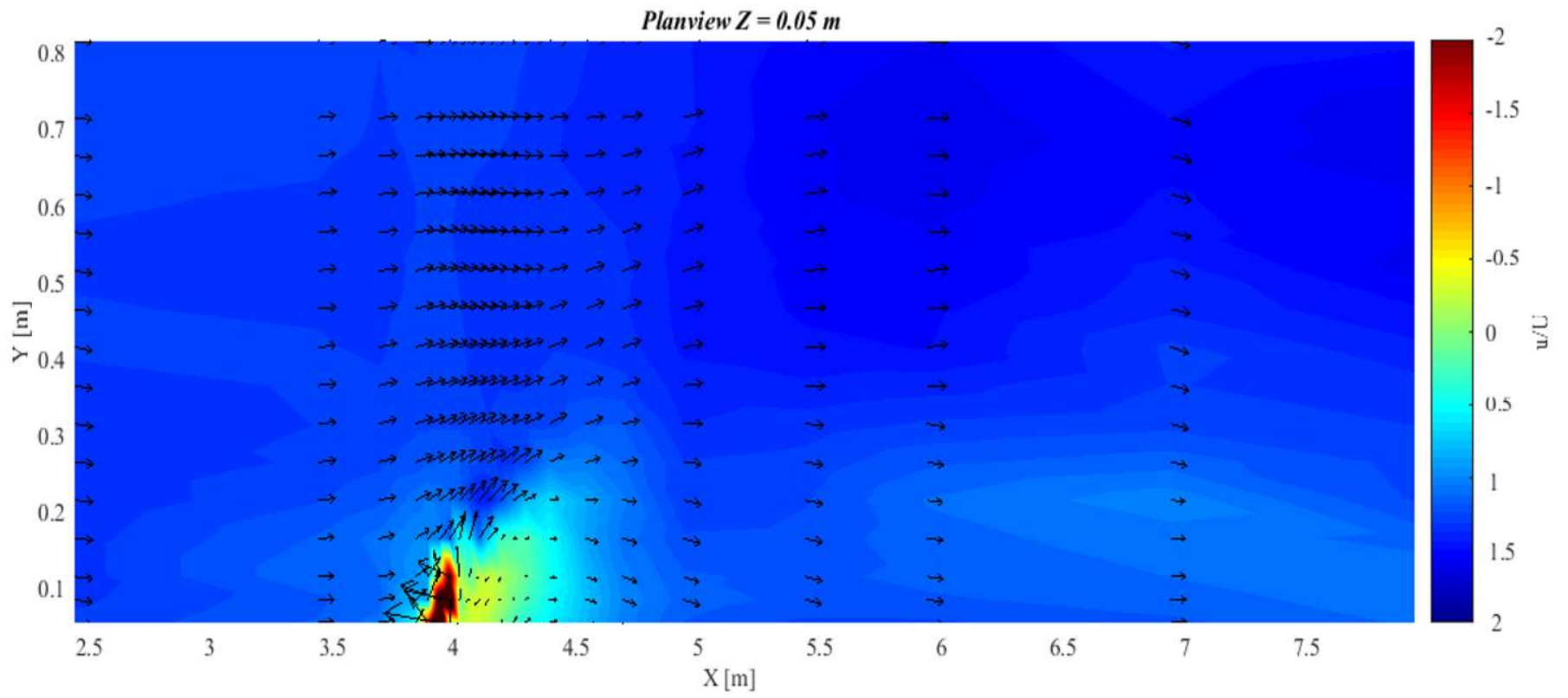




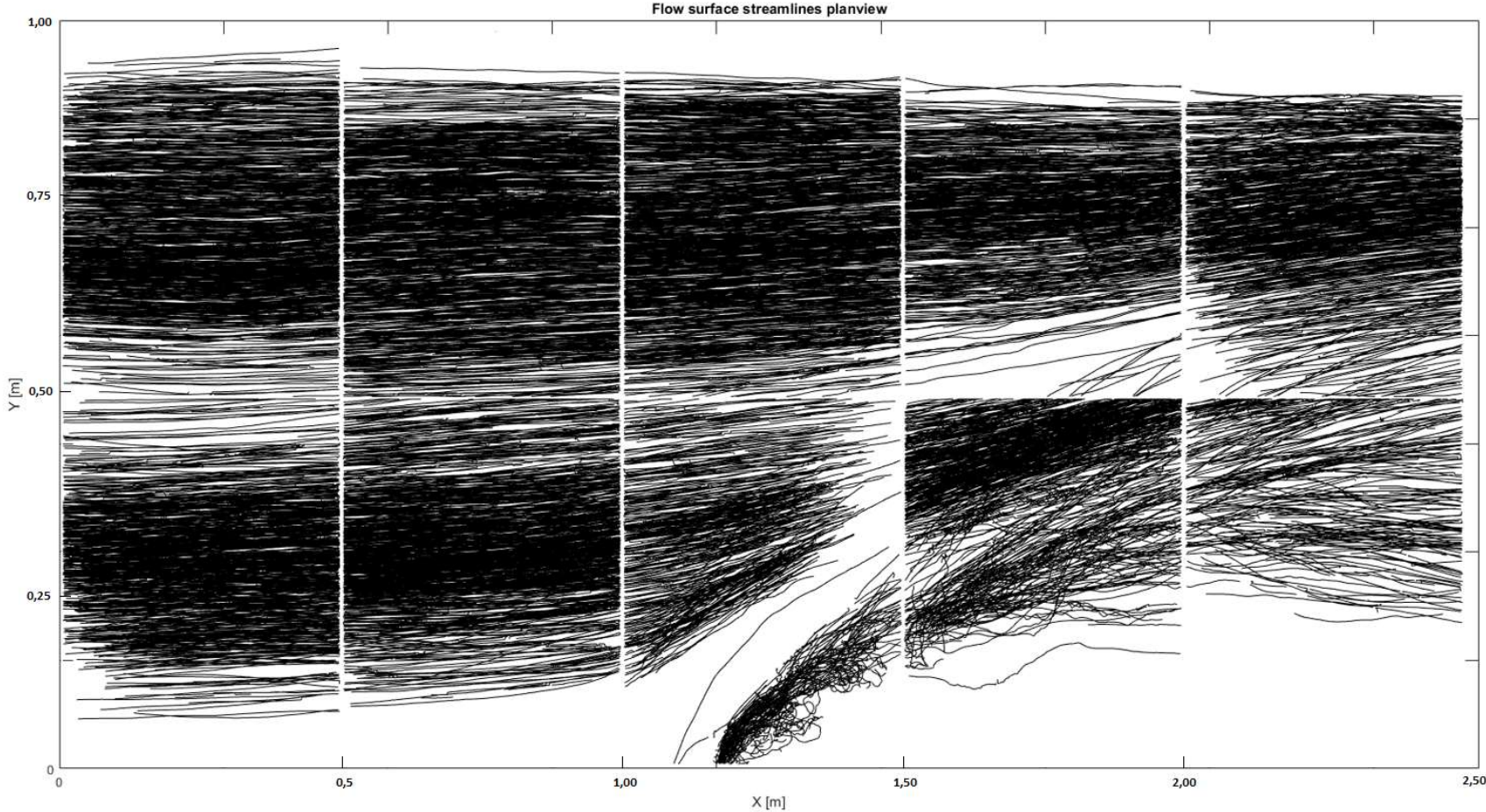


Appendix E – u/U planviews





Appendix F – Flow surface streamlines planview



Appendix G – u/U planviews with bed topography overlay

